MULTI-SENSOR TECHNIQUES FOR THE MEASUREMENT OF POST ERUPTIVE VOLCANIC DEFORMATION AND DEPOSITIONAL FEATURES

By

David B. McAlpin, BBA, MS

A Dissertation Submitted in Partial Fulfillment of the Requirements

for the Degree of

Doctor of Philosophy

in

Geology

University of Alaska Fairbanks

August 2019

APPROVED:

Dr. Franz J. Meyer, Co-Chair
Dr. James Begét, Co-Chair
Dr. Peter W. Webley, Committee Member
Dr. Jonathan Dehn, Committee Member
Dr. Paul McCarthy, Chair
Department of Geosciences
Dr. Leah Berman, Interim Dean
College of Natural Science and Mathematics
Dr. Michael Castellini
Interim Dean of the Graduate School

Abstract

Remote sensing of volcanic activity is an increasingly important tool for scientific investigation, hazard mitigation, and geophysical analysis. These studies were conducted to determine how combining remote sensing data in a multi-sensor analysis can improve our understanding of volcanic activity, depositional behavior, and the evolutionary history of past eruptive episodes. In a series of three studies, (1) optical photogrammetry and synthetic aperture radar are combined to determine volumes of lahars and lava dome growth at Redoubt Volcano, Alaska; (2) applied data from multiple synthetic aperture radar platforms are combined to model long-term deposition of pyroclastic flow deposits, including past deposits underlying current, observable pyroclastic flow deposits at Augustine Volcano, Alaska; and finally (3) combined, low-spatial-resolution thermal data from Advanced Very High Resolution Radiometer sensors are combined with high resolution digital elevation models derived from the microwave TanDEM-X mission, to increase the accuracy of eruption profiles and effusion rates at Tolbachik Volcano on the Kamchatka Peninsula, Russian Far East. As a result of this study, the very diverse capabilities of multiple remote sensing instruments were combined to improve the understanding of volcanic processes at three separate locations with recent eruptive activity, and to develop new methods of measurement and estimation by merging the capabilities of optical, thermal, and microwave observations. With the multi-sensor frameworks developed in this study now in place, future efforts should focus on increasing the diversity of sensor types in joint analyses, with the objective of obtaining better solutions to geophysical questions.

Table of Contents

List of Figures

List of Tables

Acknowledgments

The text of Chapters 1–3 frequently used the pronouns "we," and "our," in recognition of the contributions made by other researchers, whose collaboration was essential to completion of these projects. Substantial assistance was provided by Dr. Franz Meyer, at the University of Alaska Fairbanks Geophysical Institute and the Alaska Satellite Facility, who provided significant technical assistance and advice in the conduct of the research, and preparation of all manuscripts, as well as supervision, editing, and technical guidance. Dr. Wenyu Gong of the State Key Laboratory of Earthquake Dynamics, Beijing, provided InSAR processing for ERS-1 and 2, RADARSAT-1, and PALSAR data stacks in Chapter 2, and Dr. James E. Begét from the University of Alaska and Alaska Volcano Observatory contributed interpretation and participated in all results. Dr. Julia Kubanek, of the European Space Research and Technology Centre in Noordwijk, Netherlands, provided processed TanDEM-X datasets of Tolbachik Volcano, as well as access to key DEMs that were essential to completing the work in Chapter 3. Dr. Peter Webley, of the University of Alaska Fairbanks Geophysical Institute and VADAPT, Inc., provided technical support and editing for Chapter 2, as well as access to AVHRR datasets archived by VADAPT, Inc. and analyzed in Chapter 3. Dr. Webley and Dr. Jonathan Dehn, also of VADAPT, Inc., and Southern Methodist University in Dallas, were essential participants in providing technical expertise and comments that greatly improved the manuscript for Chapter 3. The assistance and support of all is gratefully acknowledged.

Introduction

Remote sensing of the environment has grown from an experimental technology on the edge of scientific investigation, to a mainstream tool used in most earth observation disciplines. Orbital platforms have progressed so rapidly, that technologies once described as advanced have become common place in less than a generation. Earth observation satellites have grown from Landsat 5, with 7-bands of multispectral imaging, to the hyperspectral Hyperion instrument, with 220 spectral bands (USGS, 2010), and the Atmospheric Infrared Sounder (AIRS) instrument, with 2378 infrared detectors (Olsen, 2017). The commercial WorldView-4 satellite, launched in 2016, has a ground resolution of 0.30 m to 1.24 m with revisit periods of less than one day (DigitalGlobe, 2019). At the beginning of that same generational span, synthetic aperture radar (SAR) was barely beginning its mainstream emergence. The first European SAR satellite (ERS-1), became operational in 1991, followed by ERS-2 and the Canadian Radarsat-2 in 1995 (Morena et al., 2004; ESA, 2011). At this writing in spring 2019, there are six dedicated, civilian SAR satellites operated by five countries and the European Union, with ground resolutions as low as one meter.

Visible, thermal, and imaging technologies now find themselves being combined together to increase Earth observation capabilities to study critical topics of interest, including but not limited to Earth's natural hazards, climate change, environmental damage, weather dangers, urban studies, and rising seas. With the present Earth observation capabilities providing a comprehensive suite of instruments and sensors that will continue to grow, this dissertation study investigates how those capabilities can be used to maximize our understanding of volcanic processes, and improve our methods to measure and observe these processes, if remote sensing data from visible, thermal, and microwave wavelength sensors are combined to increase our knowledge of the volcanic systems beyond the capabilities of individual satellites or sensors. In addition to increasing the quality and quantity of information that can be extracted pre-, syn-, and post- volcanic event, a developed multi-sensor data analysis approach would also improve the accuracy of measured event/eruption parameters, and contribute to an improved analysis of the volcanic event/eruption to support local observatories, research scientists, and decision makers.

Chapter 1 is titled "Multi-sensor data fusion for remote sensing of post-eruptive deformation and depositional features at Redoubt Volcano." Redoubt volcano, located in south-central Alaska, erupted on 22 March 2009 with a series of explosive events lasting nearly two weeks. The eruption produced an ash cloud exceeding 18 km above sea level (ASL), and inundated the Drift River Valley with pyroclastic flows and lahars, and, importantly, threatened the Drift River Oil Terminal, a petroleum storage facility east of the volcano. Following the explosions and lahars, the eruption continued through a dome-building and effusive stage that lasted approximately three months, until 1 July 2009.

This chapter focused on spaceborne data from two separate instruments aboard the Advanced Land Observing Satellite (ALOS), launched by the Japan Aerospace Exploration Agency (JAXA) in 2006 (Rosenqvist et al., 2007). Photogrammetric optical images were acquired from the Panchromatic Remote Sensing Instrument for Stereo Mapping (PRISM), and microwave imaging data from the Phased Array type L-band Synthetic Aperture Radar (PALSAR) sensors. Together, the combined data were used to quantify deposition and dome growth from the eruption of Redoubt Volcano in 2009. To demonstrate how multi-sensor efforts could obtain measurements and details of the volcano with high precision, a three-test approach was developed to examine deformation caused by lahar deposits, and to estimate the dimension of the lava dome at the end of the eruption.

First approach: Here, digital elevation models (DEMs) created from pre-eruption and post-eruption photogrammetric images were obtained from the ALOS-PRISM instrument. PRISM data were successfully used to develop high-resolution DEMs of the Redoubt Volcano and Drift River valley, to examine the extent and height of emplaced lahar deposits and scour, and to estimate the volume of the 2009 Redoubt lava dome. Second approach: Here, combined PRISM-DEMs with microwave PALSAR data were used to demonstrate the utility of multi-sensor differential interferograms and produce cm-scale deformation maps of lahars in the Drift River valley. Third approach: Here, an algorithm was developed that mapped outlines of lahar deposits from multi-temporal coherence maps. The algorithm is unique in that it takes full advantage of all available coherence data in several post eruptive InSAR pairs to reduce noise and false alarms in creating an automatic lahar mask.

As a result of these combined multi-sensor and multi-temporal datasets, an improved description of this event was established. The ability to quantify lava dome volumes and lahar areas are examples of this achievement. Furthermore, the multi-sensor combination of optical and SAR data enabled the measurement of lahar deformation to an accuracy that would not have been achievable from processing each dataset individually.

Chapter two, entitled “Pyroclastic Flow Deposits and InSAR: Analysis of Long-Term Subsidence at Augustine Volcano, Alaska,” involves a study of pyroclastic flow deposits (PFDs) from Augustine Volcano, situated on Augustine Island, in Alaska’s Cook Inlet. Augustine Volcano is an extremely active volcano, having erupted at least six times since its first documented eruption in 1883, with its most recent eruption in 2006. During those six eruptions, significant pyroclastic flows occurred in 1964, 1976, 1986, and 2006 (Cervelli et al., 2006; Power et al., 2006; Coombs et al., 2010)

In this chapter, 16 years of InSAR data from multiple SAR platforms were acquired to examine the thickness and long-term subsidence behavior of PFDs at Augustine Volcano. A total of 48 SAR images were obtained from four separate SAR sensors: ERS-1, ERS-2, Radarsat-1, and ALOS PALSAR. The results of the research included a model to (1) decompose the deformation signals from two generations of superimposed pyroclastic flow deposits emplaced during the 2006 and 1986 eruptions, and to (2) develop a reconstructed subsidence history of the observed pyroclastic flows.

By combining these various datasets, we determined the initial settling period of the PFDs on Augustine was concluded within the first year of emplacement. We were also able to show a decrease in deformation rates over time, as cooling rates of the flows subsided. Through a combination of multiple SAR data resources acquired at different times, different geometries, and from several platforms, a better understanding of the behavior and geometry of Augustine's PFDs beyond what would have been possible from a single sensor was possible and provided critical information that could be useful for further hazard assessment.

The third and final Chapter of this dissertation is entitled, "Multi-sensor remote sensing data applied to estimation of 2012-13 effusion rates at Tolbachik Volcano, Kamchatka Peninsula, Russian Far East." This is a multi-sensor study of the effusive Tolbachik Fissure Eruption (TFE) on the Kamchatka Peninsula during 2012-2013. Tolbachik Volcano is situated in the central Kamchatka depression, on the Kamchatka Peninsula in southeastern Russia. The TFE occurred over nine months, from 27 November 2012 through ~27 August 2013 and deposited volcanic products over a reported area between 35.9 km^2 and 45.8 km^2, with a non-DRE (dense rock equivalent) volume variously estimated between 0.53 km^3 and 0.65 km^3 (0.50 km^3 DRE and 0.55

km^3 DRE). (Dvigalo et al., 2014; Belousov et al., 2015; Dai and Howat, 2017; Kubanek et al., 2017).

The approach developed in this third chapter focused on the use of thermal data from the National Oceanic and Atmospheric Administration (NOAA) Advanced Very High Resolution Radiometer (AVHRR) sensors, a high-temporal resolution but low-spatial resolution dataset, in combination with a time series of twelve highly accurate DEMs derived from X-band SAR data, obtained by the TanDEM-X satellite-radar mission operated by the German Aerospace Center, Deutches Zentrum für Luft und Raumfahrt (DLR). The objective was to improve the eruption profile of the TFE, and obtain more rigorous estimates of time averaged discharge rates from the volcanic activity during the nine months of the eruption. Although the TanDEM-X data have a very high spatial resolution, only twelve DEMs over nine months left large temporal gaps between observations over the course of the eruption. Using the thermal anomalies recorded from the AVHRR data as evidence of lava flow emplacement and summit effusion, multiple AVHRR observations were interleaved between TanDEM-X acquisition points and interpolated to form more precise estimates of the magnitude and timing of significant effusive periods. The method substantially increased the precision with which the eruption profile of the TFE and possibly other effusive eruptions can be estimated.

Introduction references

Belousov, A., Belousova, M., Edwards, B., Volynets, A., and Melnikov, D., 2015, Overview of the precursors and dynamics of the 2012–13 basaltic fissure eruption of Tolbachik Volcano, Kamchatka, Russia: Journal of Volcanology and Geothermal Research, v. 307, p. 22-37, doi: 10.1016/j.jvolgeores.2015.06.013.

Cervelli, P.F., Fournier, T., Freymueller, J., and Power, J.A., 2006, Ground deformation associated with the precursory unrest and early phases of the January 2006 eruption of Augustine Volcano, Alaska: Geophysical Research Letters, v. 33, p. L18304, doi: 10.1029/2006gl027219.

Coombs, M.L., Bull, K., Vallance, J.W., Schneider, D., Thoms, E.E., Wessels, R.L., and McGimsey, R., 2010, Timing, distribution, and volume of proximal products of the 2006 eruption of Augustine Volcano, *in* Power, J.A., Coombs, M.L., and Freymueller, J., eds., The 2006 eruption of Augustine Volcano, Alaska: USGS Professional Paper 1769, p. 145-185.

Dai, C., and Howat, I.M., 2017, Measuring Lava Flows With ArcticDEM: Application to the 2012–2013 Eruption of Tolbachik, Kamchatka: Geophysical Research Letters, v. 44, p. 12,133-12,140, doi: 10.1002/2017gl075920.

DigitalGlobe, 2019, "About Us", Maxar Technologies, Inc., Westminster, Colorado, https://www.digitalglobe.com/company/about-us, accessed 1 March 2019.

Dvigalo, V.N., Svirid, I.Y., and Shevchenko, A.V., 2014, The first quantitative estimates of parameters for the Tolbachik Fissure Eruption of 2012–2013 from aerophotogrammetric observations: Journal of Volcanology and Seismology, v. 8, p. 261-268, doi: 10.1134/s0742046314050029.

ESA, 2011, "ESA missions: observing the earth", European Space Agency, http://www.esa.int/esaEO/SEMGWH2VQUD_index_0_m.html, accessed 21 January 2015.

Kubanek, J., Westerhaus, M., and Heck, B., 2017, TanDEM-X time series analysis reveals lava flow volume and effusion rates of the 2012–2013 Tolbachik, Kamchatka fissure eruption: Journal of Geophysical Research: Solid Earth, v. 122, p. 1-21, doi: 10.1002/2017JB014309.

Morena, L.C., James, K.V., and Beck, J., 2004, An introduction to the RADARSAT-2 mission: Canadian Journal of Remote Sensing, v. 30, p. 221-234, doi: 10.5589/m04-004.

Olsen, E.T., *ed.*, 2017, AIRS/AMSU/HSB Version 6, data release user guide: Pasadena, CA, Jet Propulsion Laboratory, California Institute of Technology, 67 p.

Power, J.A., Nye, C.J., Coombs, M.L., Wessels, R.L., Cervelli, P.F., Dehn, J., Wallace, K.L., Freymueller, J.T., and Doukas, M.P., 2006, The reawakening of Alaska's Augustine Volcano: Eos Transactions, AGU, v. 87, p. 373-377, doi: 10.1029/2006EO370002.

USGS, 2010, "Earth Observing 1 (EO-1) , Sensors - Hyperion", U.S. Geological Survey, Earth Resources Observation and Science (EROS) Center, Souix Falls, SD, https://archive.usgs.gov/archive/sites/eo1.usgs.gov/hyperion.html, accessed September 30, 2018.

Chapter 1

Multi-sensor data fusion for remote sensing of post-eruptive deformation and depositional features at Redoubt Volcano[1]

1.1 Abstract

Monitoring volcanic activity by remote sensing is an essential component of volcanology. Remote sensing includes a variety of different sensing methods and instruments that collect data across a wide range of the electromagnetic spectrum. This study presents an overview of the improvements that are available to remote sensing imaging with multi-sensor and multi-temporal data fusion of optical and radar data, using Redoubt Volcano and related 2009 Drift River lahar deposits as a target area. From data acquired by the Panchromatic Remote Sensing Instrument for Stereo Mapping aboard the Advanced Land Observing Satellite, high resolution digital elevation models were produced and used to generate elevation change maps of Redoubt Volcano and the Drift River, and to estimate the volcano's dome volume; these digital elevation models were then fused with data from the Advanced Land Observing Satellite’s Phased Array type L-band Synthetic Aperture Radar to produce differential interferograms demonstrating the effect of high-resolution digital elevation models on surface deformation measurements from interferometric radar data; and finally, multi-temporal, interferometric synthetic aperture radar coherence data were used to plot the boundaries of lahar flows at the distal end of the Drift River with high accuracy. These techniques demonstrate: (1) how the fusion of data from multiple sensors acquired at multiple temporal intervals can substantially increase the accuracy and

---

[1] Previously published as McAlpin, D., and Meyer, F.J., 2013, Multi-sensor data fusion for remote sensing of post-eruptive deformation and depositional features at Redoubt Volcano: Journal of Volcanology and Geothermal Research, v. 259, p. 414-423, doi: 10.1016/j.jvolgeores.2012.08.006.

precision of remote sensing measurements compared to those from one sensor alone; (2) how data fusion techniques can improve remote sensing change detection in areas otherwise ill-suited for single sensor observations; and (3) how data subject to temporal decorrelation may be used for boundary mapping with high accuracy. In addition to volcanic deformation, these methods can be applied to a number of disciplines, and will become more essential as the number of earth observing satellites increase.

1.2 Introduction

Surface deformation near volcanoes and measurement of deposits left behind by an eruption are major topics of volcano research. Measurement of the thickness, volume, and area of a volcano's erupted material is a key element of understanding its magmatic plumbing and the capacity of its magma supply. In addition, the nature and extent of secondary effects, such as lahars and flash floods are of first order interest to emergency responders, public health officials, and others.

Examination of volcanic activity by remote sensing from Earth observation satellites is an essential element of modern volcanology. The number of these satellites, along with the sophistication and capabilities of the instruments they carry has increased greatly since the first Earth Observing satellite, the Earth Resources Technology Satellite (ERTS), also known as Landsat-1, was launched in 1972 (USGS, 2003).

Remote sensing instruments for volcanology now cover a wide range of the electromagnetic spectrum. Sensors from both space borne and airborne platforms collect data across the optical, infrared, microwave, and ultraviolet spectrums, with each instrument generally addressing a specific task. Infrared data, for instance, are particularly suited for detecting eruptive activity; microwave and interferometric synthetic aperture radar (InSAR) for deformation patterns and ash detection; ultraviolet (UV) data for gas emissions; visual and infrared (VIR) data for thematic mapping, LIDAR for digital surface models, and so on.

Until the early 1990s, remote sensing of volcanic activity was generally the province of these single sensor techniques. As the number of satellites and sensors increased, however, and along with them the quantity and quality of data, the need to integrate data from different sources and at different levels of quality became apparent (Gong, 1994). Moreover, for many applications, single-sensor data were either unresponsive or incomplete (Simone et al., 2002).

More recently, fusion of multi-sensor or multi-temporal remote sensing data have become more prevalent in volcanology, with the creation of advanced algorithms and processing techniques that create increased confidence, reduced ambiguity, improved reliability, and improved classification (Rogers and Wood, 1990). Examples include processing of multiple synthetic aperture radar (SAR) images into InSAR deformation images (Lu et al., 2000; Rosen et al., 2000; Lundgren et al., 2001), InSAR decorrelation imaging to detect topographic modify-cation (Lu et al., 2005),multiple InSAR images to produce digital elevation models (DEMs) (Honikel, 1998; Lu et al., 2003), and integrating SAR and InSAR data with visual and infrared (VIR) images to achieve an entire range of products with more information that can be derived from each of the single sensors' data alone (Pohl and Van Genderan, 1998; Lu et al., 2010).

In this paper, we use optical, SAR, and InSAR data from the Drift River valley and Redoubt Volcano (Redoubt) to demonstrate how fusion of photogrammetrically derived, high resolution DEMs were used to identify pre- and post-eruption elevation changes; that fusion of high resolution, up-to-date DEMs with InSAR images can significantly improve deformation maps of lahar inundated areas; and how decorrelation maps produced by pre- and post-eruption SAR analysis can effectively map the boundaries of a series of lahars that occurred there in March–April of 2009.

For purposes of this paper, digital elevation model (DEM) is used interchangeably with the related concept of a digital surface model (DSM). DSMs differ from DEMs by taking into account surface heights of natural and man-made objects like buildings, trees, and hedges (Toutin, 2004). Within the target areas of this study, the difference between DSMs and DEMs would have negligible effects. Readers, however, should be aware of this difference when contemplating the application of these methods to other areas.

1.3 Background

Redoubt Volcano and the Drift River valley are located in south-central Alaska, approximately 160 km southwest of Anchorage (Figure 1.1). The Drift River is a braided stream that carries a heavy sediment load eastward from the Alaska Range to Cook Inlet. Approximately 37 km upstream from its Cook Inlet terminus, the Drift River valley is abutted on its south side by the piedmont lobe of an informally named "Drift glacier," which descends the north flank of the heavily glaciated, 3108 m high Redoubt Volcano from a breach in its summit crater (Till et al., 1994). From there, the river flows east to the Cook Inlet, where it forms an arcuate delta just north of the Drift River Oil Terminal (DROT), a petroleum storage facility along the coast (Figure 1.1).

Redoubt Volcano is one of five volcanoes in the Cook Inlet region, and the second most active during historical times (Riehle, 1985). Prior to 2009, historical eruptions occurred in 1902, 1966, 1967–1968, and 1989–1990, with additional vapor emission episodes observed in 1933, 1965, and 1967 (Wilson and Forbes, 1969; Miller et al., 1998). The 1989–1990 eruption was a relatively large eruption, that, in economic terms, was second only to Mount St. Helens' 1980 eruption as the most costly in U.S. History (Tuck et al., 1992). Nearly 19 years later, precursory activity in the form of glacier melt, gas emissions, phreatic explosions, and elevated seismicity

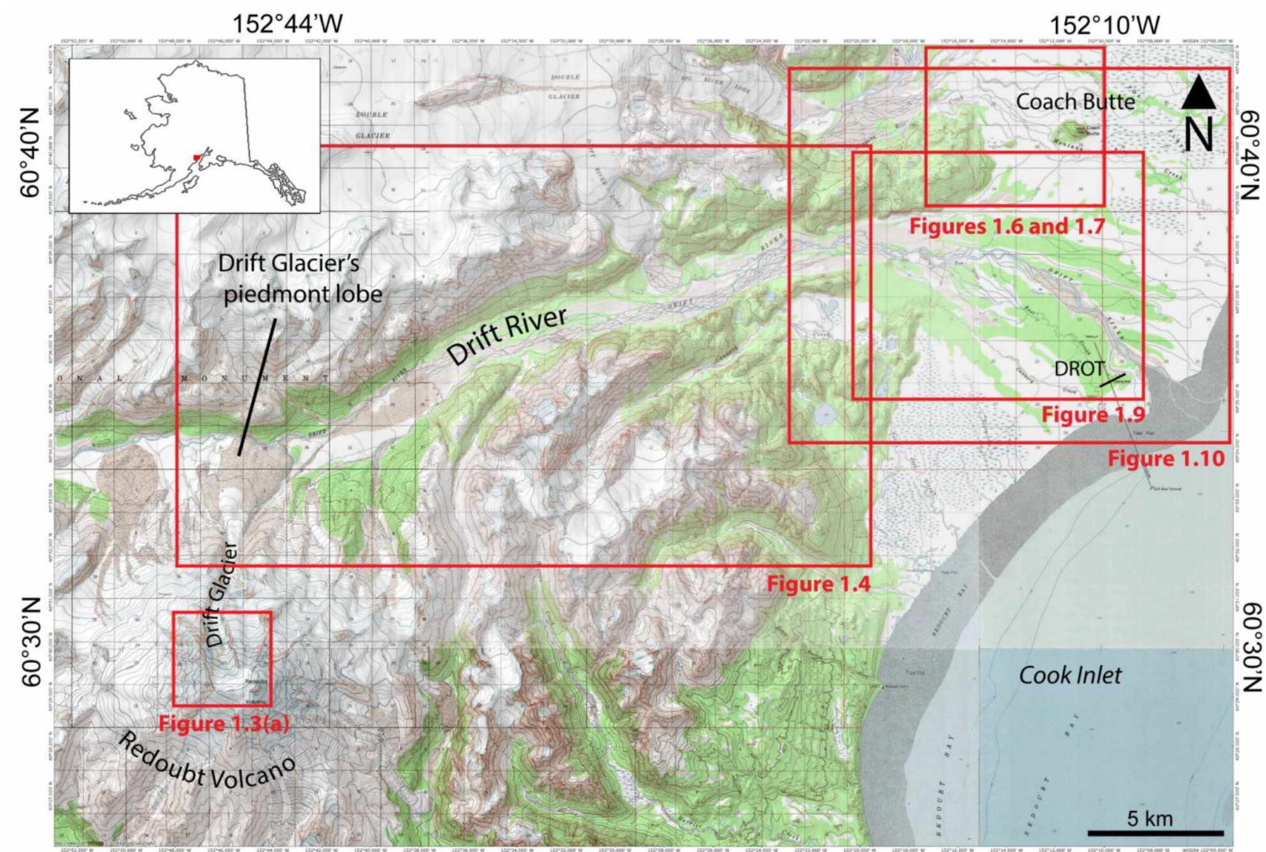

Figure 1.1: Topographic map of the Drift River valley, including Redoubt Volcano in south-central Alaska. Red rectangles identify location of subsequent figures mentioned in text. Base map provided courtesy of TOPO! © 2011 National Geographic.

were detected and monitored by the Alaska Volcano Observatory. These precursory events continued for seven months, from July 2008 through early March 2009, when, on 22 March 2009, Redoubt erupted in a series of powerful explosive events. The eruption sent ash to altitudes exceeding 18 km, and produced pyroclastic flows and associated lahars that inundated the Drift River valley (Schaefer, 2012). The explosive phase of the eruption continued for 13 days, during which 19 explosive events were observed, and at least two domes formed and collapsed. Water and mud from the Drift glacier's melt water filled the river valley, causing flash flooding and lahar flows in the Drift River valley (Schaefer, 2012; Bull and Buurman, 2013b).

The explosive phase of the eruption ended on 4 April 2009 when two explosive events created an ash cloud>15 km high, with additional pyroclastic flows, lahars, and the final dome collapse of the eruption. Following these events, an effusive stage began as the final dome began to form in the summit crater. Dome growth continued through the end of the eruption period on 1 July 2009 (Schaefer, 2012).

The concerns over lahars, ash fall, and other consequences of a Redoubt Volcano eruption are significant. An eruptive event at Redoubt Volcano presents a considerable economic hazard to the City of Anchorage, its key transportation and military facilities, and has the potential to severely disrupt the area's air travel and commerce. The residential community of Tyonek (pop. 171) is approximately 110 km north of the Volcano, and the communities of Kenai (pop. 7100) and Nikiski (pop. 4493) are located 80 km eastward across Cook Inlet (CIS, 2011). In the event of an eruption, accurate information on the distribution and likelihood of lahars, pyroclastic flows, and ash fall will be needed to assess the threat to people and property in the vicinity. Critical to this type of hazard analysis will be information about past flow behavior, and the direction and potential volume of mud, debris, ash, and water that might be expected.

In good weather, two dimensional examination of lahar deposits can be easily accomplished by space borne or airborne visible-infrared (VIR) sensors. In coastal areas however, clear weather may only rarely coincide with a satellite revisit period, or the availability of very expensive aircraft fitted with equally expensive instruments. VIR images are also unable to provide deformation or volume data at the centimeter scale needed to examine volcanic deposits.

SAR data are not weather dependent, but the presence of speckle often renders them difficult to interpret. Moreover, individual SAR images may suffer from distortions caused by layover or foreshortening. To minimize those problems, SAR data acquired at different spatial and temporal intervals may, under certain conditions, be combined into interferometric SAR (InSAR) images that detect centimeter-level deformation. Among other conditions, InSAR processing in rapidly changing volcanic environments requires high-resolution, up-to-date DEMs of the target area and high coherence between SAR images acquired at different times.

To examine lahar deposits in the Drift River valley, to analyze topographic changes of the Redoubt edifice associated with its 2009 eruption, and to determine deformation signals due to contraction of lahar deposits, image data were used from two separate instruments aboard the Advanced Land Observing Satellite (ALOS), launched by the Japan Aerospace Exploration Agency (JAXA) in 2006 (Rosenqvist et al., 2007). Optical images were obtained from the Panchromatic Remote Sensing Instrument for Stereo Mapping (PRISM), and microwave imaging data from the Phased Array type L-band Synthetic Aperture Radar (PALSAR) sensor.

The ALOS-PRISM instrument consists of three independent panchromatic radiometers for simultaneous nadir, forward, and backward directions. This configuration results in along-track stereoscopy in overlapping three images (triplets), each with 35 km coverage, and horizontal resolution at nadir of 2.5 m. This permits processing of PRISM's optical data into highly accurate DEMs (Tadono et al., 2004). The ALOS-PALSAR instrument is a fully polarimetric, active microwave sensor using L-band frequency to achieve all-weather, day-and-night, land observation. In its fine-beam mode, PALSAR offers ground resolution as high as 10×10 m in a 70 km swath (Rosenqvist et al., 2007).

1.4 Fusion of optical data for DEM generation and topographic change detection

1.4.1 Methods

To produce DEMs of the Drift River valley, radiometrically corrected (PRISM level 1B1) triplet images of the target area during pre-eruption and post-eruption time frames were obtained from the Alaska Satellite Facility (ASF). The pre-eruption triplet was acquired by PRISM on 21 September 2007, with a post-eruption triplet acquired on 26 September 2009. Acquisition dates for PRISM data may not precisely match time sensitive events, because the optical data require cloud-free skies and an absence of seasonal snow cover. Clouds and snow are particularly important, because they can obscure tie points necessary for photogrammetry and orthorectification. Unavoidable clouds, as well as featureless areas like large snowfields, and bodies of water, were masked out of the image to avoid anomalous processing results.

From the triplet data, PRISM-DEMs and panchromatic orthorectified optical images were generated simultaneously with "DSM and ORI Generation Software for ALOS-PRISM" (DOGS-AP) provided by the JAXA Earth Observation Research Center. Processing with DOGS-AP consists of two stages: orientation and DSM generation. Orthorectified images (ORIs) are optionally produced during DSM generation. Orientation is a relative image orientation using tie points (TPs) within the target scene, although an absolute orientation is possible if ground control points (GCPs) are available. DSM generation is an area-based, image matching algorithm that accounts for image characteristics and PRISM's unique sensor configuration in a semi-automatic operation (Takaku and Tadono, 2009).

From the two sets of triplets, DOGS-AP produced a DEM and an ORI of the target area for each date.

To derive topographic change from the multi-temporal PRISM-DEMs, the processed DEMs were converted to GeoTIFF files, stacked, and elevation values of the pre-eruption, 2007 image were subtracted from the post-eruption, 2009 image. The result is an elevation change map with increases in elevation represented by positive values, and decreases in elevation represented by negative values.

1.4.2 Validation of methods

To evaluate the accuracy of the derived elevation difference product, a validation of measurements was performed using test sites whose topography did not change during the period of observation. For these sites, elevation differences between pre-eruptive and post-eruptive DEMs are expected to be zero and elevation difference measurements can be compared to this expectation to determine biases and noise level of the observations. The validation sites were selected near the four corners of the DEM area to allow for the identification of potential tilting between repeated DEMs.

As shown in Figure 1.2, the distribution of elevation difference measurements within the validation sites was found to be Gaussian with a mean value, or bias ($\mu_{\Delta h}$), of 11 m and a

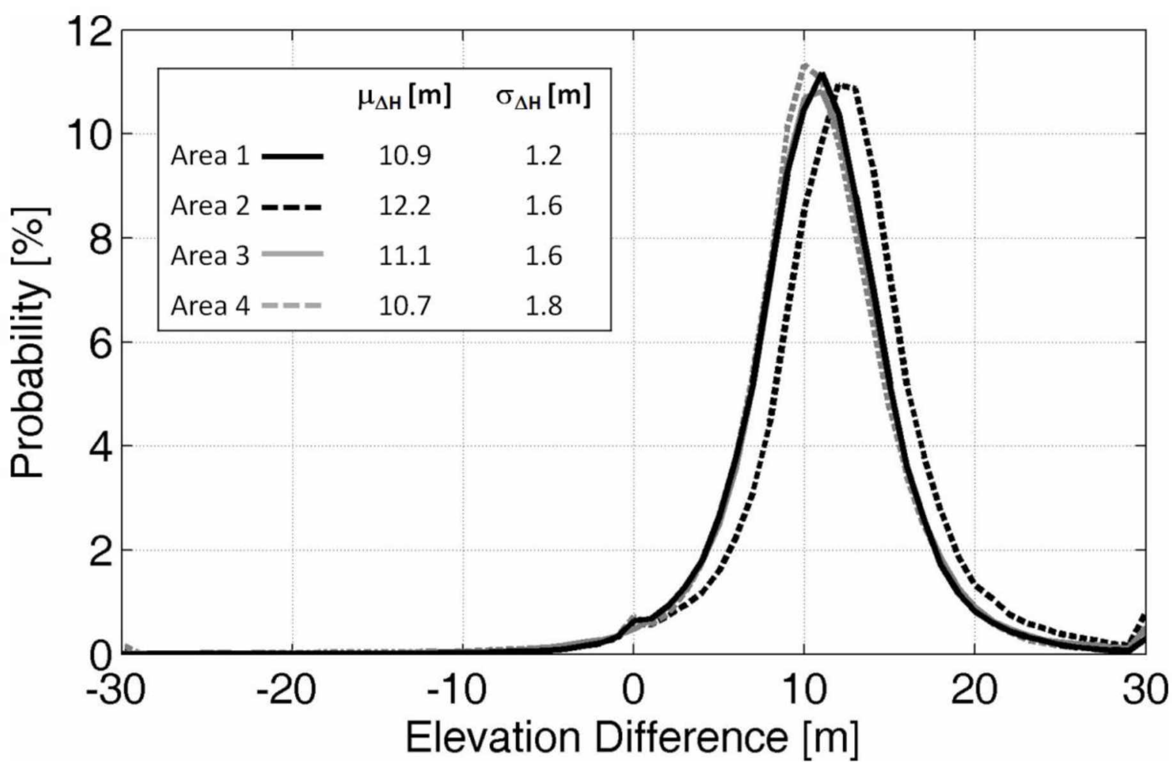

Figure 1.2: Distribution of elevation differences between repeated PRISM DEMs. Height differences were analyzed for four validation sites located near the four corners of the DEM area that did not show topographic changes during the period of observation. The expected difference in the validation sites should be zero, while the actual measurements show a consistent mean difference of ~11 m, and a standard deviation of less than 2 m. The consistency of the measurements suggests a constant offset between the DEMs that can be removed in a post-processing procedure. The results compare well to a similar study of PRISM-DEM height accuracy by Takaku and Tadono (2009), who found bias over varying terrains ranging from −16.44 to 6.93 m, and standard deviations between 4.91 and 8.7 m.

standard deviation ($\sigma_{\Delta h}$) of less than 2 m. Both bias and standard deviation are consistent for the four test sites, indicating that no tilting between DEMs could be identified. These results compare well to a similar study of PRISM-DEM height accuracy by Takaku and Tadono (2009), who found biases over varying terrains ranging from ~16.44 to 6.93 m, and standard deviations between 4.91 m and 8.7 m.

The 11 m offset of our measurements can be attributed to uncertainties in the absolute position of the instrument's orbit paths, and can be removed by using ground control points in the DEM generation process or by subtracting the offset in a post processing step. Ground control points were not present in the low elevations of the Drift River valley. To support the geophysical interpretation of the elevation difference maps, we have therefore removed the 11 m offset using the latter approach.

1.4.3 Geophysical results

1.4.3.1 Summit and dome

An elevation difference map for Redoubt Volcano, representing the difference between pre-eruption and post-eruption DEMs is shown in Figure 1.3(a). The elevation differences are overlain on the post-eruption PRISM-ORI from 2009 and are shown in a color representation with dark red corresponding to 100 m of topography increase and dark blue showing 100 m of elevation reduction.

As expected, the Drift glacier shows pronounced elevation reduction representing ice loss during the eruption. Similarly, a dark blue area of elevation loss in the summit crater reflects evacuation of accumulated snow/ice during the explosive eruption phase in March and April of 2009. The red area on the north edge of the summit crater is new topography produced by growth of the final 2009 lava dome. The elevation difference map reflects the dome's maximum change

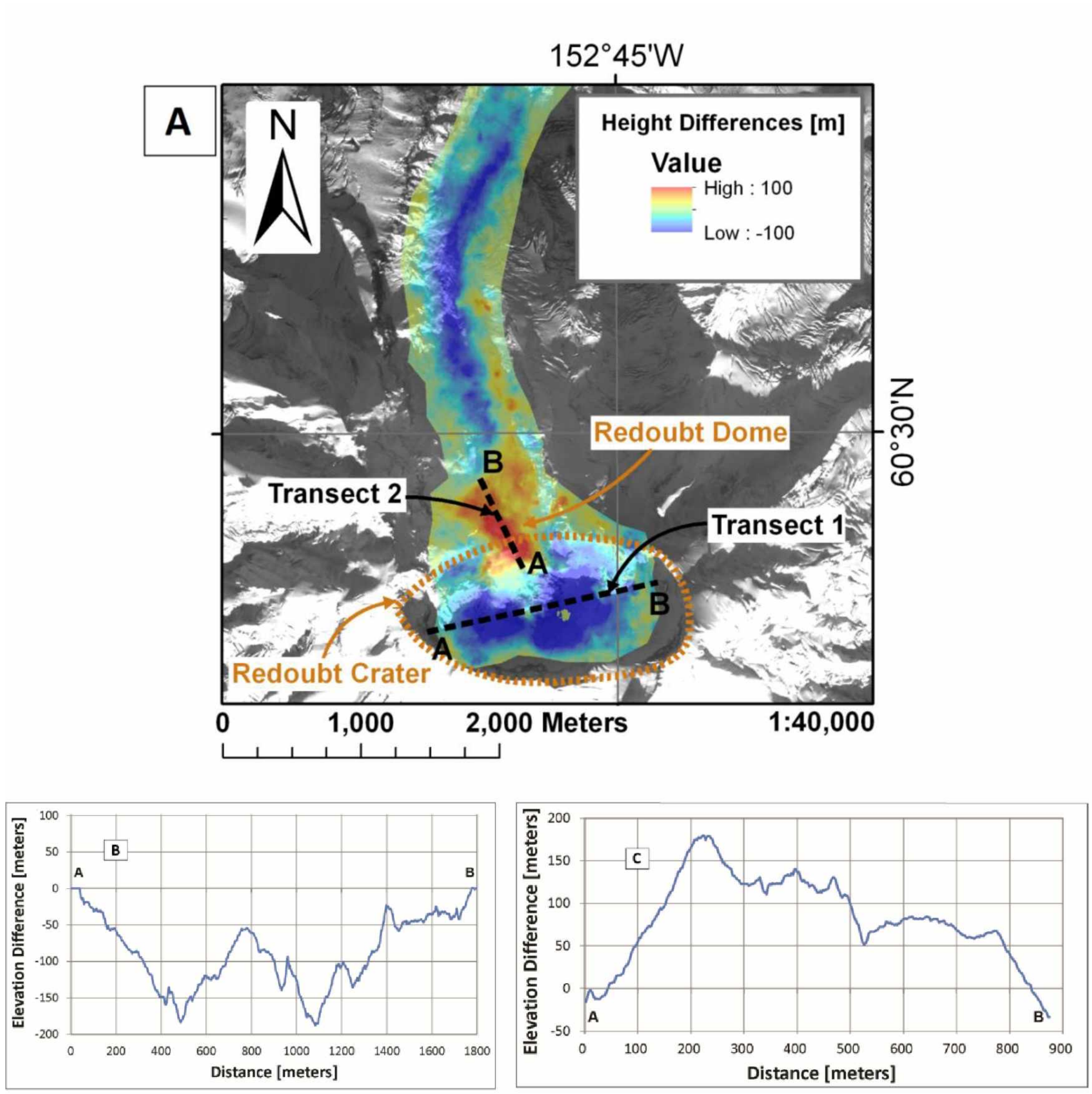

Figure 1.3: (a) Elevation change map of Redoubt Volcano and the Drift glacier, produced by subtracting a pre-eruption DEM dated 21 September 2007, from a post-eruption DEM dated 26 September 2009. The resulting pre- and post-eruption elevation differences (color coded), are overlain on a panchromatic orthorectified PRISM image. Locations of the crater and dome are outlined in brown. Elevation increases are shown in yellow and red; decreases in cyan and blue. (b) Elevation change profile across the summit crater (Transect 1 in a) indicates reduced elevation caused by evacuation of accumulated snow/ice during the explosive eruption phase in March and April of 2009. (c) Elevation change profile across final 2009 lava dome. Location of profile shown in a (Transect 2). These numbers suggest that much of the crater's elevation loss can be attributed to loss of glacier ice. Transect 2 (Figure 1.3c) follows the main shoulder of the dome from the southern end in the crater to its northern tip on the northern flank of the volcano. Close to 200 m of elevation gain are observed.

in elevation (from the south base to peak) to be a 200 m gain over 850 horizontal meters.

For further analysis, two transects were extracted from the elevation difference data. Transect 1 (Figure 1.3b), was drawn from the East across the summit crater to provide a quantitative measurement of elevation decrease in the crater. Up to 200 m of surface lowering can be measured in this area.

This observation compares well to Trabant and Hawkins (1997), who modeled ice thickness near Transect 1 at 135 m to 190 m prior to Redoubt's 1989–1990 eruption..

After the acquisition of the pre-eruption image triplet, but before the final dome began to grow on 4 April 2009, at least two previous lava domes were destroyed by explosive eruptions (Bull, 2009; Schaefer, 2012; Bull and Buurman, 2013a). The current and final lava dome is built on top of what remains of the first two domes. Consequently, where the new dome starts and the previous domes end is unknown. Likewise, the geometry of the final dome's underside is unknown, and whether its shape is flat, oblate, prolate, mushroom shaped, or some other variation may significantly affect its inferred volume. Because of these geometric uncertainties, a volume estimate of Redoubt's dome based on morphology requires some relatively broad underlying assumptions. In this study, we assume that the dome's basic shape is roughly that of a prolate spheroid, with a flat underside.

The volume, V, of a prolate spheroid is $4/3\pi a^2 c$, where a is the horizontal radius at the equator, and c is the vertical conjugate radius (Wolfram|Alpha, 2011). Measurements of the dome indicate an equatorial radius of 250 m and a polar radius of 514 m. Using a multiplier of 0.5 to account for the flat underside, the result is a geometric volume of 67.2×10^6 m^3. Although this is clearly a basic estimate, it compares favorably with estimates of 68×10^6 m^3 from Bull (2009), 65.7×10^6 m^3 from Dehn (pers. comm., 2012), and 72×10^6 m^3 from Diefenbach et al. (2013), and Bull and Buurman (2013b).

These results show that repeated DEMs generated from space borne platforms are generally useful to monitor a variety of surface changes at active volcanoes. As optical sensors such as ALOS PRISM require cloud free imaging conditions, latency times until a post-eruptive DEM can be acquired vary with conditions. If required, DEM time series can be augmented with other stereo-optical systems such as IKONOS and SPOT5 or by adding DEMs from radargrammetric analysis of SAR images.

1.4.3.2 Drift River lahars

As described earlier, the 2009 eruption of Redoubt produced significant lahars in the Drift River valley. We obtained three pre- and post-eruption PRISM triplets that cover the larger Drift River vicinity (acquired by PRISM on 21 September 2007 and 26 September 2009, respectively), starting at the Drift glacier's piedmont lobe in the west, to the river's eastern terminus in Cook Inlet. From these triplets, separate 2007 and 2009 DEMs were processed with DOGS-AP, and mosaicked together into single datasets. Subtracting the 2007 DEM from the 2009 DEM produced the elevation change map shown in Figure 1.4. In this figure, the elevation changes were color coded and overlain on the post-eruption PRISM-ORI from 2009.

Figure 1.4 provides important detail on the spatial elevation change patterns that remain from the lahar deposition period. Dark blue patterns represent areas where a combination of lahar flow and post-eruptive incision has caused local reduction of surface elevation. The data indicate significant deposition of 0.5–2.5 m (green to yellow) over a preponderance of the valley, with a mean elevation increase of 1.5 m between the piedmont lobe and the river delta. These measurements are in rough agreement with field estimates of Waythomas et al. (2013) and (Schaefer, 2012).

In a more localized area, a narrow gorge at the base of the Drift glacier reduced to bedrock by the 23 March 2012 lahar (Waythomas et al., 2013), the data show scour of more than 20 m (blue), while slightly east of the Drift glacier's piedmont lobe, there are localized areas of deposition up to 20 m (red). It can be assumed that most of this deposition is attributable to the

2009 lahars. There is, however, some uncertainty with respect to the elevation of the river bed both prior to the 2009 lahars, and later, between the lahars and the measurement date of 29

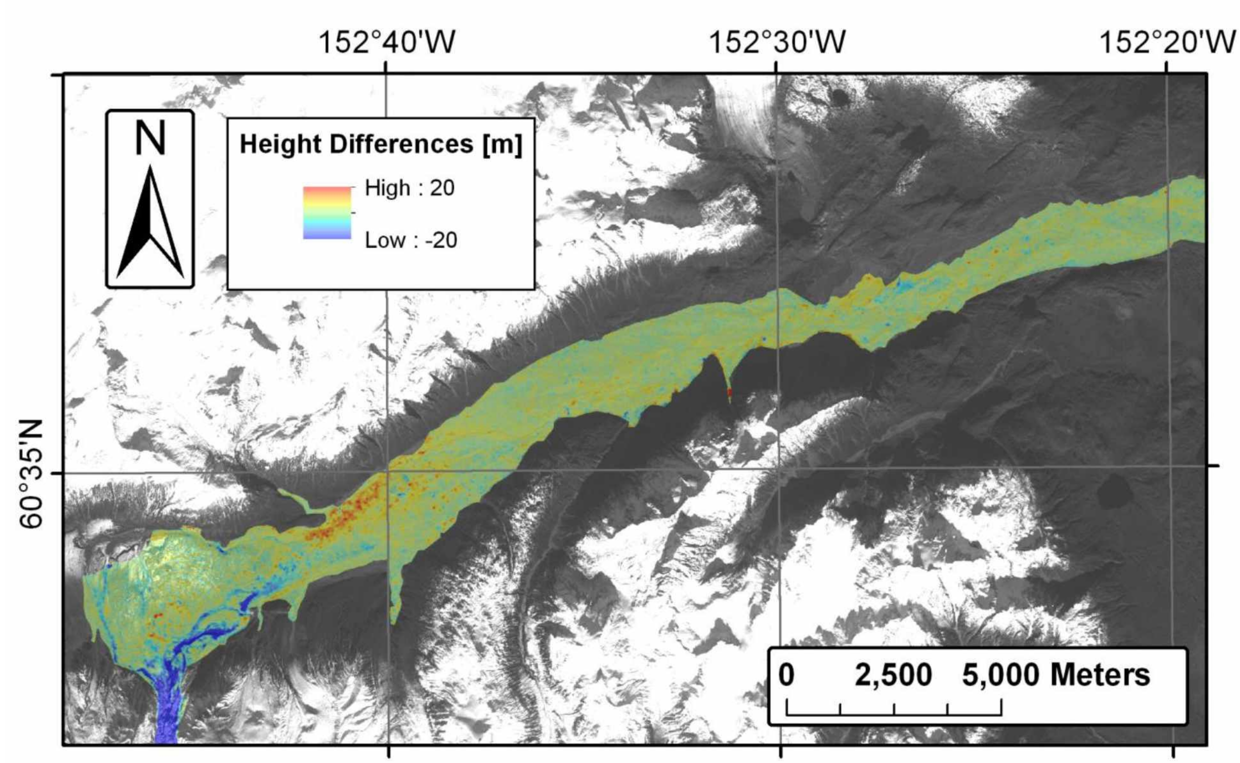

Figure 1.4: Elevation difference map of the western Drift River valley produced by subtraction of a mosaic of pre-eruption DEMs acquired on 21 September 2007, from post-eruption DEMs acquired on 26 September 2009. Shades of green, yellow, and red indicate elevation increases up to 20 m (red) between the two dates. Negative differences corresponding to scour appear as cyan and blue, to a decrease of 20 m. The elevation difference map provides great detail on the main flow patterns of the lahar, with dark stream patterns representing areas where most

September 2009. As Waythomas et al. (2013) point out, surface changes would be overstated if the riverbed was incising before peak flows began, and understated if the channel floor was aggrading before the peak flows began.

1.5 Fusion of optically-derived DEMs with InSAR for deformation detection

1.5.1 Methods

InSAR combines two or more SAR images acquired from almost identical locations to calculate phase differences. These phase differences, commonly referred to as interferometric phase, are a measurement of the path length differences between the positions of the radar antennas at the acquisition times and a resolution cell on ground. Conventionally, these path length differences can be largely attributed to either topographic height differences, depending on the relative positions of the SAR antennas, or to surface deformation.

To use InSAR for mapping surface deformation, the influence of surface topography on the observed phase measurements is removed in a process called differential SAR interferometry (d-InSAR). Conventionally, a reference elevation model is used to construct a synthetic topographic interferogram and remove it from the observed interferogram, resulting in a differential, topography-free interferogram. Time series analysis of stacks of multi-temporal differential SAR interferograms can then be used to monitor centimeter scale surface deformation over long time spans and with high spatial resolution. The potential of InSAR for monitoring geodynamic processes has been proven in the last decade by a wealth of studies where InSAR data were used for monitoring volcanic inflation (Amelung et al., 2000; Lu et al., 2000; Hooper et al., 2004), tectonic deformation (Wright et al., 2003; Chlieh et al., 2004; Ryder et al., 2007), surface subsidence in inner-city areas (Hoffmann et al., 2001; Meyer et al., 2007; Stramondo et al., 2008), oil exploration (Fielding et al., 1998), and landslide progression (Singhroy et al., 2007).

To analyze surface deformation associated with volcanic activity at Redoubt, ALOS-PALSAR single-look complex (SLC) data were obtained from ASF in multi-temporal InSAR stacks with the same beam mode, look angle, and bandwidth. Eighteen initial PALSAR images of the Drift River valley were obtained with a range of dates from 7 December 2006 through 18 December 2010 (Table 1.1 and Figure 1.5). From these eighteen images, two separate d-InSAR stacks were processed using the GAMMA RS software. The first d-InSAR stack (Subset 1 in Figure 1.5), was selected using only image sets spanning the eruptive period between 22 March 2009 and 4 April 2009. This stack was used to determine extent and boundaries of lahars. A second d-InSAR stack (Subset 2 in Figure 1.5), was created only from post-eruption acquisitions, and was used to determine average surface deformation rates once the lahar was emplaced. To maximize interferometric coherence and to minimize the effects of DEM errors on surface deformation estimates, a maximum interferometric baseline of 1.5 km, was imposed on all interferometric pairs.

Table 1.1: Details of PALSAR data obtained from the Alaska Satellite Facility. All images were acquired on ascending orbits, path 266. Off-nadir angle is 34.3°. Sensor mode is Fine Beam Dual Polarization (FBD) or Fine Beam Single Polarization (FBS) as indicated. Images marked with an asterisk denote post-eruption acquisition dates.

Granule	Acquisition date	Sensor mode
ALPSRP261001210*	12/18/2010	FBS
ALPSRP247581210*	9/17/2010	FBD
ALPSRP240871210*	8/2/2010	FBD
ALPSRP220741210*	3/17/2010	FBS
ALPSRP214031210*	1/30/2010	FBS
ALPSRP207321210*	12/15/2009	FBS
ALPSRP193901210*	9/14/2009	FBD
ALPSRP187191210*	7/30/2009	FBD
ALPSRP160351210	1/27/2009	FBS
ALPSRP146931210	10/27/2008	FBS
ALPSRP133511210	7/27/2008	FBD
ALPSRP106671210	1/25/2008	FBS
ALPSRP099961210	12/10/2007	FBS
ALPSRP086541210	9/9/2007	FBD
ALPSRP079831210	7/25/2007	FBD
ALPSRP073121210	6/9/2007	FBD
ALPSRP052991210	1/22/2007	FBS
ALPSRP046281210	12/7/2006	FBS

Based on these criteria, a total of nineteen interferograms were produced: ten post-eruptive, and nine spanning the eruptive period. The post-eruptive data stack spans a period of fourteen months between July 2009 and September 2010. After compensating for topographic phase components, both data stacks were processed using a small baseline subset (SBAS) time-series analysis algorithm as described by Berardino et al. (2002) in order to determine surface deformation signals. SBAS provides convenient methods for the mitigation of the effects of atmosphere and for orbital uncertainties (Lee et al., 2010).

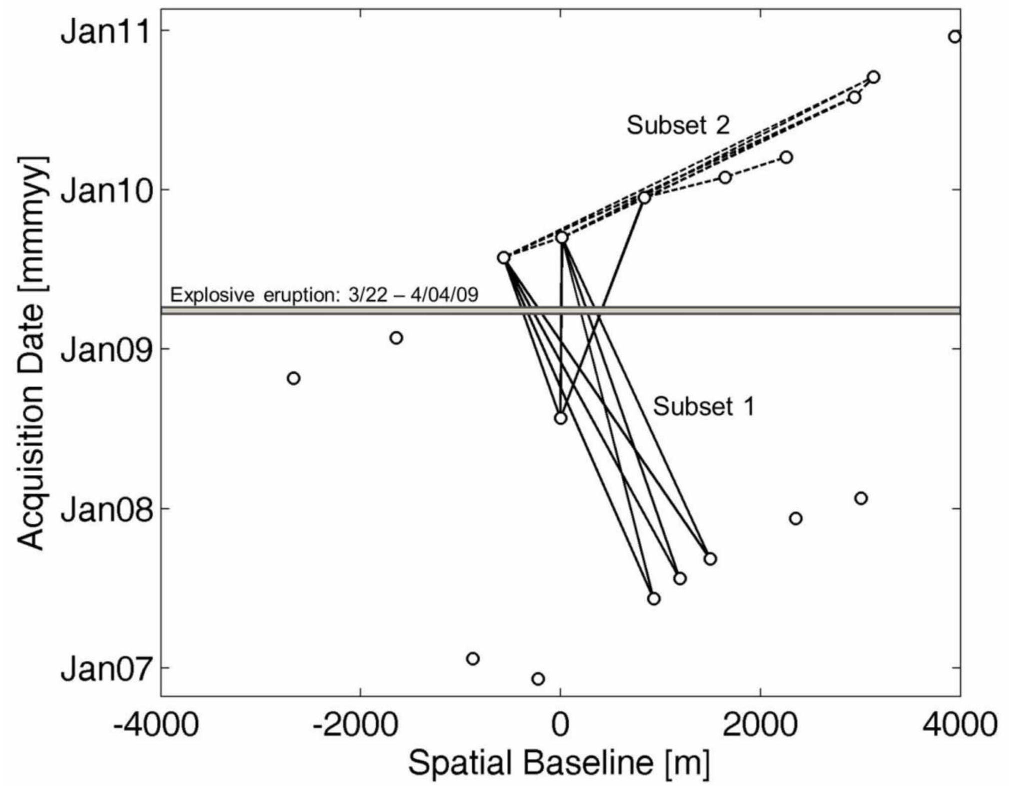

Figure 1.5: Time-baseline diagram of SAR data used for small baseline subset (SBAS) processing near Redoubt Volcano Circles identify SAR acquisitions by their acquisition date and spatial baseline relative to PALSAR image ALPSRP133511210 acquired on 27 July 2008. Lines indicate interferograms formed from the available acquisitions. Two different interferogram subsets were formed for SBAS processing. Subset 1 (solid lines), consists of image pairs that cross the explosive eruptive period and was used to map the extent of emplaced lahars. Subset 2 (dashed lines), contains only post-eruptive images, and was used to map cm-scale lahar deformation after the end of the explosive phase of the 2009 Redoubt eruption. Acquisitions not connected by lines were excluded from the InSAR analysis due to long spatial baselines, strong seasonal decorrelation effects, or both.

Correction of topographic phase components is a critical step in d-InSAR processing because residual topographic phase signals can lead to biases in surface deformation estimates. Although methods exist to remove residual topographic phase from time series of d-InSAR data (e.g., Lanari et al., 2004), these require the spatial baselines within a d-InSAR stack to be random in time.

Time correlated spatial baselines, a characteristic typical of ALOS PALSAR (Samsonov, 2010), can be observed can be observed in Subset 2 of our SAR data stack (Figure 1.5), and render methods for mitigating residual topographic signals ineffective. In these circumstances, high quality, up-to-date topographic information mitigates the effect of residual topographic phase, and becomes imperative for precision d-InSAR analysis. To demonstrate the benefit of fusing up-to-date information from multiple sensors on the sensitivity and accuracy of d-InSAR-based deformation monitoring, each of the d-InSAR stacks were processed in two separate runs.

In the first processing run, referred to here as the reference run, correction of topographic phase terms was attempted using a DEM obtained from the National Elevation Dataset (NED) (Figure 1.6). While in many areas DEMs derived from the Shuttle Radar Topography Mission

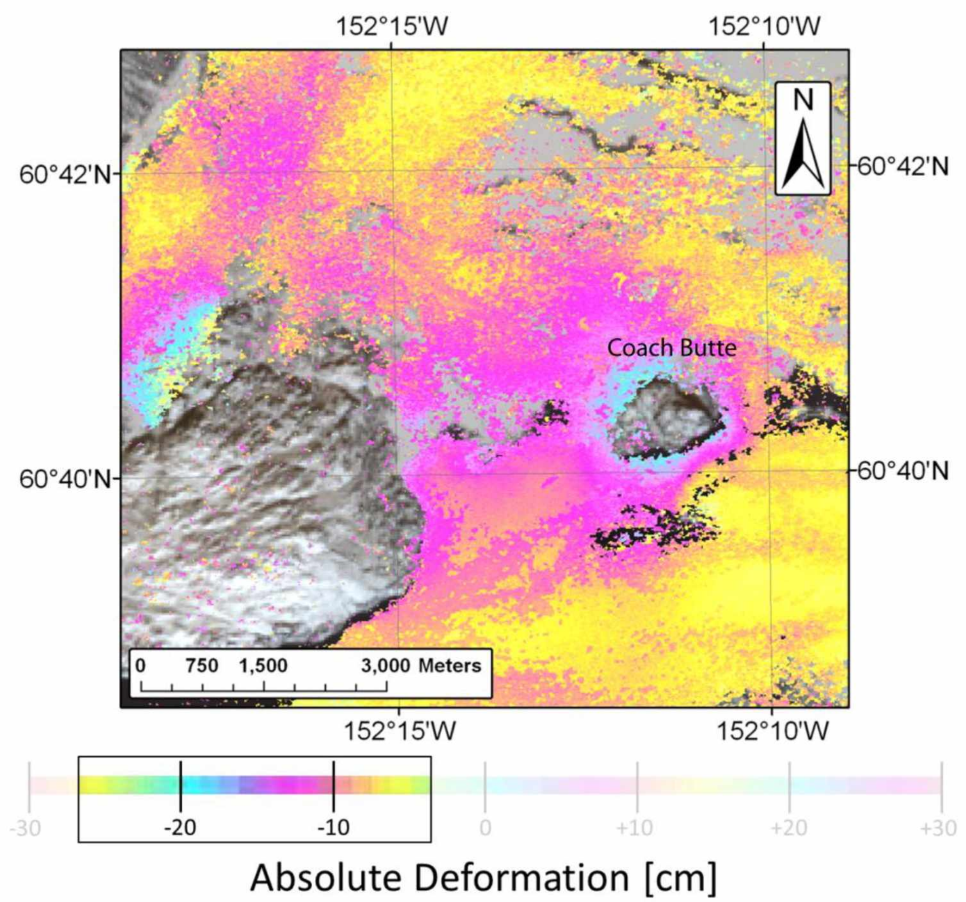

Figure 1.6: Interferometric deformation map with topographic phase terms corrected with a DEM obtained from the NED, and shown overlain on an EO-1/ALI visible-light image acquired on 4 April 2009. The horizontal resolution of the NED in Alaska is limited to 2 arc seconds, or ~60 m. This relatively coarse resolution, combined with infrequent updates to the NED dataset, likely result in differences between an NED-DEM and the actual topography. The associated errors in topographic phase correction cause biases in estimated surface deformation rates of about −10 to−20 cm yr^{-1} in this non-deforming area.

(SRTM), have a higher, 30 m resolution, they are not available for latitudes above 60°N (van Zyl, 2001). DEMs obtained from the NED have the advantages of low cost, high availability, and wide coverage, which make them a popular data source for d-InSAR processing. NED-DEMs, however, are not always optimum for topographic analysis. Their horizontal resolution in Alaska is limited to 2 arc seconds, or approximately 60 m (Gesch et al., 2009), and infrequent updates likely result in differences between the DEM and current topography, especially in rapidly changing fluvial and coastal environments. This dataset, therefore, was used primarily as a reference point.

In the second processing run, a fusion of up-to-date information from multiple satellite sensors was attempted, whereby topographic correction of the InSAR phase was based on the previously derived PRISM-DEMs (Figure 1.7). These DEMs, with much greater horizontal accuracy and availability for both pre- and post-eruption time frames, allowed every interferogram to be corrected with the most appropriate (in time) topographic signal, and to therefore improve the sensitivity and accuracy of InSAR-derived deformation estimates.

1.5.2 Performance assessment of fusion approach

To assess the performance of the data fusion process, estimates of surface deformation rates were derived for an area including the eastern end of the Drift River valley and the Drift River Delta using the ten post-eruptive interferograms that were processed with both reference and PRISM-derived DEMs. The resulting surface deformation rates were then compared to GPS observations for validation.

Available GPS observations in the study area were obtained from a local network of 14 GPS benchmarks described by Grapenthin et al. (2013). Two of these 14 GPS stations are located in the direct vicinity of the area of interest and are used for validation. These stations include a permanent station (station ID AC17) and a campaign station (QRRY) that was occupied both before and after the eruption.

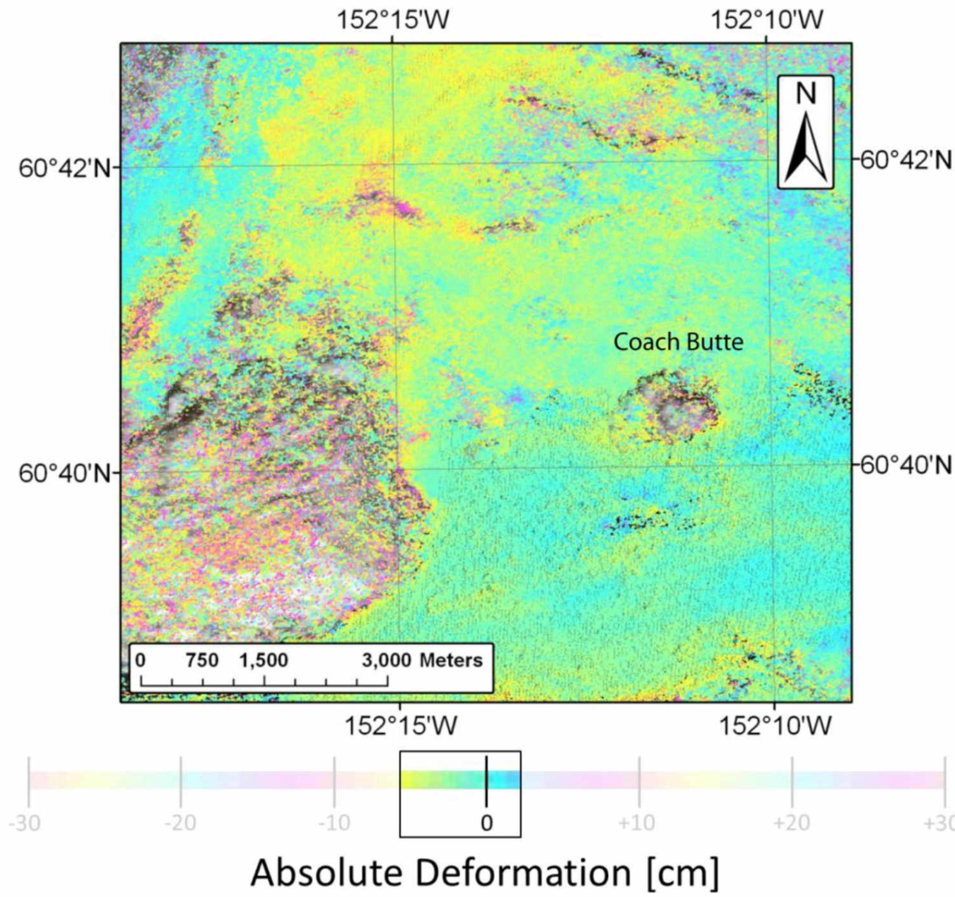

Figure 1.7: InSAR-derived surface deformation map with topographic phase terms corrected with a DEM producedphotogrammetrically from PRISM data, and shown overlain on an EO-1/ALI panchromatic image. The greater resolution and higher accuracy of the PRISM data reduced biases in surface deformation rate estimates significantly compared to the results shown in Figure 1.6.

After a global trend model was removed from the data, the GPS observations revealed only a slight, localized, mostly vertical subsidence signal of ~2.1 cm±0.9 cm over a time frame of two years at station QRRY (Grapenthin et al., 2013). This signal, however, was confined to

Estimated average surface deformation rates for the validation site were calculated based on the NED-DEM and the PRISM DEM shown in Figures 1.6 and 1.7, respectively. Surface deformation rates for this area should be close to zero and deviations from zero indicate biases of the applied method. Figure 1.6 suggests significant surface deformation with broad patterns of subsidence ranging from 5 cm to 25 cm. Coach Butte is characterized by a discernible 20 cm subsidence (blue) around its circumference. These effects, however, are an artifact produced by residual topographic signals in the differential interferometric phase; the topography surrounding Coach Butte was too steep to be represented by the NED-DEM's coarse resolution, and due to the time correlated spatial baselines in d-InSAR Subset 2, the residual topographic phase signal could not be separated from deformation-related signals. In contrast to Figure 1.6, Figure 1.7 was produced with the higher resolution and more current PRISM-DEM, and gives substantially different results. Areas of subsidence as high as 25 cm in Figure 1.6 are reduced to a range from 5 cm yr^{-1} to ~10 cm yr^{-1} in Figure 1.7 and are significantly closer to the expected value of zero. Probability density functions (PDFs) of topographic deformation rate estimates from NED-DEM and PRISM-DEM-based processing (Figure 1.8), further confirm these results. When based on the NED-DEM, the mean surface deformation rate (μ_{NED}), corresponding to an apparent

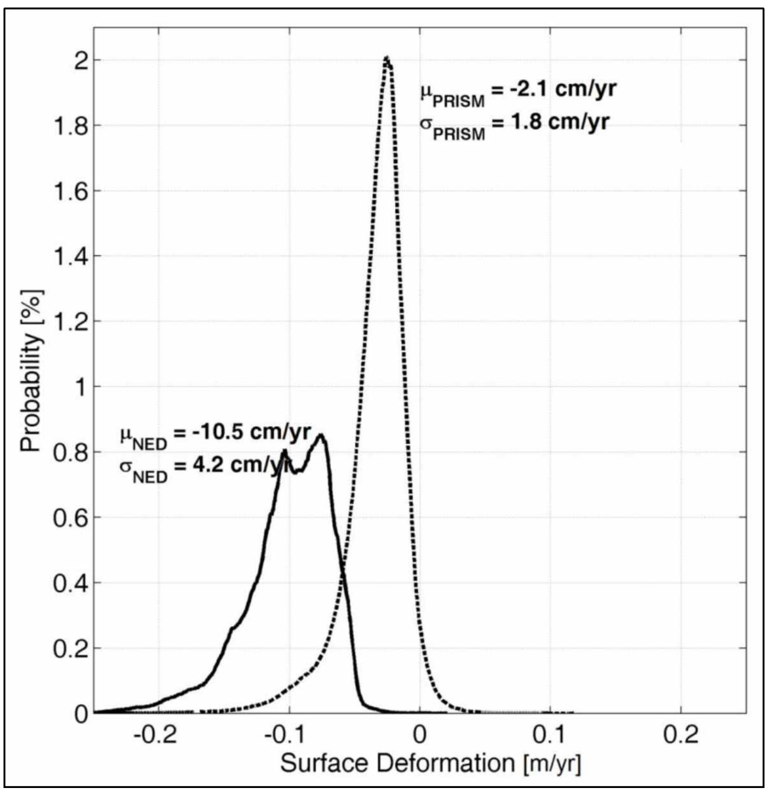

Figure 1.8: Probability density functions (PDFs) for surface deformation estimates based on NED-DEM (solid line) and PRISM-DEM (dashed line). Surface deformation estimates are given in cm yr^{-1} and were determined from post eruption interferogram pairs with an average surface deformation of 0 cm yr^{-1} (Subset 2 in Figure 1.5). Smaller standard deviation and mean values indicate the improved results obtained from PRISM based DEMs.

surface subsidence signal, was ~10.5 cm yr^{-1} in the validation area. A relatively large standard deviation (σ_{NED}) of 4.2 cm/year further indicates strong variability of these measures within the region. The mean surface deformation rate using the PRISM DEM (μ_{PRISM}), on the other hand, improved to ~2.1 cm/year, with a much reduced standard deviation (σ_{PRISM}) of 1.8 cm/year.

1.5.2.1 Comparison of InSAR-derived and GPS-derived deformation rates

An InSAR-derived deformation time series for GPS campaign station QRRY is shown in Figure 1.9 (area "A" and time series "A" in Figure 1.9). Deformation rates were averaged for the

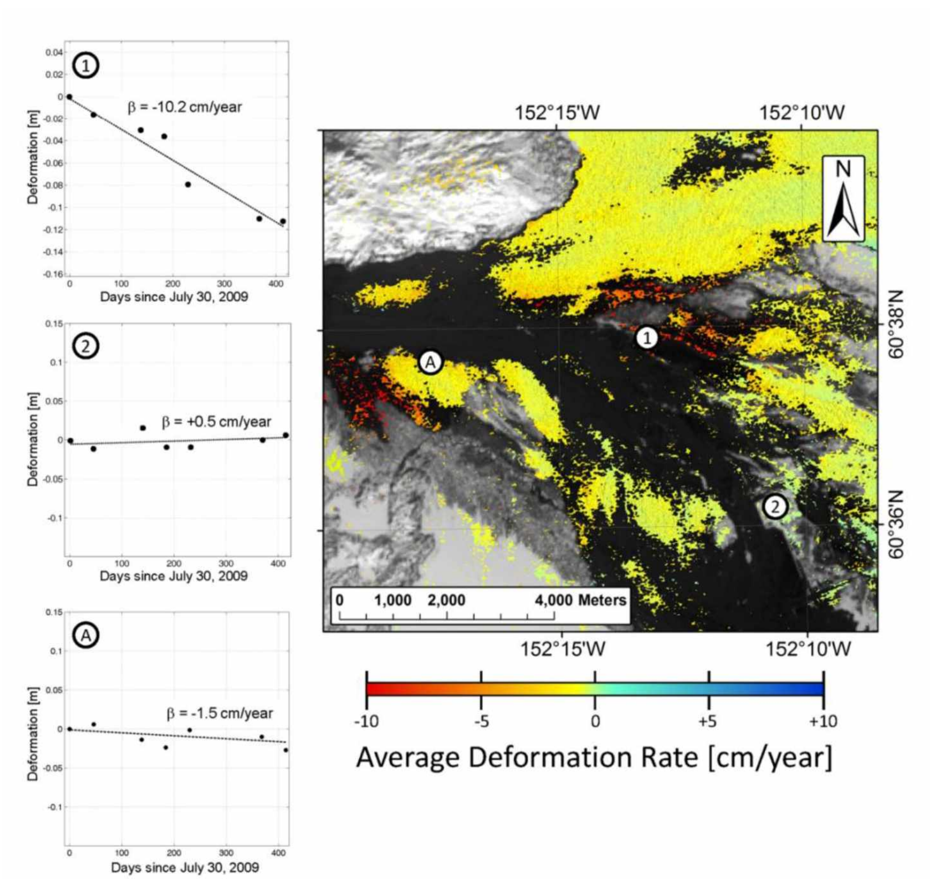

Figure 1.9: Post-lahar deformation in the eastern Drift River area. The deformation signals were detected by ten interferograms produced between 30 July 2009 and 18 December 2010, after lahars were emplaced 23 March 2009 through 4 April 2009. Black and gray areas were decorrelated in the interferograms; yellow, orange, and red areas represent contraction of lahar deposits from evaporation of interstitial water and settling. Deformation time series for three areas are plotted on the left. Area 1, which was clearly affected by lahars, shows the post-eruption contraction of lahar deposits, most likely caused by melting of an ice rich lahar that is buried underneath a later, less ice rich, deposit. Area 2, the location of the large petroleum storage tanks at the DROT, was protected by a surrounding dike, and was unaffected by the lahars. As expected, the time series plots for Area 2 show an absence of deformation. Area "A" is centered on the position of campaign GPS station QRRY, and is used to compare InSAR and GPS measurements.

30 InSAR points closest to station QRRY. Using InSAR, a linear surface deformation rate of ~1.5 cm yr^{-1} was determined, which matches the GPS-based deformation measurement (~1.1 cm yr^{-1}) within the accuracy of the two measurement types. The excellent fit of the PRISM-aided InSAR results to GPS and the vast improvement over the use of other DEMs indicates both the benefit of multi-sensor fusion and the high performance of InSAR-based deformation monitoring.

1.5.3 Geophysical results

Based on the PRISM-DEM and using the stack of ten post-eruption interferograms, the lahar deposits in the Drift River valley were analyzed for potential localized subsidence signals. In areas where thick layers of material were deposited, compaction and evaporation of interstitial water can lead to surface contraction sufficient for measurement with InSAR techniques. Figure 1.9 shows post-eruption deformation of the lahar surface for an area in the lower Drift River valley. An overlay of the deformation map (color) over a panchromatic optical light image from the Advanced Land Imager (ALI) aboard the Earth Observer-1 (EO-1) satellite is shown. Black regions in the ALI-image correspond to areas covered by the lahar deposits. Areas without deformation information were decorrelated to an extent that no surface subsidence signal could be derived. Sufficient coherence was present over extended areas however, and surface subsidence signals of 0.5 cm yr^{-1} to 20 cm yr^{-1} were obtained.

While extended areas of the lahar-covered region show only small subsidence rates of 5 cm yr^{-1} or less (indicated by shades of yellow and orange in Figure 1.9), some isolated areas were subject to enhanced subsidence. Up to 20 cm yr^{-1} subsidence was found on the western edge of the Drift River Delta and approximately 10 cm yr^{-1} are evident in an area northeast of the DROT (area "1" in Figure 1.9; the DROT is located at the bottom right in Figure 1.9). A deformation time series for the latter area is shown at the top left of Figure 1.9. Linear surface subsidence with a rate of 10.2 cm yr^{-1} is observed. As these deforming areas coincide with localized depressions, it is believed that thicker ice rich lahar deposits in this area that were emplaced on 23 March 2009 and later buried by deposits on 4 April (Waythomas et al., 2013). As the buried deposits melted out, larger, compaction-related subsidence signals were produced. Other notable features of Figure 1.9 includes a 10 cm yr^{-1} subsidence signal for a small area near the DROT runway as well as a 0 cm/year deformation of the DROT buildings and installations (area “2” in Figure 1.9). The deformation time series for the DROT buildings is shown at the bottom left of Figure 1.9. The close to 0 cm yr^{-1} deformation is a good match to the expectation of no significant deformation of this area within the observation time (400 days). This provides additional evidence of the precision and accuracy of the applied technique.

1.6 Fusion of multiple coherence maps for change detection

1.6.1 Method

Coherence is a measure of similarity between two spatial images. Besides being the basis for deriving accuracy measures of InSAR phase measurements, coherence analysis is also a powerful tool for change detection. Therefore, coherence maps were used in this study to map the extent of lahar deposits associated with the 2009 Redoubt Volcano eruption.

A loss of InSAR coherence is often referred to as decorrelation (Lu et al., 2010). Many sources of decorrelation can be identified, including (a) geometric decorrelation, caused by a difference in look angles between two acquisitions; (b) volume decorrelation, caused by penetration of the radar wave in the target surface; (c) Doppler centroid decorrelation, caused by differences in the Doppler centroids between acquisitions; (d) temporal terrain decorrelation, caused by physical changes in the target surface; and (e) processing induced decorrelation, which result from anomalies in the chosen algorithms (Hanssen, 2001). Normally, decorrelation is a limiting factor in InSAR analysis. However, low coherence has been previously used to for feature identification in glaciology applications (Li et al., 2001; Weydahl, 2001; Atwood et al., 2010), and analysis of lava flows (Zebker et al., 1996).

Due to the various influences that can contribute to signal decorrelation, the decorrelated regions in an individual InSAR coherence image are a combination of pixels that decorrelate permanently and pixels that show only sporadic decorrelation. Permanent decorrelation is due to physical changes of the surface as a consequence of cultivation, land cover and land use change, melting of ice sheets, as well as natural disasters such as earthquakes, volcanoes, and landslides. Sporadic decorrelation may be linked to short term changes of scattering conditions (e.g., seasonal effects, temporal increase of soil moisture, or freeze–thaw cycles) or unfavorable observation geometries such as long interferometric baselines. To robustly identify the extent of flow features from coherence analysis, we therefore propose a multi-image approach, where, from a stack of multiple coherence images, we identify those pixels that decorrelate permanently from those that only show only temporal coherence reduction.

To succeed in mapping flow feature extent, coherence images were calculated for the nine interferograms with a pre- and post-eruption temporal interval (Subset 1 in Figure 1.5). Based on a 5×5 estimation window and a coherence threshold of 0.25, pixels in every coherence image were classified as "correlated" or "decorrelated," and the resulting nine classification masks were stacked. Because a fundamental assumption in repeat pass InSAR is that surface scattering characteristics remain undisturbed (Lu, 2007), it follows that areas of lahar deposits will decorrelate permanently in the pre- and post-eruptive InSAR data. Therefore, a flow feature candidate mask was created from pixels that were decorrelated in all nine images. Combining information from a series of coherence images reduces the influence of temporarily decorrelated areas that are absent in areas of lahar deposition, and produces a significantly improved lahar mask. A further refinement of the flow feature candidate mask follows the approach of Atwood et al. (2010) to fill holes and remove small noise patches. In a final step, the outline of the flow feature mask is extracted and converted to a shape file to be used in mapping applications.

1.6.2 Geophysical results and validation of methods

Figure 1.10 shows the outline of the Drift River lahar as determined by the coherence-based method described above. The outline is shown in red and is overlain over a panchromatic optical light image from the EO-1/ALI instrument. This image was acquired on 4 April 2009 following the final explosive episode of the 2009 Redoubt eruption. Lahar deposits are, therefore, easily identifiable as black regions in the EO-1/ALI image, and can be used as a reference to validate the coherence-based approach.

A comparison of the coherence-derived lahar outline with the lahar deposits in the EO-1/ALI image shows remarkable correspondence with only minor differences in isolated areas. Major branches of the lahar fan were reproduced well by the mask, and more detailed signatures, like the flow of the lahar around the DROT, were clear and well preserved. These results confirm the usefulness of fusion of multiple SAR data for the analysis of volcanic eruptions.

Besides the high accuracy of the lahar mask as indicated by the results in Figure 1.10, it is important to point out that the coherence-based approach is effective in all weather, day or night conditions, both of which are among the main limitations of optical and thermal techniques. Adding SAR data to the list of routinely used remote sensing tools therefore, has great potential to improve the reliability and timeliness of remote sensing-based volcanic information, especially in cloudy conditions.

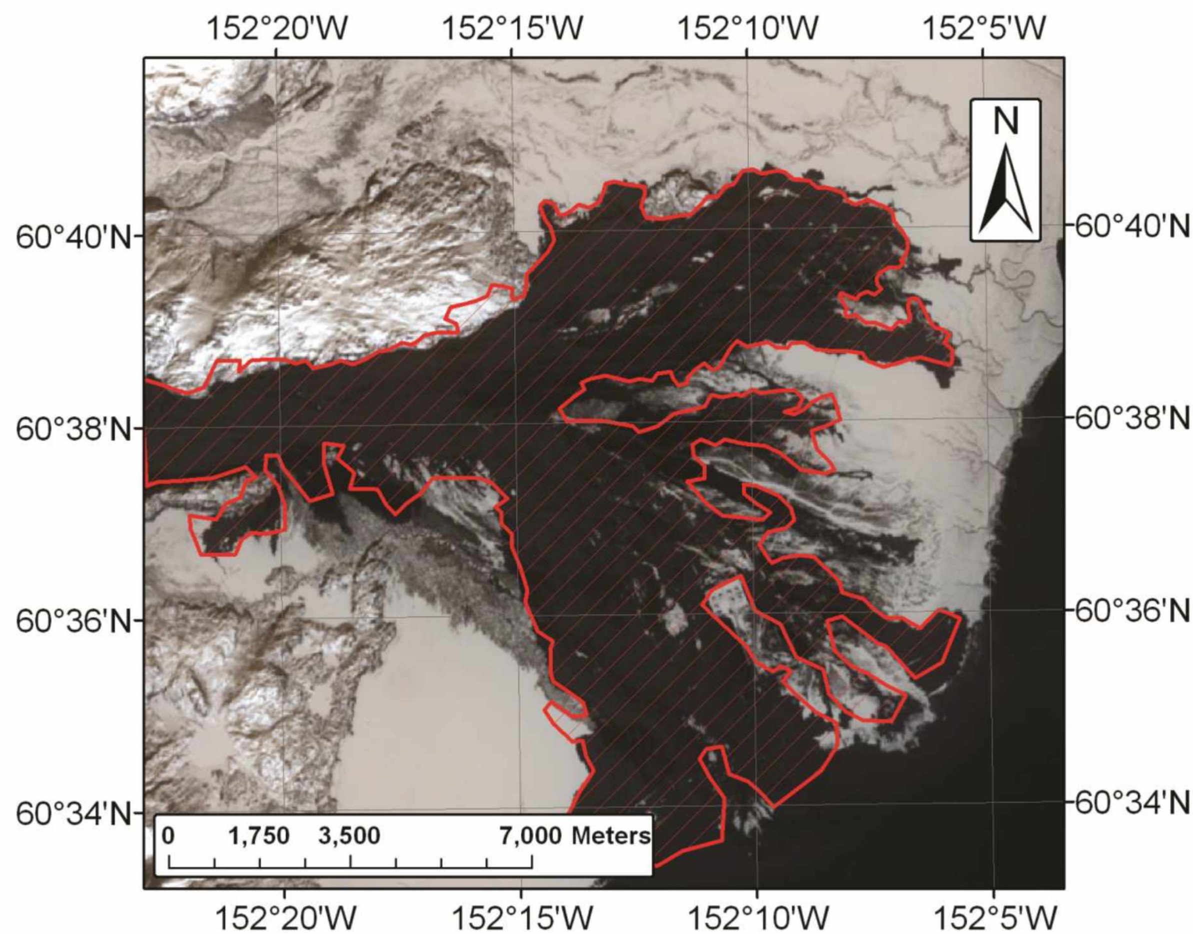

Figure 1.10: Lahar deposit on the Drift River Delta shown in a panchromatic EO-1/ALI image from 4 April 2009. Dark areas are lahar deposits. Red outline is the border of a flow-feature mask independently determined by automatically extracting decorrelation boundaries from a stack of nine interferogram pairs that span the lahar emplacement period of 23 March 2009 through 4 April 2009. Significant agreement between the visible lahar boundaries and areas of decorrelation confirm the potential usefulness of multiple SAR datasets for the analysis of volcanic deposition.

1.7 Conclusions

The results of this paper demonstrate how products from multiple sensors can be used to obtain measurements and details of volcanic deformation with greater accuracy and higher resolution than is achievable with a single sensor. Three different approaches for multi-sensor data analysis were tested for their performance.

In the first approach, optical PRISM data were used to develop high-resolution DEMs of the Redoubt Volcano and Drift River valley. These multi-temporal DEMs were fused, and used to examine deformation caused by lahar deposits and scour, and to make an estimate of the 2009

Redoubt lava dome. In examples it was shown that multi-temporal PRISM DEM information can be used to detect meter-scale changes in surface topography on volcanic edifice.

A second approach fuses PRISM-DEMs with microwave PALSAR data to demonstrate the utility of multi-sensor differential interferograms and produce cm-accurate deformation maps of lahars in the Drift River valley. Here, it was specifically demonstrated that accurate and up-to-date DEM information is indispensable if precision surface deformation information is to be extracted shortly after an eruption and from a low number of datasets.

Finally, an algorithm for mapping outlines of lahar deposits from multi-temporal coherence maps was presented. To the knowledge of the authors, the developed algorithm is unique in that it takes full advantage of all available coherence information in several post eruptive InSAR pairs to reduce noise and false alarms in automatic lahar mask creation. In an application of this technique to Redoubt volcano, accurate maps of lahar deposits were produced that conformed well to the extent of lahar deposits imaged by the EO-1/ALI satellite on 4 April 2009.

These results were primarily obtained using data from the PRISM and PALSAR instruments aboard the ALOS satellite. Although power anomalies forced the ALOS mission to terminate on 12 May 2011(JAXA, 2011), the advantages of multi-sensor data fusion to improve elevation change detection are well demonstrated. This is of particular importance, given that the number and capacity of earth observing satellites and sensors can only be expected to grow in the future. Over the next 15 years, the Committee on Earth Observation Satellites (CEOS) reports that its member agencies are operating or plan to operate 260 earth observing satellites with more than 400 different instruments (CEOS, 2011). This increase in data will present numerous opportunities to extend these results into other disciplines, and to increase the accuracy and precision of satellite remote sensing in volcanic applications.

1.8 Acknowledgments

Funding for this work was provided by the Alaska Satellite Facility at the University of Alaska Fairbanks Geophysical Institute. Additional support was provided by EPSCoR NSF award #EPS-0701898 and the State of Alaska. Pre-processing of PALSAR and PRISM data were performed by the Alaska Satellite Facility. Interferometric PALSAR data include material © JAXA, METI, 2011. PRISM-DEMs and orthorectified PRISM data include material © JAXA, 2011. NED data and EO-1/ALI images were provided courtesy of the US Geological Survey, Earth Resources Observation and Science (EROS) Center, Sioux Falls, SD. Map of Drift River vicinity provided with permission from TOPO! © 2011 National Geographic. The authors gratefully acknowledge Mike Poland and an anonymous reviewer for comments and suggestions that greatly improved the manuscript.

1.9 References

Amelung, F., Jonssón, S.Â., Zebker, H., and Segall, P., 2000, Widespread uplift and 'trapdoor' faulting on Galápagos volcanoes observed with radar interferometry: Nature, v. 407, p. 993-996.

Atwood, D.K., Meyer, F., and Arendt, A., 2010, Using L-band SAR coherence to delineate glacier extent: Canadian Journal of Remote Sensing, v. 36, p. S186-S195, doi: 10.5589/m10-014.

Berardino, P., Fornaro, G., Lanari, R., and Sansosti, E., 2002, A new algorithm for surface deformation monitoring based on small baseline differential SAR interferograms: IEEE Transactions on Geoscience and Remote Sensing, v. 40, p. 2375-2383, doi: 10.1109/TGRS.2002.803792.

Bull, K., and Buurman, H., 2013a, An overview of the 2009 eruption of Redoubt Volcano, Alaska: Journal of Volcanology and Geothermal Research: Special Issue on the 2009 Redoubt Eruption, v. 259, p. 2-15, doi: 10.1016/j.jvolgeores.2012.06.024.

Bull, K.F., 2009, Redoubt Volcano: 2009 Eruption Overview: AGU Fall Meeting, Abstract V51F-01, v. 1, p. 01.

Bull, K.F., and Buurman, H., 2013b, An overview of the 2009 eruption of Redoubt Volcano, Alaska: Journal of Volcanology and Geothermal Research, v. 259, p. 2-15, doi: 10.1016/j.jvolgeores.2012.06.024.

CEOS, 2011, "CEOS EO handbook - earth observation satellite capabilities and plans", Committee on Earth Observing Satellites, http://www.eohandbook.com/eohb2011/earthobservation.htm, accessed 18 May 2012.

Chlieh, M., De Chabalier, J., Ruegg, J., Armijo, R., Dmowska, R., Campos, J., and Feigl, K., 2004, Crustal deformation and fault slip during the seismic cycle in the North Chile subduction zone, from GPS and InSAR observations: Geophysical Journal International, v. 158, p. 695-711, doi: 10.1111/j.1365-246X.2004.02326.x.

CIS, 2011, "Alaska community database community information summaries (CIS)", Alaska Department of Commerce, Community, and Economic Development, http://www.commerce.state.ak.us/dca/commdb/CF_CIS.htm, accessed 20 May 2011.

Diefenbach, A., Bull, K.F., Wessels, R.L., and McGimsey, R., 2013, Photogrammetric monitoring of lava dome growth during the 2009 eruption of Redoubt Volcano: Journal of Volcanology and Geothermal Research, v. 259, p. 308-316, doi: 10.1016/j.jvolgeores.2011.12.009.

Fielding, E.J., Blom, R.G., and Goldstein, R.M., 1998, Rapid subsidence over oil fields measured by SAR: Geophysical Research Letters, v. 25, p. 3215-3218, doi: 10.1029/98GL52260.

Gesch, D., Evans, G., Mauck, J., Hutchinson, J., and Carswell, W.J., Jr., 2009, The National Map - Elevation: USGS Fact Sheet 2009-3053, US Geological Survey, 4 pp., http://pubs.usgs.gov/fs/2009/3053/.

Gong, P., 1994, Integrated analysis of spatial data from multiple sources: an overview: Canadian Journal of Remote Sensing, v. 20, p. 349-359, doi: 10.1080/07038992.1994.10874578.

Grapenthin, R., Freymueller, J.T., and Kaufman, A.M., 2013, Geodetic observations during the 2009 eruption of Redoubt Volcano, Alaska: Journal of Volcanology and Geothermal Research, v. 259, p. 115-132, doi: 10.1016/j.jvolgeores.2012.04.021.

Hanssen, R.F., 2001, Radar interferometry: data interpretation and error analysis: Dordrecht, The Netherlands, Kluwer Academic Publishers, 308 pp.

Hoffmann, J., Zebker, H.A., Galloway, D.L., and Amelung, F., 2001, Seasonal subsidence and rebound in Las Vegas Valley, Nevada, observed by synthetic aperture radar interferometry: Water Resources Research, v. 37, p. 1551-1566, doi: 10.1029/2000WR900404.

Honikel, M., 1998, Improvement of InSAR DEM accuracy using data and sensor fusion, *in* Proceedings, International Geoscience and Remote Sensing Symposium (IGARSS), vol. 5, Seattle, Washington, 6-10 Jul 1998, pp. 2348-2350.

Hooper, A., Zebker, H., Segall, P., and Kampes, B., 2004, A new method for measuring deformation on volcanoes and other natural terrains using InSAR persistent scatterers: Geophysical Research Letters, v. 31, p. L23611, doi: 10.1029/2004GL021737.

JAXA, 2011, "Japan Aerospace Exploration Agency press release dated 12 May 2011: DAICHI (ALOS) operation completion", http://www.jaxa.jp/press/2011/05/20110512_daichi_e.html, accessed 7 May 2012.

Lanari, R., Mora, O., Manunta, M., Mallorquí, J.J., Berardino, P., and Sansosti, E., 2004, A small-baseline approach for investigating deformations on full-resolution differential SAR interferograms: Geoscience and Remote Sensing, IEEE Transactions on, v. 42, p. 1377-1386, doi: 10.1109/TGRS.2004.828196.

Lee, C.W., Lu, Z., Jung, H.S., Won, J.S., and Dzurisin, D., 2010, Surface deformation of Augustine Volcano, 1992–2005, from multiple-interferogram processing using a refined small baseline subset (SBAS) interferometric synthetic aperture radar (InSAR) approach, *in* Power, J.A., Coombs, M.L., and Freymueller, J.T., eds., The 2006 eruption of Augustine Volcano, Alaska: U.S. Geological Survey Professional Paper 1769, p. 453-465.

Li, Z., Guo, H., Li, X., and Wang, C., 2001, SAR interferometry coherence analysis for snow mapping, *in* Proceedings, International Geoscience and Remote Sensing Symposium (IGARSS), vol. 6, Sydney, NSW, Australia, 9-13 July 2001, pp. 2905-2907.

Lu, Z., 2007, InSAR imaging of volcanic deformation over cloud-prone areas - Aleutian Islands: Photogrammetric Engineering & Remote Sensing, v. 73, p. 245-257, doi: 10.14358/PERS.73.3.245.

Lu, Z., Dzurisn, D., Jung, H.-S., Zhang, J., and Zhang, Y., 2010, Radar image and data fusion for natural hazards characterisation: International Journal of Image and Data Fusion, v. 1, p. 217-242, doi: 10.1080/19479832.2010.499219.

Lu, Z., Fielding, E., Patrick, M.R., and Trautwein, C.M., 2003, Estimating lava volume by precision combination of multiple baseline spaceborne and airborne interferometric synthetic aperture radar: the 1997 eruption of Okmok Volcano, Alaska: IEEE Transactions on Geoscience and Remote Sensing, v. 41, p. 1428-1436, doi: 10.1109/TGRS.2003.811553

Lu, Z., Mann, D., Freymueller, J.T., and Meyer, D.J., 2000, Synthetic aperture radar interferometry of Okmok Volcano, Alaska: radar observations: Journal of Geophysical Research, v. 105, doi: 10.1029/2000JB900034.

Lu, Z., Masterlark, T., and Dzurisin, D., 2005, Interferometric synthetic aperture radar study of Okmok volcano, Alaska, 1992:2003: Magma supply dynamics and post-emplacement lava flow deformation: Journal of Geophysical Research, v. 110, p. B02403, doi: 10.1029/2004JB003148.

Lundgren, P., Usai, S., Sansosti, E., Lanari, R., Tesauro, M., Fornaro, G., and Berardino, P., 2001, Modeling surface deformation observed with synthetic aperture radar interferometry at Campi Flegrei caldera: Journal of Geophysical Research, v. 106, p. 19355-19366, doi: 10.1029/2001JB000194.

Meyer, F., Gernhardt, S., and Adam, N., 2007, Long-term and seasonal subsidence rates in urban areas from persistent scatterer interferometry, *in* Proceedings, Urban Remote Sensing Joint Event, vol. 7, Paris, France, 2007, pp. 1-6, doi: 10.1109/URS.2007.371883.

Miller, T.P., McGimsey, R.G., Richter, D.H., Riehle, J.R., Nye, C.J., Yount, M.E., and Dumoulin, J.A., 1998, Catalog of the historically active volcanoes of Alaska: U.S. Geological Survey Open-File Report 98-582, US Department of the Interior, US Geological Survey, 104 pp.

Pohl, C., and Van Genderan, J.L., 1998, Multisensor image fusion in remote sensing: concepts, methods and applications: International Journal of Remote Sensing, v. 19, p. 823-854, doi: 10.1080/014311698215748.

Riehle, J.R., 1985, A reconnaissance of the major Holocene tephra deposits in the upper Cook Inlet region, Alaska: Journal of Volcanology and Geothermal Research, v. 26, p. 37-74, doi: 10.1016/0377-0273(85)90046-0.

Rogers, R.H., and Wood, L., 1990, The history and status of merging multiple sensor data: an overview, presented at the ACSM-ASPRS Annual Convention, Technical Papers 1990, Image Processing and Remote Sensing, vol. 4, Denver, Colorado, pp. 352-360.

Rosen, P.A., Hensley, S., Joughin, I.R., Li, F.K., Madsen, S.N., Rodriguez, E., and Goldstein, R.M., 2000, Synthetic aperture radar interferometry: Proceedings of the IEEE, v. 88, p. 333-382, doi: 10.1109/5.838084.

Rosenqvist, A., Shimada, M., Ito, N., and Watanabe, M., 2007, ALOS PALSAR: A pathfinder mission for global-scale monitoring of the environment: IEEE Transactions on Geoscience and Remote Sensing, v. 45, p. 3307-3316, doi: 10.1109/TGRS.2007.901027.

Ryder, I., Parsons, B., Wright, T.J., and Funning, G.J., 2007, Post seismic motion following the 1997 Manyi (Tibet) earthquake: InSAR observations and modelling: Geophysical Journal International, v. 169, p. 1009-1027, doi: 10.1111/j.1365-246X.2006.03312.x.

Samsonov, S., 2010, Topographic correction for ALOS PALSAR interferometry: IEEE Transactions on Geoscience and Remote Sensing, v. 48, p. 3020-3027, doi: 10.1109/TGRS.2010.2043739

Schaefer, J.R.G., *ed.*, 2012, The 2009 Eruption of Redoubt Volcano, Alaska: Fairbanks, Alaska, Alaska Division of Geological & Geophysical Surveys, Report of Investigations 2011-5, 45 p.

Simone, G., Farina, A., Morabito, F., Serpico, S.B., and Bruzzone, L., 2002, Image fusion techniques for remote sensing applications: Information Fusion, v. 3, p. 3-15, doi: 10.1016/S1566-2535(01)00056-2.

Singhroy, V., Couture, R., Alasset, P.J., and Poncos, V., 2007, InSAR monitoring of landslides on permafrost terrain in Canada, *in* Proceedings, International Geoscience and Remote Sensing Symposium (IGARSS), Barcelona, Spain, pp. 2451-2454, doi: 10.1109/IGARSS.2007.4423338

Stramondo, S., Bozzano, F., Marra, F., Wegmuller, U., Cinti, F., Moro, M., and Saroli, M., 2008, Subsidence induced by urbanisation in the city of Rome detected by advanced InSAR technique and geotechnical investigations: Remote Sensing of Environment, v. 112, p. 3160-3172, doi: 10.1016/j.rse.2008.03.008.

Tadono, T., Shimada, M., Watanabe, M., Hashimto, T., and Iwata, T., 2004, Calibration and validation of PRISM onboard ALOS.: International Archives of the photgrammetry, remote sensing, and spatial Information Sciences, v. 35, p. 13-18.

Takaku, J., and Tadono, T., 2009, PRISM on-orbit geometric calibration and DSM performance: IEEE Transactions on Geoscience and Remote Sensing, v. 47, p. 4060-4074, doi: 10.1109/TGRS.2009.2021649.

Till, A.B., Yount, M.E., and Bevier, M.L., 1994, The geologic history of Redoubt Volcano, Alaska: Journal of Volcanology and Geothermal Research, v. 62, p. 11-30, doi: 10.1016/0377-0273(94)90026-4.

Toutin, T., 2004, Review article: Geometric processing of remote sensing images: models, algorithms and methods: International Journal of Remote Sensing, v. 25, p. 1893-1924, doi: 10.1080/0143116031000101611.

Trabant, D., and Hawkins, D.B., 1997, Glacier ice-volume modeling and glacier volumes on Redoubt Volcano, Alaska: U.S.Geological Survey water-resources investigation report 97-4187, 29 pp., (US).

Tuck, B.H., Huskey, L., and Talbot, L., 1992, The economic consequences of the 1989-90 Mt. Redoubt eruptions, Institute of Social and Economic Research, University of Alaska Anchorage, Unpublished report for the U.S. Geological Survey and the Alaska Volcano Observatory, Anchorage, Alaska, 42 pp.

USGS, 2003, Landsat: A global land-observing program, US Geological Survey Fact Sheet 023-03, 4 pp., https://pubs.usgs.gov/fs/2003/0023/.

van Zyl, J.J., 2001, The Shuttle Radar Topography Mission (SRTM): a breakthrough in remote sensing of topography: Acta Astronautica, v. 48, p. 559-565, doi: 10.1016/S0094-5765(01)00020-0.

Waythomas, C.F., Pierson, T.C., Major, J.J., and Scott, W.E., 2013, Voluminous ice-rich and water-rich lahars generated during the 2009 eruption of Redoubt Volcano, Alaska: Journal of Volcanology and Geothermal Research, v. 259, p. 389-413, doi: 10.1016/j.jvolgeores.2012.05.012.

Weydahl, D.J., 2001, Analysis of ERS tandem SAR coherence from glaciers, valleys, and fjord ice on Svalbard: IEEE Transactions on Geoscience and Remote Sensing, v. 39, p. 2029-2039, doi: 10.1109/36.951093

Wilson, C.R., and Forbes, R.B., 1969, Infrasonic Waves from Alaskan Volcanic Eruptions: J. Geophys. Res., v. 74, p. 4511-4522, doi: 10.1029/JC074i018p04511.

Wolfram|Alpha, 2011, "Wolfram|Alpha computational knowledge engine", Wolfram Alpha, LLC, http://www.wolframalpha.com/input/?i=volume+of+a+prolate+spheroid, accessed 12 December 2010.

Wright, T.J., Lu, Z., and Wicks, C., 2003, Source model for the M_w 6.7, 23 October 2002, Nenana Mountain Earthquake (Alaska) from InSAR: Geophysical Reserve Letters, v. 30, p. 12-1–12-4, doi: 10.1029/2003GL018014.

Zebker, H.A., Rosen, P., Hensley, S., and Mouginis-Mark, P.J., 1996, Analysis of active lava flows on Kilauea volcano, Hawaii, using SIR-C radar correlation measurements: Geology, v. 24, p. 495-498, doi: 10.1130/0091-7613(1996)024<0495:AOALFO>2.3.CO;2.

Chapter 2

Pyroclastic flow deposits and InSAR: analysis of long-term subsidence at Augustine Volcano, Alaska[1]

2.1 Abstract

Deformation of pyroclastic flow deposits begins almost immediately after emplacement, and continues thereafter for months or years. This study analyzes the extent, volume, thickness, and variability in pyroclastic flow deposits on Augustine Volcano from measuring their deformation rates with interferometric synthetic aperture radar. To conduct this analysis, we obtained 48 synthetic aperture radar images of Augustine Volcano acquired between 1992 and 2010, spanning its most recent eruption in 2006. The data were processed using differential interferometric synthetic aperture radar time-series analysis to measure the thickness of the Augustine pyroclastic flow deposits, as well as their surface deformation behavior. Because much of the 2006 pyroclastic flow deposits overlie those from the previous eruption in 1986, geophysical models were derived to decompose deformation contributions from the 1986 deposits underlying the measured 2006 deposits. To accomplish this, we introduce an inversion approach to estimate geophysical parameters for both 1986 and 2006 pyroclastic flow deposits. Our analyses estimate the expanded volume of pyroclastic flow material deposited during the 2006 eruption to be 3.3×10^{7} m^3 ± 0.11×10^{7} m^3, and that pyroclastic flow deposits in the northeastern part of Augustine Island reached a maximum thickness of ~31 m with a mean of ~5 m. Similarly, we estimate the expanded volume of pyroclastic flow deposits from the 1986 eruption at 4.6×10^{7} m^3 ± 0.62×10^{7} m^3, with a maximum thickness of ~31 m, and a mean of ~7 m.

---

[1] Previously published as McAlpin, D., Meyer, F., Gong, W., Beget, J., and Webley, P., 2017, Pyroclastic flow deposits and InSAR: analysis of long-term subsidence at Augustine Volcano, Alaska: Remote Sensing, v. 9, p. 4, doi: 10.3390/rs9010004.

2.2 Introduction

Interferometric synthetic aperture radar (InSAR) is well established as a means for identifying terrain deformation associated with volcanic activity (Gabriel et al., 1989; Massonnet and Feigl, 1998; Mouginis-Mark and Domergue-Schmidt, 2000; Rosen et al., 2000; Masterlark and Lu, 2004). InSAR processing can be used to measure changes in the surface deformation with centimeter to sub-centimeter accuracy at regional scales as terrains inflate and deflate with subsurface magma intrusion and extrusion (Rosen et al., 1996; Zebker et al., 2000), and also at local scales as post-eruptive materials subside through compaction, degassing, and other mechanisms (Sheridan and Ragan, 1975; Riehle et al., 1995).

All eruptive materials are subject to localized deformation, with each material having its own particular characteristics Common examples of these characteristics are observed in lavas and pyroclastic flow deposits. Lavas are flows of magma that have erupted at the Earth's surface effusive volcanic activity (Cas and Wright, 1987). Pyroclastic flows are produced by more violent explosive activity or gravitational dome collapse (Williams and McBirney, 1979). They can be described, generally, as hot, gravity controlled, rapidly moving flows of high particle-concentration ash and gas, and, in some instances, may be partly fluidized (Cas and Wright, 1987). They are the high-solids end member of the more broadly defined pyroclastic density currents, which include a mixture of both pyroclastic flows and a more dilute, highly turbulent end member called a pyroclastic surge (Vallance et al., 2010).

Most eruptive products, especially lava, pyroclastic flow deposits, and pyroclastic surge deposits, are not static once emplaced. Vertical displacement continues within each (Briole et al., 1997; Stevens et al., 2001; Lu et al., 2005), albeit at different rates based on individual rheology and susceptibility to erosion and compaction. Vertical displacement of this nature can be accurately measured with InSAR, which in turn provides clues to the materials' thermo-mechanical. This paper is concerned with pyroclastic flow deposits (PFDs). But pyroclastic flow processes are highly complex; consequently, no single description of their deposits satisfies all conditions. As Williams and McBirney (1979) observed, "many classifications of pyroclastic flows have been proposed, but none is without its deficiencies", and Schmincke (2004) added, "a well-documented general discussion of the many terms and genetic concepts for the origin of pyroclastic flows and their deposits covering the last 100 years would require a long chapter on its own." Over decades of research, pyroclastic flows have been variously described as *nuée ardentes*, glowing avalanches, incandescent tuff flows, ash flows, sand flows, and block-and-ash flows, and related deposits as PFDs, ignimbrites, ash-flow tuffs, and welded tuffs, to name a few. Regardless of nomenclature, however, the underlying commonality is that each represents an unconsolidated deposit laid down at high temperature (Williams and McBirney, 1979).

In this paper, pyroclastic flow deposits (PFDs) describe deposits of unconsolidated rock and ash from the high-solids end member of a pyroclastic density current, regardless of its origin, mechanism of transport, or particle concentration (Vallance et al., 2010). More specifically, we examine the thickness and long-term deformation of PFDs at Augustine Volcano, Alaska, and present methods that can be used to determine those parameters from InSAR measurements acquired between 1992 and 2010, and to model the thickness of the historical 1986 PFD that underlies the observable 2006 deposits.

Augustine Volcano (Figure 2.1) was selected for this work because its eruption history is both frequent and relatively recent. Moreover, its last two eruptions, in 1986 and 2006, resulted in significant PFDs on its north flank, as shown in Figure 2.2a,b. This layered deposition requires observation of deformation behavior in two overlying generations of PFDs. Although this is a condition commonly found at active volcanoes, it complicates measurements of surface deformation, because any such measurement will contain the combined effect of a number of

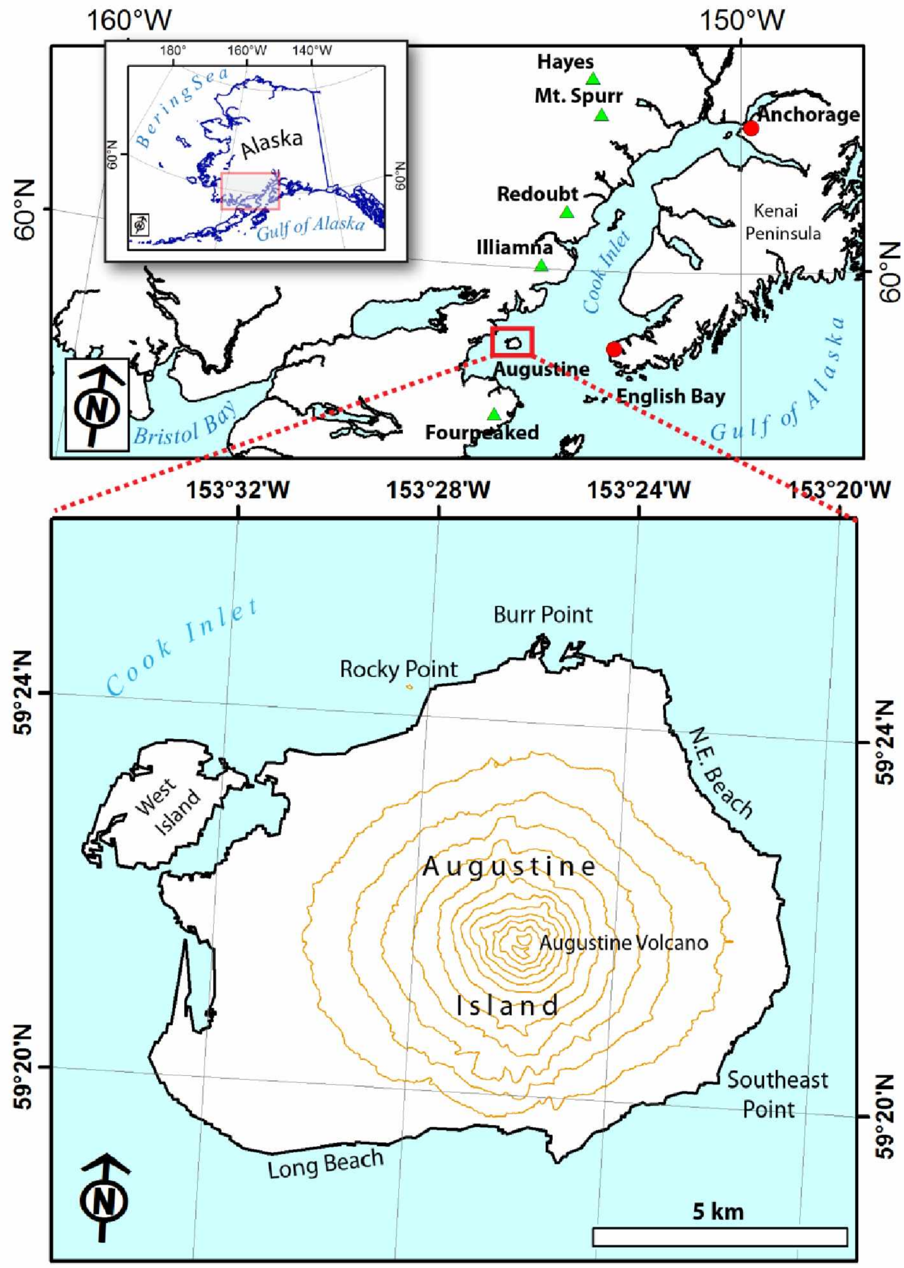

Figure 2.1 Augustine Island (59°21.6'N, 153°25.9'W) and the Cook Inlet vicinity of south-central Alaska. Volcanoes described in the text are marked by green triangles; populated places by red circles. Contour line interval is 100 m.

superimposed PFDs. Analyzing one individual deposit, therefore, is not possible from direct measurements alone. To solve this issue, we use a combination of long-term InSAR observations and basic geophysical models to decompose contributions from several generations of overlying PFDs and derive specific geophysical information. At Augustine Volcano, SAR data suitable for interferometry are available from June 1992 to October 2005, from March 2006 to April 2007, and from July 2007 to October 2010, spanning its most recent eruption in 2006. By using these data in combination with geophysical models, we were able to project deformation rates back to pre-SAR periods from 1986 to 1992 and estimate original thickness and long-term subsidence rates for PFDs related to Augustine Volcano's two most recent eruptions in 1986 and 2006.

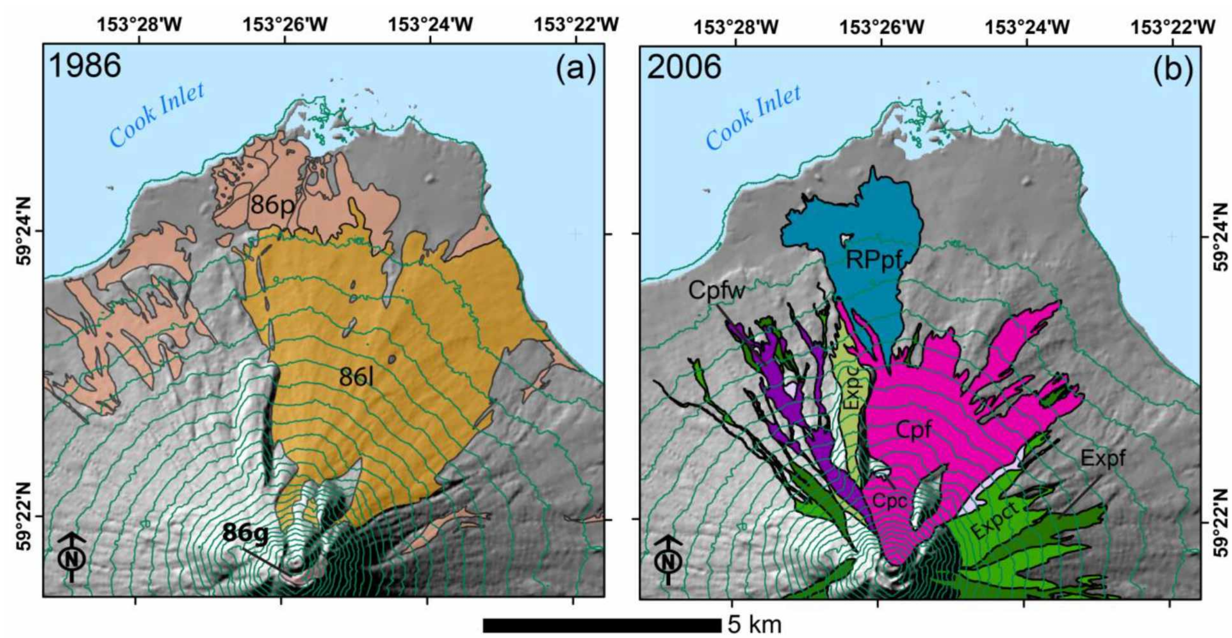

Figure 2.2 The north flank of Augustine Island with pertinent deposits from the 1986 and 2006 eruptions. From 1986 (**a**): 86l—Lithic PFD; 86g—Dome agglutinate and proximal fall; 86p—Deposits from pumacious pyroclastic flows, mixed flows, and lahars (modified from Waitt et al. (2009)). From 2006 (**b**): Cpf—Continuous phase PFDs; Cpc—Continuous phase pyroclastic current deposits; Cpfw—Windy PFD; RPpf—Rocky Point PFD; Expc—Explosive-phase pyroclastic current deposit; Expf—Explosive-phase PFD; Expct—Thin explosive-phase PFDs (modified from Coombs et al. (2010b)). Contour lines at 50 m.

Consistent with previous observations of PFDs (Rowley et al., 1981; Masterlark et al., 2006), we found that PFDs from the 2006 eruption rapidly subsided for an initial post-emplacement period, before slowing to a more persistent and linear long-term rate. For Augustine, we found that the initial post-emplacement period was about six months and the long-term subsidence rate was proportional to the deposits' thickness, which allows for the assessment of deposit thickness from measured subsidence rates and vice versa.

2.3 Augustine Volcano

Augustine Volcano is located in Cook Inlet, Alaska, approximately 285 km southwest of Anchorage (Figure 2.1). It completely occupies its namesake Augustine Island, an 8 km × 11 km, uninhabited island of pyroclastic debris surrounding a central dome complex. It is the youngest and most active of five historically active volcanoes in the Cook Inlet area, which, besides Augustine, include Mt. Spurr, Redoubt Volcano, Iliamna Volcano (Riehle, 1985), and most recently Fourpeaked Mountain, which experienced a minor eruption in 2006 (Zielinki, 2006; Neal et al., 2008).

Since its discovery by James Cook in 1778 (Kienle and Shaw, 1979), Augustine Volcano has had major eruptions in 1883, 1908, 1935, 1964, 1976, 1986, and 2006 (Power and Lalla, 2010). Its 1883 eruption, the first to be contemporaneously documented, is also considered its most violent (Yount et al., 1987; Miller et al., 1998). It began on 6 October 1883, when an edifice collapse extended the north coastline of the island by 2 km (Waitt and Begét, 2009), and a resulting debris avalanche, which extended another 2.5 km into Cook Inlet (Siebert et al., 1989), caused a tsunami in the range of 6 m to 9 m at the English Bay settlement, 85 km to the west (Davidson, 1884; Begét and Kowalik, 2006), Figure 2.1 (English Bay was renamed *Nanwalek* on 12 July 2007 by the USGS Board of Geographic Names (GNIS, 2007); the name English Bay is used here for continuity with previous work). Contemporaneous accounts describe the English Bay tsunamis destroying fishing boats and inundating houses (Davidson, 1884), and accompanying ash falls were sufficient to bury Aleut *barabaras,* the communal houses of the Aleuts and some Inuit bands of native Alaskans (from 1898 field notes of J.A. Spurr, quoted by Kienle et al., 1987).

Over the next 123 years, through 2006, Augustine erupted on least six occasions, with significant pyroclastic flows occurring in 1964, 1976, 1986, and 2006. Each of these eruptions were similar in nature and composition, beginning with an initial explosive phase (VEI ~3), followed by a period of decreasing intensity, and finally, an effusive, dome building phase (Cervelli et al., 2006; Power et al., 2006; Coombs et al., 2010a). Although Augustine has had four eruptions in the past 50 years, this paper examines the two most recent eruptions in 1986 and 2006. This was a practical limitation, because civilian Earth-Observing radar imaging satellites suitable for interferometry, were not available before the launch of ERS-1 (Curlander and McDonough, 1991). In any case, by the time SAR satellite data were available, much of Augustine's pre-1986 eruptive products had been overlain by its subsequent eruption.

2.3.1 The 1986 eruption and its PFDs

The 1986 eruption began 27 March and continued with three main episodes, from 27 March–2 April; from 23–28 April; and 22 August–1 September (Yount et al., 1987). A large andesitic dome resulting from the eruption engulfed a dome emplaced in 1976, which had, in turn, incorporated part of a 1935 dome and all of the 1883 dome (Waitt and Begét, 2009). In the first and most explosive episode of the eruption, a nearly continuous ash plume reached altitudes of 4.6 km above sea level (ASL), while explosions generated episodic ash clouds up to 12.3 km ASL. Hundreds of pyroclastic flows extended down the north and northeast flanks, with the largest of these reaching Cook Inlet, to the west and east of Burr Point, some 5 km from the summit vent (Yount et al., 1987). Early in the eruption, these flows were rich in pumice. In latter stages, dome collapse events created more lithic pyroclastic flows of dome rock (porphyritic andesite), leaving a broad fan on the north flank, downslope from the 1986 dome (Waitt and Begét, 2009) (Figure 2.2a). Pyroclastic flows continued during the late April and August episodes of the eruption, but these were greatly reduced in number and on a smaller scale. Lava was eventually produced from the summit vent, flowing down a gully on the north flank until formation of a dome in late August (Yount et al., 1987).

2.3.2 The 2006 eruption and its PFDs

At the conclusion of its 1986 eruption, Augustine was quiescent for nearly 20 years, until a 6-month period of pre-eruption seismicity began in the summer of 2005 (Coombs et al., 2010a). On 11 January 2006, the volcano erupted in a 17-day series of explosions that would be the first of three distinct eruption phases. This first phase, termed the "Explosive Phase," produced ash plumes up to 14 km ASL, along with lava flows and a number of pyroclastic flows on the north flank. These included the largest flow of the Explosive Phase, which, at 4.8 km in length, was designated by Coombs et al., (2010a) as the Rocky Point Pyroclastic Flow (see RPpf deposit in Figure 2.2b). On 28 January, the volcano's Explosive Phase ended, and a 13-day period of essentially uninterrupted activity began. This was the "Continuous Phase," so named to separate it from the discrete explosions of the previous Explosive Phase. The Continuous Phase was characterized by nearly constant, rapid effusion, numerous pyroclastic flows on the north flank (Vallance et al., 2010), and episodic seismic activity. Especially during the early stage of this phase, pyroclastic flows were common, and their deposits would eventually cover an area of 4.9 km^2 and extend from the summit vent more than 3.8 km down the north flank.

The 2006 eruption concluded with a final, 13-day Effusive Phase from 3–16 March. This phase followed a 21-day hiatus in activity, and resulted in a larger summit dome, increased lava flows on the north flank, and significant block and ash flows. The eruption concluded on 16

March, when no further juvenile material was observed (Coombs et al., 2010a).

A comparison of eruption products from 2006 indicates broad compositional overlap with those from 1986. Silica variation diagrams of major element, whole rock compositions of 70 samples from the 2006 eruption (Larsen et al., 2010), overlaid with 60 whole-rock samples from the 1986 eruption (Gardner, 2016) are presented in Figure 2.3. These compositional similarities imply that the 1986 and the 2006 PFDs have similar thermo-mechanical properties, which will cause them to deform in a similar fashion as they cool.

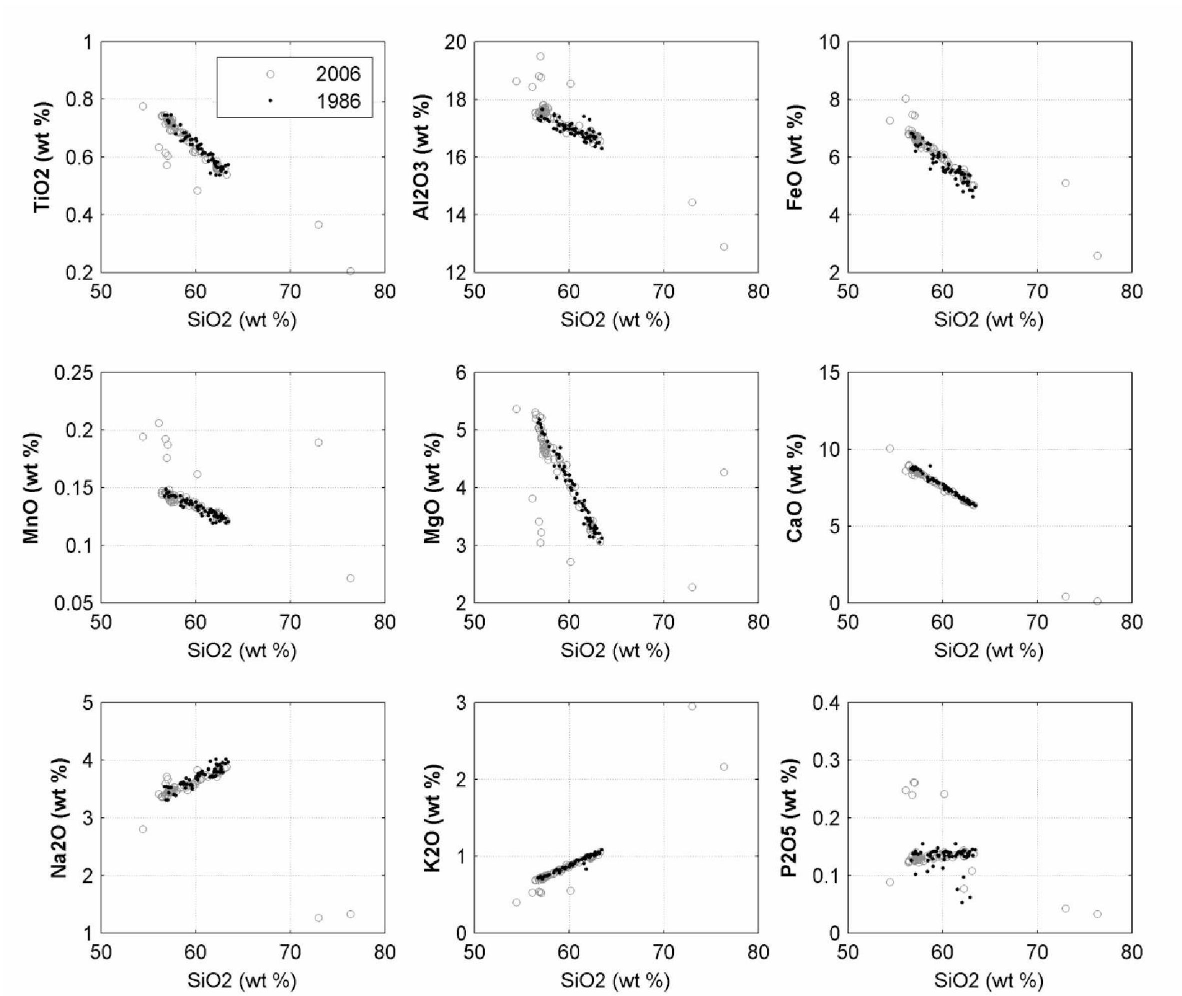

Figure 2.3 Silica variation diagrams demonstrating general similarities of whole-rock, major element composition in pyroclastic material from Augustine's 1986 and 2006 eruptions.

2.4 Datasets

2.4.1 Available SAR data

To study PFDs related to the 1986 and the 2006 eruption, the use of data from multiple SAR sensors is a practical necessity. No single SAR sensor was in service for the nearly 20-year period between the 1986 and 2006 eruptions, and no permanent spaceborne SAR system existed at the time of the 1986 eruption. The first European Remote Sensing (ERS) satellite, ERS-1, did not fly until 1991 (Rignot and van Zyl, 1993), and both ERS-2 and Canada's Radarsat-1 were launched in 1995 (Morena et al., 2004; ESA, 2011). The Phased Array L-band Synthetic Aperture Radar (PALSAR) aboard Japan's Advanced Land Observing Satellite (ALOS) was the most recent sensor used in this study. ALOS-PALSAR was launched on 24 January 2006, but was not operational until October 2006 (Rosenqvist et al., 2007), several months after the cessation of the 2006 eruptive activity.

To analyze the eruption deposits, we obtained a total of 48 SAR single look complex (SLC) images acquired between 21 June 1992 and 9 October 2010. The images were acquired across four platforms, in C-band and L-band wavelengths (λ). C-band data were obtained from Radarsat-1 (λ = 5.6 cm), ERS-1, and ERS-2 (λ = 5.66 cm); L-band data (λ = 23.62 cm) were acquired by ALOS-PALSAR. All SAR data used in this study together with their platform identifiers are listed in Table 2.1.

Table 2.1 SAR data used to produce interferometric data for the 1986 and 2006 Augustine Volcano eruptions.

Granule	Platform	Date	Orbit	Path	Frame	Ascend/ Descend
E1_04883_STD_F301	ERS1	21-Jun-1992	4883	229	301	D
E1_05384_STD_F301	ERS1	26-Jul-1992	5384	229	301	D
E1_06386_STD_F301	ERS1	4-Oct-1992	6386	229	301	D

Table 2.1 (Continued) SAR data used to produce interferometric data for the 1986 and 2006 Augustine Volcano eruptions.

Granule	Platform	Date	Orbit	Path	Frame	Ascend/ Descend
E1_10394_STD_F301	ERS1	11-Jul-1993	10,394	229	301	D
E1_10895_STD_F301	ERS1	15-Aug-1993	10,895	229	301	D
E1_11396_STD_F301	ERS1	19-Sep-1993	11,396	229	301	D
E1_21259_STD_F301*	ERS1	8-Aug-1995	21,259	229	301	D
E1_21760_STD_F301	ERS1	12-Sep- 1995	21,760	229	301	D
E2_06596_STD_F301	ERS2	24-Jul-996	6596	229	301	D
E2_12107_STD_F301*	ERS2	13-Aug-1997	12,107	229	301	D
E2_17618_STD_F301*	ERS2	2-Sep-1998	17,618	229	301	D
E2_23129_STD_F301	ERS2	22-Sep-1999	23,129	229	301	D
E2_27137_STD_F301	ERS2	28-Jun-2000	27,137	229	301	D
E2_27638_STD_F301	ERS2	2-Aug-2000	27,638	229	301	D
E2_28139_STD_F301	ERS2	6-Sep-2000	28,139	229	301	D
E2_32648_STD_F301	ERS2	18-Jul-2001	32,648	229	301	D
E2_33650_STD_F301	ERS2	26-Sep-2001	33,650	229	301	D
E2_38159_STD_F301	ERS2	7-Aug-2002	38,159	229	301	D
E2_38660_STD_F301	ERS2	11-Sep-2002	38,660	229	301	D
E2_42167_STD_F301	ERS2	14-May 2003	42,167	229	301	D
E2_42668_STD_F301	ERS2	18-Jun-2003	42,668	229	301	D
E2_43670_STD_F301	ERS2	27-Aug-2003	43,670	229	301	D
E2_44171_STD_F301	ERS2	1-Oct-203	44,171	229	301	D

Table 2.1 (Continued) SAR data used to produce interferometric data for the 1986 and 2006 Augustine Volcano eruptions.

Granule	Platform	Date	Orbit	Path	Frame	Ascend/ Descend
E2_48680_STD_F301	ERS2	11-Aug-2004	48,680	229	301	D
E2_53189_STD_F301	ERS2	22-Jun-2005	53,189	229	301	D
E2_53690_STD_F301	ERS2	27 Jul-2005	53,690	229	301	D
E2_54692_STD_F301	ERS2	5-Oct-2005	54,692	229	301	D
R1_53774_ST6_F149	R1	22-Feb- 2006	53,774	182	149	A
R1_54117_ST6_F149	R1	18-Mar-2006	54,117	182	149	A
R1_54460_ST6_F149	R1	11-Apr-2006	54,460	182	149	A
R1_54803_ST6_F149	R1	5-May 2006	54,803	182	149	A
R1_55146_ST6_F149	R1	29-May 2006	55,146	182	149	A
R1_55832_ST6_F149	R1	16-Jul-2006	55,832	182	149	A
R1_56175_ST6_F149	R1	9-Aug-2006	56,175	182	149	A
R1_56518_ST6_F149	R1	2-Sep-2006	56,518	182	149	A
R1_56861_ST6_F149	R1	26-Sep-2006	56,861	182	149	A
R1_57204_ST6_F149	R1	20-Oct-2006	57,204	182	149	A
R1_57547_ST6_F149	R1	13-Nov-2006	57,547	182	149	A
R1_59948_ST6_F149	R1	30-Apr-2007	59,948	182	149	A
ALPSRP076331180	PALSAR	1-Jul-2007	7633	270	1180	A
ALPSRP083041180	PALSAR	16-Aug-2007	8304	270	1180	A
ALPSRP089751180	PALSAR	1-Oct-2007	8975	270	1180	A
ALPSRP190401180	PALSAR	21-Aug-2009	19,040	270	1180	A
ALPSRP197111180	PALSAR	6-Oct-2009	19,711	270	1180	A

Table 2.1 (Continued) SAR data used to produce interferometric data for the 1986 and 2006 Augustine Volcano eruptions.

Granule	Platform	Date	Orbit	Path	Frame	Ascend/ Descend
ALPSRP230661180	PALSAR	24-May 2010	23,066	270	1180	A
ALPSRP237371180	PALSAR	9-Jul-2010	23,737	270	1180	A
ALPSRP244081180	PALSAR	24-Aug-2010	24,408	270	1180	A
ALPSRP250791180	PALSAR	9-Oct-2010	25,079	270	1180	A

2.4.2 Ancillary data used in this study

The reference digital elevation model (DEM), used for InSAR analysis was acquired during the Shuttle Radar Topography Mission (SRTM) in February, 2000 (tile No. SRTM1N59W154V2). SRTM was a cooperative project of the National Aeronautics and Space Administration (NASA), the National Imagery and Mapping Agency (now the National Geospatial Intelligence Agency, or NGA), and the German agency *Deutches Zentrum für Luft und Raumfahrt* (DLR) (van Zyl, 2001). The SRTM elevation data were processed from original radar signals spaced at intervals of 1 arc-second (~30 meters), with additional, later processing employed to fill voids where initial processing did not meet mission specifications. The SRTM data meet absolute horizontal and vertical accuracies of 20 m (circular error at 90% confidence) and 16 m (linear error at 90% confidence). In North America, the relative vertical accuracy of the SRTM DEM was measured to be 7 m (linear error at 90% confidence) (Rodriguez et al., 2005).

2.5 Data processing methods

Data processing was conducted in two steps. In the first step, SAR data from ERS-1/2, Radarsat-1, and ALOS-PALSAR sensors were separately processed to evaluate PFD subsidence between 1992 and 2010 (Section 4.1). Emphasis was placed on deformation occurring on Augustine's north flank, where the great majority of PFDs were emplaced. In a second step, these subsidence data were used to derive geophysical information, such as deposit thickness and deformation behavior, for both the 1986 and 2006 PFDs. This latter process proved less straightforward, however, because data acquired after the 2006 eruption measures the combined deformation of superimposed multiple generations (1986 and 2006) of PFDs. We therefore devised an approach that decomposes contributions from 1986 and 2006 PFDs by combining subsidence data with geophysical models. In the following sub-sections, we will describe those models and the processing methods used in this two-step strategy. A geophysical interpretation of results is presented in Section 2.6. A summary of variables used in the following Eqs. 2.1 – 2.16 is presented as Appendix A.

2.5.1 Methods: differential InSAR (d-InSAR) time-series processing

Differential InSAR (d-InSAR) time-series analysis techniques use the phase measurements of a stack of $N + 1$ co-registered SAR images observed at image acquisition times $[t_0, \dots, t_N]$, to extract accurate information about the (time-dependent) deformation of an observed surface. To this end, a set of M interferograms is first formed from the $N + 1$ images using InSAR processing, which calculates the phase difference $\phi_{i,j}$ (typically referred to as the interferometric phase) between pairs of SAR images according to

$$\phi_{i,j} = \varphi_i - \varphi_j \qquad (2.1)$$

where $\phi_{i,j}$ is the interferometric phase measurement calculated from SAR images i and j ($i, j \in (N + 1)$ and $i < j$). As shown in Eq. 2.2, the phase values in Eq. 2.1 contain information about the topography h of the observed surface encoded in phase component ($\phi_{i,j,topo}$) as well as the surface deformation $\Delta d_{i,j} = \left(d_j - d_i\right)$ that occurred between the image acquisition times t_i and t_j ($\phi_{i,j,defo}$). In addition to these desired parameters, however, $\phi_{i,j}$ is furthermore affected by differences in the atmospheric stratification at times t_i and t_j ($\phi_{i,j,atm-s}$), variations in the distribution of atmospheric water vapor ($\phi_{i,j,atm-t}$), errors in satellite orbits ($\phi_{i,j,orbit}$), and noise ($\phi_{i,j,noise}$), such that $\phi_{i,j}$ can be written as

$$\phi_{i,j} = \phi_{i,j,defo} + \phi_{i,j,topo} + \phi_{i,j,atm-s} + \phi_{i,j,atm-t} + \phi_{i,j,orbit} + \phi_{i,j,noise} \quad (2.2)$$

The sensitivity of the phase values in Eq. 2.2 to the target parameters h (surface topography), and $\Delta d_{i,j}$, (surface deformation), is given by:

$$\phi_{i,j,topo} = \frac{4\pi}{\lambda} \frac{B_{i,j,\perp}}{r \cdot sin(\theta)} h \quad (2.3)$$

and

$$\phi_{i,j,defo} = \frac{4\pi}{\lambda} (d_j - d_i) \quad (2.4)$$

where $B_{i,j,\perp}$ is the perpendicular baseline between SAR acquisitions i and j, r is the sensor-to-target range, θ is the look angle of the system, and λ is the wavelength of the transmitted signal.

In this study, we use d-InSAR time-series analysis techniques to extract information about the time-dependent surface deformation $d_n = [d_0, \dots, d_N]$ of PDFs emplaced on Augustine's northern flank during both the 1986 and 2006 eruptions from the measurements in Eq. 2.2. From SAR data acquired after the 2006 eruption, we extract information about the thickness $h_{PFD,06}$ of PFD deposits emplaced by this eruption. Here, we interpret the SAR-observed post-eruptive surface topography h in Eq. 2.3 as the combination of a pre-eruptive DEM h_{pe} and the thickness $h_{PFD,06}$ of 2006 deposits, i.e., $h = h_{pe} + h_{PFD,06}$.

To extract d_n from the observed phase measurements, $\phi_{i,j}$, we first mitigate phase signals related to the pre-eruptive DEM h_{pe} from Eq. 2.2 by subtracting topographic phase values obtained from the 1 arc-second resolution SRTM digital elevation model (d-InSAR processing). We subsequently model and subtract stratified atmospheric phase signals ($\phi_{i,j,atm-s}$) from Eq.

2.2 using the Weather Research and Forecasting (WRF) model and following the approach described in Gong et al., (2015a; 2015b). This separate step is required as stratified atmospheric signals are significant at Augustine and can often not be removed using spatial or temporal filters. Finally, we mitigate orbital errors ($\phi_{i,j,orbit}$) by referencing all phase values to a stable region near the PFDs of interest, and apply an adaptive phase filter (Goldstein and Werner, 1998) to minimize $\phi_{i,j,noise}$.

After individually unwrapping the filtered differential interferograms using a minimum-cost-flow unwrapping algorithm (Costantini, 1998), the unwrapped *differential* interferometric phase resulting from these processing steps can be written as

$$\Delta\phi_{i,j} \approx \frac{4\pi}{\lambda}\left(d_j - d_i\right) + \frac{4\pi}{\lambda}\frac{B_{i,j,\perp}}{r \cdot sin(\theta)}\Delta h \quad + \phi_{i,j,atm-t} + \phi_{i,j,noise} \tag{2.5}$$

where Δh is a residual topography signal that may be due to errors in h_{pe} or due to real changes of topography since the acquisition of h_{pe}.

A final set of two processing steps remain to arrive at estimates for the deformation time series d_n. First, we apply the small baseline subset (SBAS) algorithm of Berardino et al., (2002) to the data in Eq. 2.5. In SBAS, interferograms are formed from the subset of all possible SAR image pairs, whose temporal (B_t) and spatial baselines ($B_\perp$) are within pre-defined thresholds. By limiting B_t and $B_\perp$, SBAS addresses the difficult problem of coherence loss, or decorrelation, in interferometric data (Berardino et al., 2002; Agram et al., 2013) and therefore reduces the impact of $\phi_{i,j,noise}$ on $\Delta\phi_{i,j}$. Moreover, processing interferograms within the SBAS framework reduces atmospheric effects $\phi_{i,j,atm-t}$ in Eq. 2.5, by applying spatial and temporal filters to the InSAR time-series data (Lee et al., 2010). By inverting the differential phase measurements $\Delta\phi_{i,j}$ in Eq.

2.5, the algorithm results in the reconstructed phase history $\Delta\varphi_n$ at the $N + 1$ image acquisition times $[t_0, \dots, t_N]$

$$\Delta\varphi_n = \frac{4\pi}{\lambda} \frac{B_{n,\perp}}{r \cdot sin(\theta)} \Delta h \quad + \frac{4\pi}{\lambda} d_n \tag{2.6}$$

For reasons of simplicity, Eq. 2.6 assumes that atmosphere and noise influences were sufficiently reduced by the filtering steps in our SBAS workflow so that they can be considered negligible and dropped from the equation. This approximation is made to keep the description of our processing approach mathematically short. Note that in reality, noise and atmospheric effects are only reduced but not eliminated during SBAS processing.

In addition to $\Delta\varphi_n$, we also derive an estimate of its uncertainty, $\sigma_{\Delta\varphi_n}$, through our SBAS implementation. This uncertainty estimate is derived for each pixel and epoch using a jackknifing approach: For our dataset of M interferograms formed from $N + 1$ SAR acquisitions, we calculate $N + 1$ solutions for $\Delta\varphi_n$ by recursively dropping the nth acquisition date from our list of observations. The standard deviation of the $N + 1$ derived solutions for $\Delta\varphi_n$ forms the uncertainty estimate $\sigma_{\Delta\varphi_n}$. Note, that our approach for uncertainty estimation does not consider spatial correlations between pixels that might be introduced by residual atmospheric signals as well as by the application of spatial filters in our workflow. These correlations are currently ignored but could be included in the future.

In Eq. 2.6, the variable d_n is the cumulative line-of-sight displacement at time t_n, and $B_{n,\perp}$ is the perpendicular baseline between the SAR image acquisition at time t_n and the reference-image acquisition at time t_0.

For interferometric data acquired before Augustine's 2006 eruption, we assume that Δh is small such that its impact on $\Delta\varphi_n$ can be ignored and the deformation time series d_n can be directly extracted from Eq. 2.6. To validate this assumption, we have analyzed short term ERS-

1/2 interferograms with spatial baselines typical for our ERS data stack (up to ~250 m) over non-deforming areas of the Augustine edifice and found residual phase signals with a standard-deviation of about 0.8 rad. The spatial pattern of these residual signals suggests atmospheric delay effects as the main source. Hence, we decided to not correct for topographic effects but rather model their error influence according to Eq. 2.3 and consider them in the statistical model for the estimation of d_n along with phase noise due to the data's coherence properties. Here, we use $\sigma_{h_{pe}} = 7m$ to model the accuracy of the SRTM DEM, which is its relative height error estimated by Rodriguez et al., (Rodriguez et al., 2005) for the North American continent.

For data acquired after 2006, we assume that the residual topography signal is an expression of the deposit thickness $h_{PFD,06}$ and apply the approach by Fattahi and Amelung (2013) to jointly estimate the unknown parameters of the deformation time series d_n from the unknown PFD thickness $h_{PFD,06}$. Errors in the pre-eruption DEM ($\sigma_{h_{pe}}$) were included in the error model for $h_{PFD,06}$. Interested readers are referred to Berardino et al. (2002) and Fattahi and Amelung (2013) for more technical details on the applied SBAS and DEM error estimation approaches.

Using this approach, we derive line-of-sight deformation time-series information separately from the ERS1/2, Radarsat-1, and ALOS PALSAR data, resulting in the deformation time series d_n^{92-05}, d_n^{06-07}, and d_n^{07-10}, respectively. To reduce the influence of any potential larger-scale, magma-related deformation of Augustine's edifice on the deformation estimates, we chose three reference points on the north flank that were unaffected by PFDs (Figure 2.2b). To facilitate subsequent joint processing of these time-series data (Section 4.2), we assume that PFD deformation is dominated by vertical subsidence motion (Briole et al., 1997; Lee et al., 2008), and project all deformation measurements together with their error properties into a joint vertical reference frame, resulting in the subsidence estimates s_n^{92-05}, s_n^{06-07}, and s_n^{07-10}, with their respective uncertainty measures σ_{s_n}. The assumption of vertical motion is consistent with other work on Augustine's PFDs (Lee et al., 2008).

From the ALOS PALSAR data, acquired after the 2006 eruption, we furthermore derive an estimate for the thickness $h_{PFD,06}$ of the 2006 PFDs. In Section 4.2, we introduce an inversion approach that is used to estimate physical parameters for the 1986 and the 2006 PFD deposits from these measurements.

Note, that a similar approach for the joint estimation of the thickness and subsidence of volcanic deposits was also applied by Ebmeier et al., (2012). There, InSAR data was used to estimate thickness and deformation of lava deposits on Santiaguito Volcano, Guatemala. In contrast to their approach, which measured the cumulative deformation of material deposited during an extended extrusive event, we are tracking deposit deformation across two eruptive cycles that resulted in a superposition of multiple generations of PFDs. Hence, in our case, further processing is needed to decompose contributions from 1986 and 2006 PFDs and extract geophysical information for the individual PFD generations.

2.5.2 Methods: geophysical model of PFD parameter estimation

The overall goal of this study is to extract geophysical information about the 1986 and 2006 PFDs from the InSAR-derived subsidence estimates, s_n^{92-05}, s_n^{06-07}, and s_n^{07-10}. This effort is complicated (at Augustine and at most other active volcanoes) by younger 2006 deposits that are superimposed onto earlier 1986 material (Figures 2a and 2b). Consequently, surface deformation data acquired after the 2006 eruption includes the effect of subsiding new material as well as residual contraction of the underlying 1986 deposits.

2.5.2.1 Geophysical considerations and model assumptions

To discriminate between contributions from individual deposits in our deformation measurements, we employ a simplified model that assumes the contraction behavior of 1986 and 2006 deposits can be modeled using the same physical principles and same material parameters. We base this assumption on the geochemical similarity of eruption products from both 1986 and 2006, as described in Figure 2.3 and Section 2.3.

We further consider four possible geophysical sources that may give rise to the observed deformation at Augustine-type PFDs: (1) surface deflation due to loss of volatiles; (2) surface inflation or deflation caused by volume changes in the magma reservoir; (3) poroelastic deformation caused by loading; and (4) thermoelastic surface deformation due to cooling. Of these four mechanisms, only two—deformation from loading, and thermoelastic cooling—were considered significant. Whereas loss of volatiles contributes to deformation, observations of deflating PFDs acquired at Mount St. Helens in 1980 indicate that most deflation occurs immediately—within hours or days—after emplacement (Rowley et al., 1981). We assume that gas deflation at Augustine was similar in timing and extent, and, therefore, deformation from deflation was complete before satellite observations were made after the 1986 and 2006 eruptions.

Centimeter-scale ground deformation attributed to magma movement, particularly in periods immediately preceding or following an eruption, is well established in a number of previous studies (e.g., Lanari et al., 1998; Massonnet and Feigl, 1998; Lu et al., 2000; Lu et al., 2002; Masterlark and Lu, 2004; Lu et al., 2010). At Augustine, however, magma source-related deformation has been subtle and at or below the detection level of geodetic systems for most of its recent history. Both an InSAR analysis of Augustine from 1992 to 1999 (Lu et al., 2003) and

a study based on optical, electronic, and GPS surveying techniques (Pauk et al., 2001) found no evidence of magma-related deformation. While subtle magma-related deformation signals were found for the time period 1988–2000 from both reprocessed GPS data and InSAR data (Lee et al., 2010), the magnitude of the signal was near the detection level of both techniques.
An exception to this general behavior was a deformation episode that started immediately before and lasted through the initial stages of the 2006 eruption (Cervelli et al., 2006). While this deformation was significant, it occurred at a time not covered by our SAR data and had almost entirely ceased at the time of our first SAR acquisition after the 2006 eruption. We therefore ignore magma source-related deformation in our geophysical model. Note, that our choice of a reference point nearby the deforming PFDs further mitigates magma-induced surface deformation signals that may have existed.

The remaining sources of deformation considered in our model are compaction-related poroelastic deformation and thermal contraction. We are able to pretermit the effects of compaction as a cause of persistent subsidence, because such effects last as little as hours or days after emplacement (Rowley et al., 1981; Lee et al., 2008), while thermoelastic contraction persists for years (Masterlark et al., 2006). Our consideration of poroelastic compaction is therefore limited to the period immediately after emplacement (Eq. 2.8). Finally, we assume that the subsidence time series s_n^{92-05}, s_n^{06-07}, and s_n^{07-10} are sufficiently linear such that they can be approximated by linear functions of the form:

$$s_n = \Delta s \cdot t_n \tag{2.7}$$

where Δs is the linear subsidence rate in $cm \cdot y^{-1}$. This linearity assumption has major advantages when formulating our geophysical model as it significantly reduces the number of unknowns that need estimation. As some researchers (e.g., (Lee et al., 2008)) have proposed exponential models in the past, we provide a more detailed justification for this linearity assumption in Section 2.6.1 where we show that the model in Eq. 2.7 is supported by the data.

With these prerequisites in place, we were able to construct a forward model that relates each of the subsidence rate estimates, Δs^{92-05}, Δs^{06-07}, and Δs^{07-10} to physical parameters of the 1986 and 2006 PFDs.

2.5.2.2 Model formulation

Because poroelastic deformation of the 1986 PFDs had likely ceased before the start of our observation time series, we are able to limit our estimate of the initial subsidence rate, Δs^{92-05}, to a function of thermoelastic contraction and thickness:

$$\Delta s^{92-05} = \bar{\gamma}_{th} \cdot h_{PFD,86}; \text{ [cm t}^{-1}\text{]} \tag{2.8}$$

where $h_{PFD,86}$ [m] is the (unknown) thickness of the 1986 deposits and $\bar{\gamma}_{th} = \alpha_L \cdot \bar{k}$ [cm t^{-1} m^{-1}] is the unknown average thermoelastic contraction parameter of Augustine-type PFDs that is proportional to the material's thermal contraction coefficient α_L and its time-averaged cooling rate $\bar{k}$.

The second subsidence rate, Δs^{06-07}, describes the deformation behavior *immediately* after the emplacement of the 2006 PFDs. Because it is affected by poroelastic and thermoelastic deformation of 2006 materials as well as thermoelastic deformation of underlying 1986 materials, it is modeled as:

$$\begin{aligned} \Delta s^{06-07} &= \left(\bar{\gamma}_{pe} + \bar{\gamma}_{th}\right) \cdot h_{PFD,06} + \Delta s^{92-05} \quad \text{or} \\ \left(\Delta s^{06-07} - \Delta s^{92-05}\right) &= \left(\bar{\gamma}_{pe} + \bar{\gamma}_{th}\right) \cdot h_{PFD,06} \end{aligned} \tag{2.9}$$

where $\bar{\gamma}_{pe}$ [cm t^{-1} m^{-1}] is an average poroelastic contraction parameter and $\bar{\gamma}_{th}$ is the average thermoelastic contraction parameter from Eq. 2.8.

For the third subsidence rate, Δs^{07-10}, which starts more than one year after emplacement of the 2006 PFDs, we assume that poroelastic contraction has ceased, such that:

$$(\Delta s^{07-10} - \Delta s^{92-05}) = \bar{\gamma}_{th} \cdot h_{PFD,06} \tag{2.10}$$

Note that the average thermoelastic contraction parameter $\bar{\gamma}_{th}$ is assumed to be identical for the 1986 and the 2006 PFDs. This assumption is based on their compositional similarity (as shown in Figure 2.3).

To solve this system of equations.(Eqs. 2.8 – 2.10), we apply two consecutive, linear least-squares inversions. In the first, we derive estimates for the parameters $\bar{\gamma}_{th}$ and $\bar{\gamma}_{pe}$ from Eqs. 2.9 and 2.10 using a least-squares parameter estimation in the Gauss-Markov model (Plackett, 1950). To that end, Eq. 2.8 and Eq. 2.9 are rearranged to take the form:

$$b + \hat{\varepsilon} = A \cdot \hat{x} \tag{2.11}$$

In Eq. 2.11, b is a $(2 \cdot R \cdot C) \times 1$ column vector of observations, with R and C being the number of rows and columns of the InSAR data matrix; $\hat{\varepsilon}$ is the $(2 \cdot R \cdot C) \times 1$ column vector of estimated residuals; $\hat{x}$ is the 2×1 column vector of unknowns; and A is the $(2 \cdot R \cdot C) \times 2$ design matrix containing the partial derivatives of the forward model in Eq. 2.8 and Eq. 2.9 with respect to the unknowns $\hat{x}$ ($\partial Eq.(9)/\partial\bar{\gamma}_{th} = \partial Eq.(10)/\partial\bar{\gamma}_{th} = h_{PFD,06}$; $\partial Eq.(9)/\partial\bar{\gamma}_{pe} = h_{PFD,06}$; $\partial Eq.(10)/\partial\bar{\gamma}_{pe} = 0$).

We model errors in observations using covariance matrix Σ_{bb} from which we derive a matrix of weights P_{bb} for the observations b in the parameter inversion according to:

$$P_{bb} = (\Sigma_{bb})^{-1} \tag{2.12}$$

The covariance matrix Σ_{bb} is a diagonal matrix containing the variances $\sigma_{\Delta s}^2$ of the subsidence rate estimates, Δs. The values $\sigma_{\Delta s}^2$ are derived by propagating the uncertainties σ_{s_n}

through Eq. 2.7. Following the Gauss-Markov theorem, the optimal solution for the problem in Eq. 2.11 is found by minimizing the object function δ:

$$\delta = \hat{\varepsilon}^T P_{bb} \hat{\varepsilon} \rightarrow min \tag{2.13}$$

Solving this minimization problem yields the estimated unknowns $\hat{x} = [\bar{\gamma}_{th} \quad \bar{\gamma}_{pe}]^T$ with their covariance properties $\Sigma_{\hat{x}\hat{x}}$ according to:

$$\begin{array}{rcc} \hat{x} & = & (A^T P_{bb} A)^{-1} A^T P_{bb} b \\ \Sigma_{\hat{x}\hat{x}} & = & (A^T P_{bb} A)^{-1} \end{array} \tag{2.14}$$

resulting in estimates for $\bar{\gamma}_{th}$ and $\bar{\gamma}_{pe}$.

Once these parameters were derived, the estimate for $\bar{\gamma}_{th}$ together with its accuracy properties are used in a second inversion of Eq. 2.7 to derive estimates for the thickness $\hat{h}_{PFD,86}$ of the PFDs emplaced by Augustine's 1986 eruption. As observations and unknowns cannot be formally separated in Eq. 2.7, the Gauss-Markov theorem is not applicable and a General Least-Squares (GLS) solution must be sought instead. In the GLS case, the functional model is formulated as:

$$\Delta s^{92-05} - \bar{\gamma}_{th} \cdot \hat{h}_{PFD,86} = 0 \tag{2.15}$$

where $\bar{\gamma}_{th}$ is now treated as an observation with known error properties. To solve Eq. 2.15 for the unknown deposit thickness $\hat{h}_{PFD,86}$, we solve:

$$\begin{array}{rcc} \hat{x} & = & (B\Sigma_{bb}B^T)^{-1} A (A^T (B\Sigma_{bb}B^T)^{-1} A)^{-1} Bb \\ \Sigma_{\hat{x}\hat{x}} & = & (A^T (B\Sigma_{bb}B^T)^{-1} A)^{-1} \end{array} \tag{2.16}$$

on a pixel-by-pixel basis. In Eq. 2.16, $\hat{x}$ is the $(R \cdot C) \times 1$ sized vector of unknown deposit thickness values $\hat{h}_{PFD,86}$, A is again the design matrix, and B is a matrix containing the partial derivatives of Eq. 2.15 with respect to the observations.

Results of the application of the parameter estimation models in Eq. 2.14 and Eq. 2.16 to the data in s_n^{92-05}, s_n^{06-07}, s_n^{07-10}, and $h_{PFD,06}$ are shown in Section 2.6.2.

2.6 Results

2.6.1 d-InSAR-based estimates of surface subsidence and 2006 PFD thickness

We estimated s_n^{92-05}, s_n^{06-07}, and s_n^{07-10}, and 2006 PFD thickness $h_{PFD,06}$ by applying the techniques in Section 2.4.1 to a total of 48 single look complex (SLC) SAR images. Subsidence estimates s_n^{92-05} were based on a stack of 27 ERS-1/2 images acquired between the 1986 and the 2006 eruptions. s_n^{06-07} was estimated from 12 Radarsat-1 images acquired within the first 12 months after the 2006 eruption. The parameters s_n^{06-07} and $h_{PFD,06}$ were derived from nine ALOS-PALSAR images with acquisition dates between July 2007 and October 2010 (Table 2.1). October 2010 was the last seasonally appropriate ALOS-PALSAR acquisition of the target area. In April 2011, the ALOS satellite suffered a non-recoverable power generation anomaly. It was permanently powered down on 12 May 2011 (JAXA, 2011).

Time-baseline plots showing the interferograms selected for the three data stacks are shown in Figure 2.4, along with the spatial and temporal baseline thresholds (B_t^{max} and $B_\perp^{max}$) that were used in the interferogram selection process. Baseline thresholds were set empirically to optimize InSAR coherence and reduce the number of unconnected interferogram subsets. Note that, for the ERS-1/2 data stack, three interferograms with a larger geometric baseline but with good coherence were added to the dataset to keep the number of unconnected interferogram subsets low.

Average subsidence rates Δs (Eq. 2.7) were derived for the three subsidence time series and are plotted in Figure 2.5a–c. For all three datasets, a spatial coherence threshold of 0.2 was set to discard incoherent regions. Coherence loss is particularly evident in the Radarsat-1 time series,

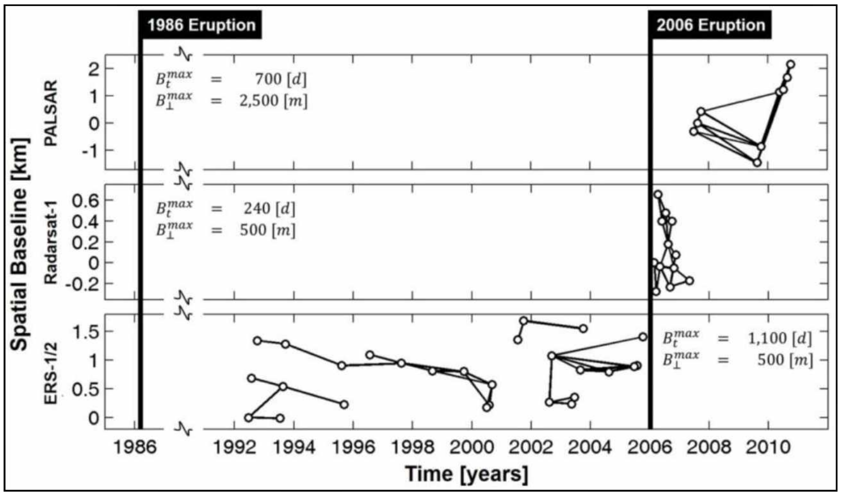

Figure 2.4 Time and spatial baseline diagrams indicating SAR pairs selected for interferometric processing.

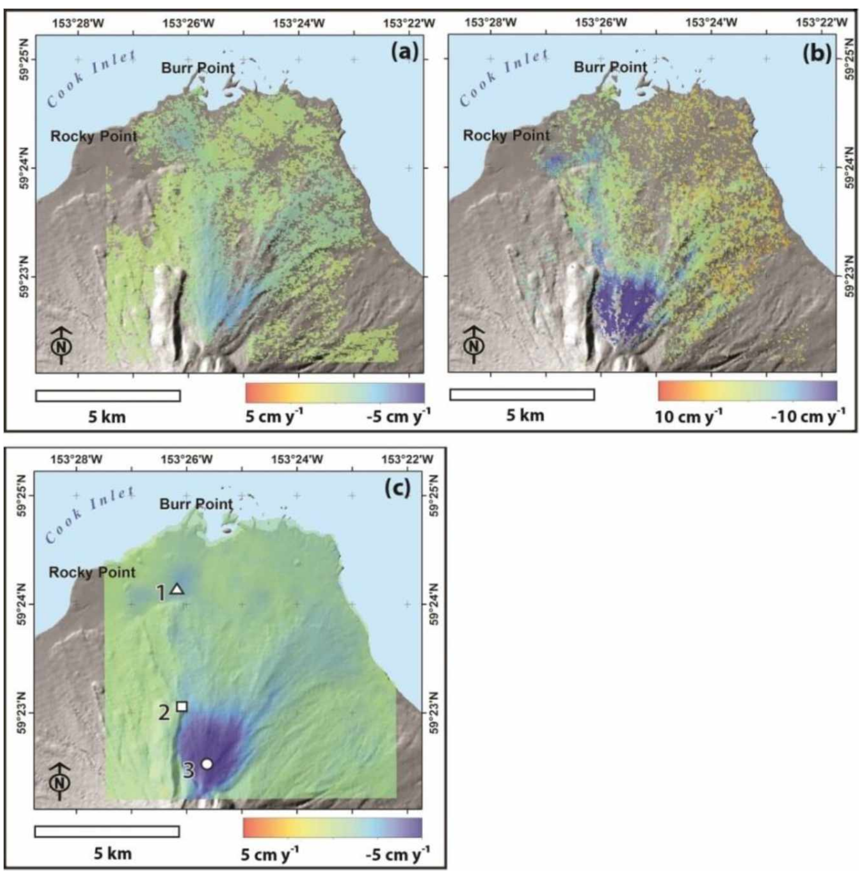

Figure 2.5 Average deformation rates (Δs) obtained by InSAR time-series analysis [cm·y-1]; deformation rates (apply to (**a**) ERS-1/2 (June 1992 to October 2005); (**b**) Radarsat-1 (6 February–7 April); and (**c**) ALOS-PALSAR (July 2007 to October 2010). Locations labeled 1, 2, and 3 in (**c**) are data points whose deformation across each time series is plotted in Figure 2.6. Note that the deformation key shown for Radarsat-1 data in figure (**b**) is shown at a smaller scale than (**a**) or (**c**), to accommodate the higher subsidence that occurred immediately after the 2006 eruption.

(s_n^{06-07}), where rapid surface change in the first months after the eruption resulted in extended no-data areas (transparent regions in Figure 2.5b). Figure 2.5 shows that largest subsidence rates are found for the time period immediately following the eruption (Δs^{06-07}; Figure 2.5b) where poroelastic and thermoelastic deformation of newly deposited 2006 materials, as well as thermoelastic deformation of underlying 1986 deposits, lead to subsidence rates of up to 20 $cm \cdot y^{-1}$. Figure 2.5 also demonstrates that the spatial pattern of subsidence changes after the 2006 eruption, which can be attributed to the newly deposited material Subsidence time series for three points on Augustine's PFDs (indicated by rectangle, triangle and circular symbols in Figure 2.5c) are shown in Figure 2.6 as black and gray lines. To create these plots, the post-2006

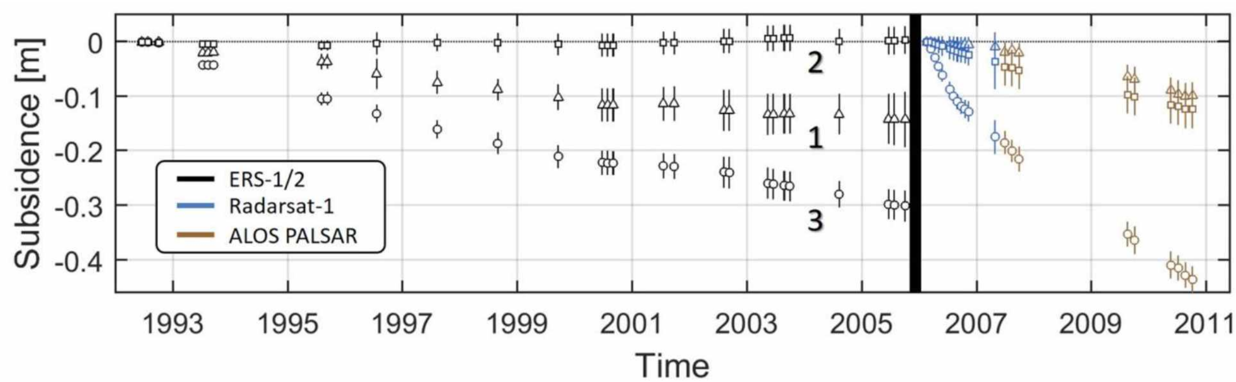

Figure 2.6 Subsidence measured by InSAR at each of three locations on Augustine Volcano's north flank. The data points (labeled 1, 2, and 3 and indicated by different symbols) correspond to locations shown in Figure 2.5c. Error bars indicate the precision of the measurements and points are color coded by satellite. Bold vertical bars represent dates of eruptions. Vertical bar represents the 2006 eruption.

deformation estimates s_n^{06-07} and s_n^{07-10} were connected using an offset parameter, estimated using least-squares techniques constrained by a minimum-norm assumption. The black subsidence time series (lines 1 and 3) corresponds to two locations that were covered by both the 1986 and the 2006 PFDs. Correspondingly, their deformation between 1992 and 2005 relates to cooling of 1986 flows. Figure 2.5c illustrates that stronger deformation occurs near Augustine's summit crater that is attributed to the area's greater thickness of PFDs, observable in Figure 2.7a,b. Following deposition of the 2006 PFDs, deformation rates near the crater increased due to the combined subsidence of both 1986 and 2006 material. The subsidence time series No. 2, indicated by the gray line in Figure 2.6, is taken from a location that was only affected by 2006 flows (Figure 2.5c); consequently, surface deformation from 1992 to 2005 is zero, as expected.

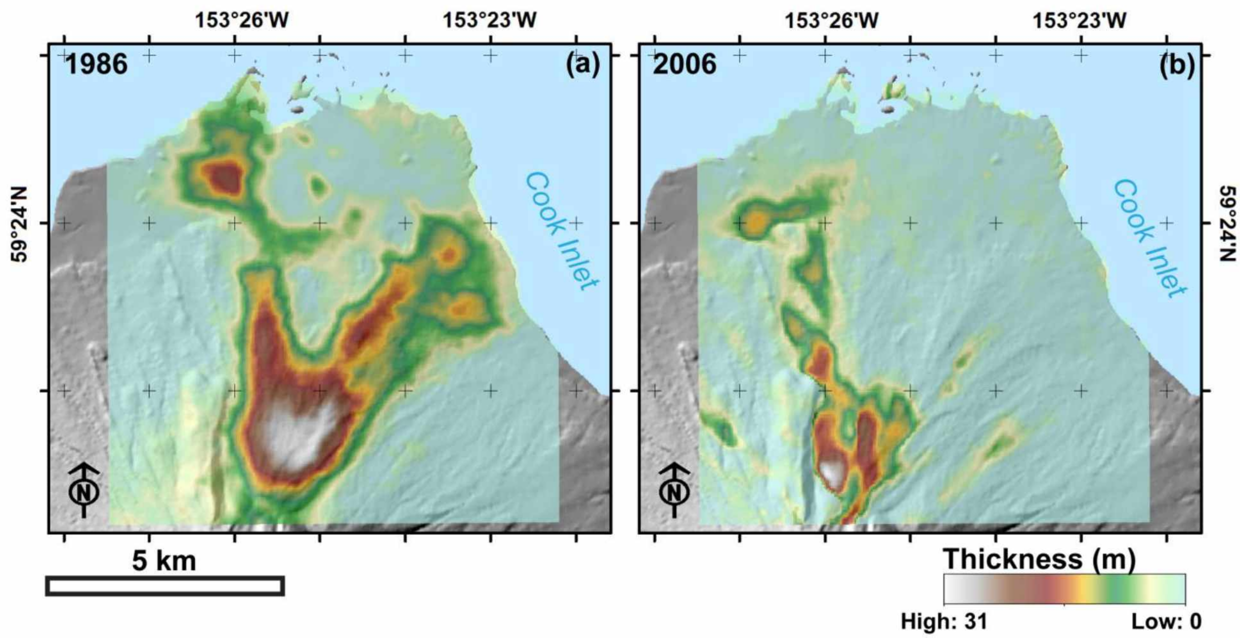

Figure 2.7: Thickness plot of (**a**) 1986 pyroclastic flow deposits and (**b**) 2006 pyroclastic flow deposits on Augustine Volcano's north flank. Maximum deposits reach a thickness of ~31m (in white) near the summit crater.

In addition to surface subsidence, we estimate the thickness $h_{PFD,06}$ of pyroclastic flow material deposited during the 2006 eruption using the method described in Section 4.1. Based on our error model, which considers the distribution of perpendicular baselines as well as error sources related to coherence and DEM accuracy, $h_{PFD,06}$ could be estimated with an average error of $\sigma h_{PFD,06}$ = 2.1 m. A map of $h_{PFD,06}$ is presented in Figure 2.7b showing deposition predominantly in a northerly direction from the summit with thickest deposits (> 30m) found just north of Augustine's summit. From these data, the total volume of 2006 PFD deposits was 3.3×10^7 m^3 (0.033 km^3) $\pm 0.11 \times 10^7$ km^3, with a maximum thickness of ~31 m, and a mean of ~5 m.

These estimates compare well to field observations of the 2006 PFDs by Coombs et al. (2010a), who identified the difficulty of thickness measurements and/or estimates as a main source of uncertainty in volume and yield calculations for the 2006 eruption. With that steep slopes and flow edges, to a maximum of 10–15 m in the distinctive Rocky Point pyroclastic flow; see Figures 2b and 7b (Coombs et al., 2010a; Vallance et al., 2010). A comparison of digital terrain models of the volcano's edifice, acquired before and after the eruption, indicates a maximum thickness of 20 m (Vallance et al., 2010), and the inflated eruptive volume at ~3.9×10^7 m^3 (2.3×10^7 m^3 DRE), subject to inherent uncertainties of 25%–50% (Coombs et al., 2010a).

2.6.2 Estimated PFD parameters for the 1986 and 2006 deposits

2.6.2.1 Testing the approximation of linearity in the geophysical model

To formulate our physical deformation model in Section 4.2, we approximated the true subsidence time series s_n^{92-05}, s_n^{06-07}, and s_n^{07-10} by a linear model of the form $s_n = \Delta s \cdot t_n$, where Δs are their linear subsidence rates. When analyzing the shape of the subsidence time series in Figure 2.6, it can be observed that the subsidence of PFDs indeed appears reasonably linear within each data stack. A chi-squared test was conducted to test if the deformation data in s_n^{92-05}, s_n^{06-07}, and s_n^{07-10} can be sufficiently described by a linear model. This test showed that 90% of the variability in these subsidence time series can be explained by a linear model. Furthermore, it was found that an alternative exponential decay model did not lead to a statistically significant improvement of model fit. Both of these findings indicate that approximating our data by a linear model, as suggested in Section 4.2, does not lead to significant loss of information.

2.6.2.2 Estimating $\bar{\gamma}_{th}$ and $\bar{\gamma}_{pe}$

We use the linear subsidence rates Δs^{92-05}, Δs^{06-07}, and Δs^{07-10} together with estimates for the thermoelastic and poroelastic contraction parameters $\bar{\gamma}_{th}$ and $\bar{\gamma}_{pe}$, respectively. As we assume that the subsidence measurements in the individual pixels are uncorrelated from measurements in other pixels (see Sections 2.4.1 and 2.4.2), this means that the model in Eqs. 2.10 – 2.14 can be executed pixel by pixel, vastly simplifying the computational complexity. While there are true correlations between pixels (related to phase filtering and atmospheric effects), we considered the impact of ignoring these correlations small compared to the impact on computational efficiency.

Before inverting for parameters $\bar{\gamma}_{th}$ and $\bar{\gamma}_{pe}$ we first conducted a test of the geophysical relationships in Eq. 2.8, which imply a linear relationship between surface contraction rate, Δs, and PFD thickness h, with $\bar{\gamma}_{th}$ and $\bar{\gamma}_{pe}$ acting as scaling parameters. To test this assumption, we created a scatterplot between the surface subsidence ($\Delta s^{07-10} - \Delta s^{92-05}$) and thickness $h_{PFD,06}$ of the 2006 PFDs (Figure 2.8). The result showed a strong linear correlation between subsidence rate and PDF thickness ($r^2 = 0.66$), giving credence to the scaling model used in Eqs. 2.8 – 2.10. Similar linear relationships were also found by Ebmeier et al. (2012), who studied deformation of a lava flow deposit at Santiaguito Volcano, Guatemala.

With the assumptions in our geophysical model confirmed, we perform the least-squares estimation of the thermoelastic and poroelastic contraction parameters $\bar{\gamma}_{th}$ and $\bar{\gamma}_{pe}$ using the formalism in Eqs. 2.9 – 2.13. The following results were achieved:

Least Squares Estimates for $\bar{\gamma}_{th}$ and $\bar{\gamma}_{pe}$:

$\bar{\gamma}_{th}$ [cm y^{-1} m^{-1}] = -0.091; sigma = 0.002

$\bar{\gamma}_{pe}$ [cm y^{-1} m^{-1}] = -0.319; sigma = 0.005

Correlation coefficient between parameters = −0.22

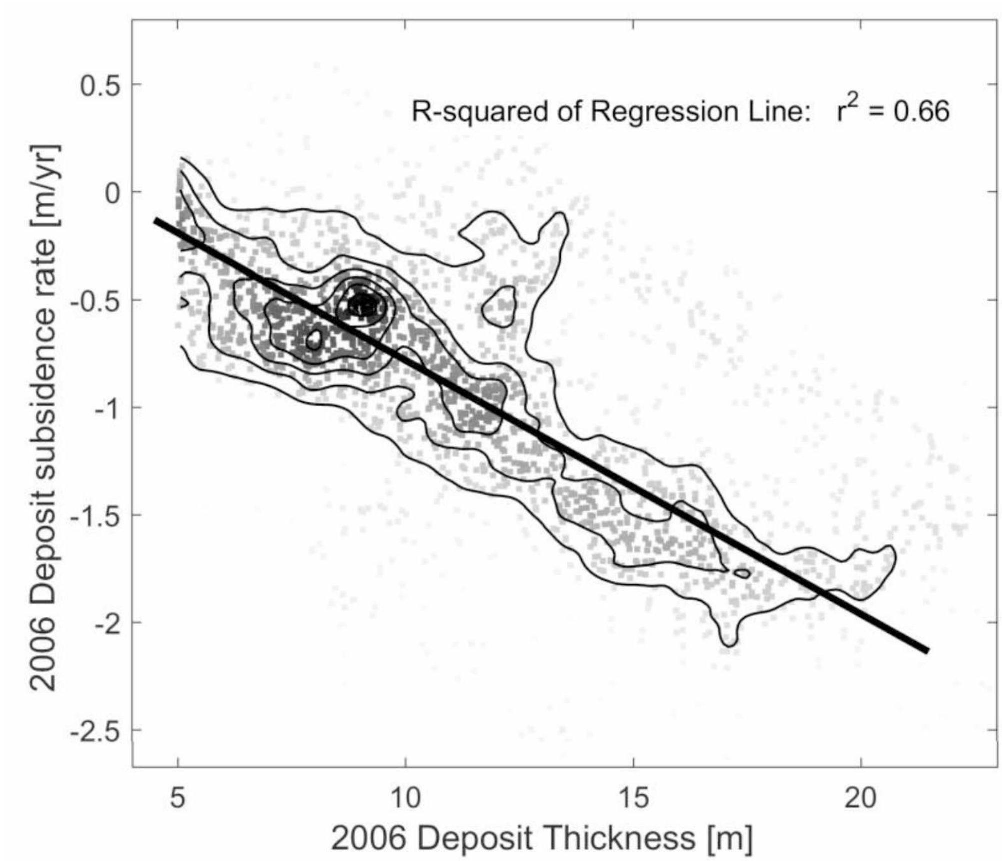

Figure 2.8 A scatter plot of deposit thickness and subsidence rates from the 2006 eruption, shown here with the best-fit linear regression line, validates the assumption of a linear relationship between the two. Density of data points is indicated by isolines (thin black lines) and changes in gray scale shading of points. The data's r^2 value of 0.66 is persuasive evidence the linearity assumption is appropriate

These results indicate that both $\bar{\gamma}_{th}$ and $\bar{\gamma}_{pe}$ could be successfully separated using the proposed approach (small correlation coefficient) with acceptable precision ($\sigma_{\bar{\gamma}_{th}}$ = 0.002 and $\sigma_{\bar{\gamma}_{pe}}$ = 0.005) as shown above. While only relevant for a short time period after the eruption, poroelastic contraction was dominant during the immediate post eruption time. The long term-acting thermoelastic contraction was found to cause subsidence of 0.1 cm y^{-1} m^{-1}. Interestingly, this value is in good agreement with typical contraction parameters for basaltic and andesitic lava flows that were calculated by Ebmeier et al. (2012), from a limited set of global measurements.

This similarity should be studied further for PFDs at other volcanoes with sufficient SAR data coverage.

2.6.2.3 Estimating the thickness of PFDs deposited in 1986

Following the assumption of strong similarities between the compositions of the 1986 and 2006 PFDs (Section 2.3), we conclude that the thermoelastic contraction parameter $\bar{\gamma}_{th}$ (estimated for the 2006 PFDs in Section 2.5.2.2) also applies to deposits emplaced during the 1986 eruption. Consequently $\bar{\gamma}_{th}$ can be used, together with Eq. 2.7, to arrive at first estimates of the thickness, $\hat{h}_{PFD,86}$, of PFDs deposited in 1986.

We apply the general least squares concept in Eqs. 2.14 – 2.15 to calculate both $\hat{h}_{PFD,86}$ and its accuracy properties and achieved the following result:

General Least Squares Estimates for $\hat{h}_{PFD,86}$:

Mean thickness $\mu_{\hat{h}_{PFD,86}}$ [m] = 7.4

Error of thickness estimates $\sigma_{\hat{h}_{PFD,86}}$ [m] = 1.1

Max thickness [m] = 31.5

Total deposition volume [m³] = $4.6 \times 10^7 \pm 0.62 \times 10^7$

A map of the estimated 1986 PFD thickness is shown in Figure 2.7a. At $4.6 \times 10^7 \pm 0.62 \times 10^7$ m^3, we found the total volume of the 1986 PFDs to be about 1.5 times larger than those deposited in 2006. A comparison of the maps in Figure 2.7a,b shows that this difference mainly stems from a higher deposition on the northeastern flank of Augustine during the 1986 eruption. To estimate the average deposition thickness $\mu_{\hat{h}_{PFD,86}}$ we first identified pixels with significant deposition by applying a threshold of $\hat{h}_{PFD,86} < 2 \cdot \sigma_{\hat{h}_{PFD,86}}$ and then calculated the average of $\hat{h}_{PFD,86}$ over these pixels. As the resulting number $\mu_{\hat{h}_{PFD,86}} = 7.4$ m is dependent on the selected threshold, it should be considered as an approximate value only.

By comparison, Swanson and Kienle (1988) estimated the expanded volume of the 1986 PFDs as approximately 5×10^7 m^3 (0.05 km^3), but did not describe how that estimate was determined. They also report that a post-eruption topographic map, prepared from aerial photographs taken on 9 September 1986, indicated that dome elevation had increased by ~26 m between 1976 and the close of the 1986 eruption (consistent with Waitt and Begét's observation, between 1992 and 2003, of a 1986 andesite dome forming a prominent part of the summit area (2009). More recently, a finite element model developed by Masterlark et al., (2006), predicted PFDs with a mean thickness of 9.3 m, a maximum of 126 m, and a volume of 2.1×10^7 m^3 (0.021 km^3); Masterlark et al. (2006), similarly report a total PFD volume of 9.9×10^6 m^3 (~0.01 km^3) estimated by differences in DEMs. A summary of the available values is presented in Table 2.2.

Table 2.2 Comparison of previously determined values for mean thickness, maximum thickness, and volume of PFDs from Augustine's 1986 eruption. Unreported values are shown as n/r.

	This Research	**Swanson and Kienle (1988)**	**Masterlark et al., (2006) Model**	**Masterlarket al., (2006) DEM**
Mean thickness (m)	7.4	n/r	9.3	n/r
Maximum Thickness (m)	31.5	n/r	126	n/r
Volume (m^3)	4.6e7	5e7	2.1e7	9.9e6

Our estimates of thickness and volume for 1986 compare well to the 1986 topographic map and observations reported by Swanson and Kienle (1988), but differ more significantly from the results modeled by Masterlark et al., (2006). Given the observations of dome growth by Swanson and Kienle (1988) and Waitt and Begét (2009), however, it seems fair to attribute differences in maximum thickness, particularly in the area proximal to the summit, to andesitic dome growth rather than PFDs alone. Differences in volume are likely due to uncertainties of the finite element model used by Masterlark, et al., (2006). While these uncertainties are not numerically specified, model runs with different initial parameter settings resulted in PFD volume estimates ranging from 9.9×10^6 m^3 to 5.7×10^7 m^3 encompassing our result.

2.7 Discussion

2.7.1 Limitations of the technique

Thickness and deformation rates were developed from models based on observations and a number of simplifying assumptions. Chief among these is an assumption that Augustine's 1986 and 2006 PFDs were sufficiently similar to allow modeling using the same material parameters. The eruption dynamics and a comparison of whole-rock geochemical composition (Figure 2.3) served as the basis for this general assumption. Although we believe this compositional comparison was sufficient for the stated purpose, it was not intended to be a comprehensive geochemical analysis, which was beyond the scope of this work. Similarly, we broadly considered the principal mechanism of deformation to be thermoelastic contraction (Section 4.2.1). Given the similarity of the two eruptions and eruptive products, we considered it unnecessary to model individual deformation processes such as cooling and degassing, or individual conditions that contribute to that process (porosity, density, pressure, and others). This necessarily involves an additional, implicit assumption that the PFDs from 1986 and 2006 were homogeneous in composition, allowing for uniform rates of deformation. This assumption was made despite field observations that Augustine's 1986 PFDs were comprised of block and ash flow deposits, lithic-rich pumice flow deposits, and lahar deposits (Begét and Limke, 1989), and deposits from 2006 were similar to 1986 in terms of sequence, deposit distributions, and magma compositions (Swanson and Kienle, 1988; Power et al., 2006; Coombs et al., 2010a; Vallance et al., 2010). These observations may indicate the possibility of depositional gradations that refute the assumption of uniform deformation. We, however, believe the relative similarities between the two years' eruption products and their similarly rapid emplacement process validate the uniformity assumption for purposes of this estimation.

To simplify modeling and data interpretation, we approximated the deformation behavior of PFDs at Augustine as a piecewise linear process where an initial (higher) deformation rate describes the deformation during the first months after emplacement and a second rate represents the long-term deformation as a flow. This differs from most other approaches, which often use exponential decay functions to describe the temporal variation of subsidence (Lee et al., 2008). We showed in Section 2.6.2.1 that using exponential functions did not lead to a statistically significant improvement of model fit to the InSAR data. Furthermore, we also found that the parameters of the linear functions could be estimated with higher significance than the parameters of an alternative exponential function. Hence, linear models were considered sufficient for this study.

2.7.2 Scientific significance of extracted PFD information

Deformation behavior of volcanic deposits, although reasonably well understood, is difficult to observe and measure on a first hand, in situ basis. Obtaining data from direct observation of pyroclastic emplacement may be hampered by continuing volcanic activity, remote locations, arduous terrain, and other obstacles. Numerical modeling has proven highly effective in estimating deformation, particularly when geometric data, such as deposit thickness from repeated DEMs, are unavailable (Masterlark et al., 2006). Modeling, however, may require significantly simplifying assumptions, and be valid only for individual field situations (Masterlark, 2003). The results from our study, such as deposit thickness and deformation, can provide an important method to numerical modeling and help increase the reliability and precision of geophysical estimates.

The technique we present offers a means to estimate PFD thickness and deformation rates using InSAR and parameter estimation techniques that reach beyond *a priori* estimates and initial modeling. By decomposing contributions from multiple generations of PFDs, our approach provides a basis to quantify thickness, deformation rates, and volume of recent deposits, while providing some insight into a volcano's past by providing previously inaccessible information about deposits from earlier eruption cycles. More precise and accurate data on the post-emplacement characteristics of PFDs allow geophysical parameters to be more accurately modeled, and improve the body of knowledge available for investigation of volcanic hazards.

2.8 Conclusions

This study combines 16 years of InSAR data from multiple platforms to study the thickness and long-term subsidence behavior of PFDs from Augustine Volcano. Our methodology was applied to examine the subsidence behavior of PFDs from multi-sensor InSAR acquisitions acquired across two eruption cycles. This includes a model used to decompose deformation signals from two generations of superimposed flows. From this model, we are able to present the reconstructed subsidence history for PFDs observed on Augustine Island.

This investigation provides interesting insight into post-emplacement behavior of PFDs and similar eruptive flows. Using empirical observations derived from SAR data, we determined that the initial settling period is usually concluded within a year of emplacement. We were also able to show a decrease of deformation rates over time as cooling rates of the flows subside. The produced results allow us to better understand the behavior and geometry of PFDs by using InSAR. Masterlark et al., has previously demonstrated that thermoelastic deformation is a strong function of PFD thickness (Masterlark et al., 2006), and used finite element modeling and an adaptive mesh algorithm to produce a thickness distribution of PFDs from Augustine's 1986 eruption. Using InSAR data from Augustine's 2006 eruption, our model describes a relationship between the thickness of PFDs, their material properties, deformation rates, and change in temperature that permits estimation of any of these four parameters when the other three are known or similarly estimated. Finally, the model can be extended to underlying PFDs to estimate the effect of deforming materials deposited by prior eruptions.

Author Contributions:

David B. McAlpin and Franz J. Meyer conceived and designed this study, and wrote the paper. Wenyu Gong retrieved and processed SAR data. James E. Begét and Peter W. Webley contributed interpretation and participated in all results. Franz J. Meyer supervised the entire project.

Conflicts of Interest:

The authors declare no conflicts of interest.

2.9 Acknowledgements

This study was funded in part by NASA grant ID: NNX12AQ38G. Much gratitude is extended to Cynthia Gardner of the USGS Cascades Volcano Observatory for providing geochemical data on Augustine Volcano's 1986 eruptive products. ALOS-PALSAR data were provided by JAXA as ALOS high level products, ©JAXA, METI, ALOS-1, PALSAR L1.0 2007–2010. Datasets from ERS-1, ERS-2, RADARSAT-1, and ALOS-PALSAR were retrieved from the Alaska Satellite Facility (ASF) Distributed Active Archive Center (DAAC) 2013–2015, and provided through the NASA Earth Science Data and Information System (ESDIS) project. SRTM data were provided courtesy of the USGS Earth Resources Observation and Science Center (EROS), Sioux Falls, South Dakota.

2.10 Appendix

List of variables used in Section 2, Equations 2.1 – 2.16

Variable	Description
N	The number of acquisition times of SAR images in a time series [$t_0, \ldots t_N$].
$\phi_{i,j}$	The interferometric phase measurement [rad] in each pixel, calculated from the SAR images i and j (i.e., an interferogram).
$\phi_{i,j,defo}$	The contribution of ground deformation to each pixel that occurred between time t_i and t_j.
$\phi_{i,j,topo}$	The topography-related phase component that is proportional to the surface height and the interferometric baseline between acquisition at times t_i and t_j.
$\Delta d_{i,j}$	The surface deformation [m] that occurred between image acquisition times t_i and t_j.
$\phi_{i,j,atm-s}$	Interferometric phase related to changes in the atmospheric stratification between times t_i and t_j.
$\phi_{i,j,atm-t}$	Phase differences from variations in the distribution of atmospheric water vapor at time t_i and t_j.
$\phi_{i,j,orbit}$	The interferometric phase contribution due to errors in the satellite orbits of acquisitions at times t_i and t_j.
$\phi_{i,j,noise}$	Phase noise in a pixel of an interferogram calculated from acquisitions at times t_i and t_j.
h	The SAR-observed surface topography [m].
$\Delta\Phi_{i,j}$	The unwrapped differential interferometric phase of a pixel in SAR images i and j.
d_n	The cumulative surface deformation of PDFs across the time-series $d_0 \ldots d_n$.
r	The sensor-to-target range between a SAR instrument and its ground target.
$B_{i,j,\perp}$	The perpendicular baseline distance between sensor acquisitions i and j.
θ	The look angle of the SAR system.
λ	The wavelength of the transmitted radar signal.
h_{pe}	Topography values obtained from a pre-eruption DEM.
$h_{PFD,06}$	The thickness of 2006 PFDs measured by InSAR.
$B_{n,\perp}$	The perpendicular baseline between the SAR image acquisition at time t_n and the reference image acquisition at time t_0.
$\Delta_{\varphi n}$	The reconstructed phase history at the N+1 image acquisition times.

B_t	The temporal baseline of an InSAR image pair.
$\Delta\varphi_n$	The reconstructed phase history at time step n of the N + 1 image acquisitions.
$\Delta\varphi$	The (N × 1) vector of reconstructed phase history values.
d_n^{92-05} d_n^{06-07} d_n^{07-10}	Deformation time series data estimated for the time periods 1992–2005 (ERS1 and 2), 2006–2007 (Radarsat-1), and 2007–2010 (ALOS PALSAR) (see also $\boldsymbol{s_n^{92-05}}$, et al.).
s_n^{92-05} s_n^{06-07} s_n^{07-10}	Deformation time series data estimated for the time periods 1992–2005 (ERS 1 and 2), 2006–2007 (Radarsat-1), and 2007–2010 (ALOS PALSAR) after projection into a joint vertical reference frame (see d_n^{92-05}, et al.).
Δs_n^{92-05} Δs_n^{06-07} Δs_n^{07-10}	Estimated linear subsidence rates applicable to each of the three time series, $\boldsymbol{s_n^{92-05}}$, s_n^{06-07}, s_n^{07-10}.
Δs	Linear subsidence rate.
$h_{PFD,86}$	The unknown thickness of the 1986 PFDs.
$\bar{\gamma}_{th}$	The average thermoelastic contraction parameter of PFDs for the 2006–2007 period.
$\bar{k}$	The average cooling rate of 2006 PFDs.
$\bar{\gamma}_{pe}$	The average poroelastic contraction parameter of PFDs for the 2006–2007 period.
α_L	The thermal contraction coefficient of the PFDs.
b	The (2·R·C) × 1 column vector of observations in the InSAR data matrix.
$\hat{\varepsilon}$	The (2·R·C) × 1 column vector of estimated residuals.
$\hat{x}$	Generic vector of estimated unknowns in a least-squares inversion framework.
A	Design matrix of a least-squares inversion framework, containing the partial derivatives of a mathematical relationship relative to the unknowns.
P_{bb}	Weight matrix.

Σ_{bb}	The covariance matrix of observations.
δ	The object function to be minimized in a least-squares inversion.
$\Sigma_{\hat{x}\hat{x}}$	The covariance matrix of estimated unknowns $\hat{x}$.
B	A second design matrix of the generalized least-squares model containing the partial derivatives of a mathematical relationship with respect to the observations.

2.11 References

Agram, P.S., Jolivet, R., Riel, B., Lin, Y.N., Simons, M., Hetland, E., Doin, M.-P., and Lasserre, C., 2013, New radar interferometric time series analysis toolbox released: Eos, Transactions, American Geophysical Union, v. 94, p. 69-70, doi: 10.1002/2013EO070001.

Begét, J.E., and Kowalik, Z., 2006, Confirmation and Calibration of Computer Modeling of Tsunamis Produced by Augustine Volcano, Alaska: Science of Tsunami Hazards, v. 24, p. 257.

Begét, J.E., and Limke, A.J., 1989, Density and void ratio on emplacement of a small pyroclastic flow, Mount St. Augustine, Alaska: Journal of Volcanology and Geothermal Research, v. 39, p. 349-353, doi: 10.1016/0377-0273(89)90098-X.

Berardino, P., Fornaro, G., Lanari, R., and Sansosti, E., 2002, A new algorithm for surface deformation monitoring based on small baseline differential SAR interferograms: IEEE Transactions on Geoscience and Remote Sensing, v. 40, p. 2375-2383, doi: 10.1109/TGRS.2002.803792.

Briole, P., Massonnet, D., and Delacourt, C., 1997, Post-eruptive deformation associated with the 1986–87 and 1989 lava flows of Etna detected by radar interferometry: Geophysical Research Letters, v. 24, p. 37-40, doi: 10.1029/96gl03705.

Cas, R.A.F., and Wright, J.V., 1987, Volcanic Successions: London, UK, Allen & Unwin, Ltd., 528 pp.

Cervelli, P.F., Fournier, T., Freymueller, J., and Power, J.A., 2006, Ground deformation associated with the precursory unrest and early phases of the January 2006 eruption of Augustine Volcano, Alaska: Geophysical Research Letters, v. 33, p. L18304, doi: 10.1029/2006gl027219.

Coombs, M.L., Bull, K., Vallance, J.W., Schneider, D., Thoms, E.E., Wessels, R.L., and McGimsey, R., 2010a, Timing, distribution, and volume of proximal products of the 2006 eruption of Augustine Volcano, *in* Power, J.A., Coombs, M.L., and Freymueller, J., eds., The 2006 eruption of Augustine Volcano, Alaska: USGS Professional Paper 1769, p. 145-185.

Coombs, M.L., Bull, K., Vallance, J.W., and Thoms, E.E., 2010b, Geologic map of on-island deposits from the 2006 eruption of Augustine Volcano (Map) - Plate 1: U.S. Geological Survey Professional Paper 1769, scale 1:20000.

Costantini, M., 1998, A novel phase unwrapping method based on network programming: IEEE Transactions on Geoscience and Remote Sensing, v. 36, p. 813-821, doi: 10.1109/36.673674.

Curlander, J.C., and McDonough, R.N., 1991, Synthetic aperture radar: systems and signal processing: New York, NY, USA, John Wiley & Sons, Inc., 645 pp.

Davidson, G., 1884, Notes on the eruption of Mount St. Augustine, Alaska, October 6, 1883: Science, v. 3, p. 186-189.

Ebmeier, S.K., Biggs, J., Mather, T.l., Elliott, J.R., Wadge, G., and Amelung, F., 2012, Measuring large topographic change with InSAR; lava thicknesses, extrusion rate, and subsidence rate at Santiaguito Volcano, Guatemala: Earth and Planetary Science Letters, p. 216-225, doi: 10.1016/j.epsl.2012.04.027.

ESA, 2011, "European Space Agency: Observing the earth", Agency, E.S. (ed.). Last modified 17 August 2011, European Space Agency, http://www.esa.int/Our_Activities/Observing_the_Earth/ERS_overview, accessed 25 September 2014.

Fattahi, H., and Amelung, F., 2013, DEM error correction in InSAR time series: IEEE Transactions on Geoscience and Remote Sensing, v. 51, p. 4249-4259, doi: 10.1109/TGRS.2012.2227761.

Gabriel, A.K., Goldstein, R.M., and Zebker, H.A., 1989, Mapping small elevation changes over large areas: Differential radar interferometry: Journal of Geophysical Research, v. 94, p. 9183-9191, doi: 10.1029/JB094iB07p09183.

Gardner, C., 2016, Unpublished data, USGS Cascades Volcano Observatory, Vancouver, WA, USA.

GNIS, 2007, "USGS Geographic Names Information System", U.S. Geological Survey, Reston , VA, http://geonames.usgs.gov/apex/f?p=136:3:0::NO:3:P3_FID,P3_TITLE:1412986,Nanwalek, accessed 7 September 2016.

Goldstein, R.M., and Werner, C.L., 1998, Radar interferogram filtering for geophysical applications: Geophysical Research Letters, v. 25, p. 4035-4038, doi: 10.1029/1998GL900033.

Gong, W., Meyer, F.J., Lee, C.W., Lu, Z., and Freymueller, J., 2015a, Measurement and interpretation of subtle deformation signals at Unimak Island from 2003 to 2010 using weather model-assisted time series InSAR: Journal of Geophysical Research: Solid Earth, v. 120, p. 1175-1194, doi: 10.1002/2014JB011384.

Gong, W., Meyer, F.J., Liu, S., and Hanssen, R.F., 2015b, Temporal Filtering of InSAR data using statistical parameters from NWP models: IEEE Transactions on Geoscience and Remote Sensing, v. 53, p. 4033-4044, doi: 10.1109/TGRS.2015.2389143.

JAXA, 2011, "Japan Aerospace Exploration Agency press release dated 12 May 2011: DAICHI (ALOS) operation completion", http://www.jaxa.jp/press/2011/05/20110512_daichi_e.html, accessed 7 May 2012.

Kienle, J., Kowalik, Z., and Murty, T.S., 1987, Tsunamis Generated by Eruptions from Mount St. Augustine Volcano, Alaska: Science, v. 236, p. 1442-1447, doi: 10.1126/science.236.4807.1442.

Kienle, J., and Shaw, G.E., 1979, Plume dynamics, thermal energy and long-distance transport of vulcanian eruption clouds from Augustine Volcano, Alaska: Journal of Volcanology and Geothermal Research, v. 6, p. 139-164, doi: 10.1016/0377-0273(79)90051-9.

Lanari, R., Lundgren, P., and Sansosti, E., 1998, Dynamic deformation of Etna Volcano observed by satellite radar interferometry: Geophysical Research Letters, v. 25, p. 1541-1544, doi: 10.1029/98gl00642.

Larsen, J.F., Nye, C.J., Coombs, M.L., Tilman, M., Izbekov, P., and Cameron, C., 2010, Petrology and geochemistry of the 2006 eruption of Augustine Volcano, *in* Power, J.A., Coombs, M.L., and Freymueller, J., eds., The 2006 eruption of Augustine Volcano, Alaska: USGS Professional Paper 1769, p. 335-382.

Lee, C.-W., Lu, Z., Kwoun, O.-I., and Won, J.-S., 2008, Deformation of the Augustine Volcano, Alaska, 1992-2005, measured by ERS and ENVISAT SAR interferometry: Earth, planets and space, v. 60, p. 447-452, doi: 10.1186/bf03352811.

Lee, C.W., Lu, Z., Jung, H.S., Won, J.S., and Dzurisin, D., 2010, Surface deformation of Augustine Volcano, 1992–2005, from multiple-interferogram processing using a refined small baseline subset (SBAS) interferometric synthetic aperture radar (InSAR) approach, *in* Power, J.A., Coombs, M.L., and Freymueller, J.T., eds., The 2006 eruption of Augustine Volcano, Alaska: U.S. Geological Survey Professional Paper 1769, p. 453-465.

Lu, Z., Dzurisin, D., Biggs, J., Wicks, C., Jr., and McNutt, S., 2010, Ground surface deformation patterns, magma supply, and magma storage at Okmok volcano, Alaska, from InSAR analysis: 1. Intereruption deformation, 1997-2008: J. Geophys. Res., v. 115, p. B00B02, doi: 10.1029/2009jb006969.

Lu, Z., Masterlark, T., and Dzurisin, D., 2005, Interferometric synthetic aperture radar study of Okmok volcano, Alaska, 1992:2003: Magma supply dynamics and post-emplacement lava flow deformation: Journal of Geophysical Research, v. 110, p. B02403, doi: 10.1029/2004JB003148.

Lu, Z., Masterlark, T., Wicks, C., Thatcher, W., Dzurisin, D., and Power, J., 2002, Interferometric synthetic aperture radar studies of Alaska volcanoes, presented at the ISPRS Commission I Mid-term Symposium in conjunction with Pecora 15/Land Satellite Information IV Conference, vol. XXXIV, Part 1, Denver, Colorado, USA, 10-15 November 2002, pp., doi: 10.1109/IGARSS.2002.1024984, http://www.isprs.org/proceedings/XXXIV/part1/.

Lu, Z., Wicks, C., Power, J.A., and Dzurisin, D., 2000, Ground deformation associated with the March 1996 earthquake swarm at Akutan volcano, Alaska, revealed by satellite radar interferometry: Journal of Geophysical Research: Solid Earth, v. 105, p. 21483-21495, doi: 10.1029/2000jb900200.

Lu, Z., Wicks Jr, C., Dzurisin, D., Power, J., Thatcher, W., and Masterlark, T., 2003, Interferometric synthetic aperture radar studies of Alaska volcanoes: Earth Observation Magazine, v. 12, p. 9-18.

Massonnet, D., and Feigl, K., 1998, Radar interferometry and its application to changes in the Earth's surfaces: Reviews of Geophysics, v. 36, p. 441-500, doi: 10.1029/97RG03139.

Masterlark, T., 2003, Finite element model predictions of static deformation from dislocation sources in a subduction zone: Sensitivities to homogeneous, isotropic, Poisson-solid, and half-space assumptions: Journal of Geophysical Research: Solid Earth, v. 108, p. 7.1 - 7.17, doi: 10.1029/2002jb002296.

Masterlark, T., and Lu, Z., 2004, Transient volcano deformation sources imaged with interferometric synthetic aperture radar: application to Seguam Island, Alaska: Journal of Geophysical Research: Solid Earth, v. 109, p. B01401, doi: 10.1029/2003jb002568.

Masterlark, T., Lu, Z., and Rykhus, R., 2006, Thickness distribution of a cooling pyroclastic flow deposit on Augustine Volcano, Alaska: Optimization using InSAR, FEMs, and an adaptive mesh algorithm: Journal of Volcanology and Geothermal Research, v. 150, p. 186-201, doi: 10.1016/j.jvolgeores.2005.07.004.

Miller, T.P., McGimsey, R.G., Richter, D.H., Riehle, J.R., Nye, C.J., Yount, M.E., and Dumoulin, J.A., 1998, Catalog of the historically active volcanoes of Alaska: U.S. Geological Survey Open-File Report 98-582, US Department of the Interior, US Geological Survey, 104 pp.

Morena, L.C., James, K.V., and Beck, J., 2004, An introduction to the RADARSAT-2 mission: Canadian Journal of Remote Sensing, v. 30, p. 221-234, doi: 10.5589/m04-004.

Mouginis-Mark, P.J., and Domergue-Schmidt, N., 2000, Acquisition of satellite data for volcano studies, *in* Mouginis-Mark, P.J., Crist, J.A., and Fink, J.H., eds., Remote Sensing of Active Volcanism: Geophysical Monograph Series 116, p. 9-24, doi: 10.1029/GM116p0009.

Neal, C.A., McGimsey, R.G., Dixon, J.P., Manevich, A., and Rybin, A., 2008, 2006 volcanic activity in Alaska, Kamchatka, and the Kurile Islands: summary of events and response of the Alaska Volcano Observatory: US Geological Survey Scientific Investigations Report 2008-5214, 102 pp.

Pauk, B.A., Power, J.A., Lisowski, M., Dzurisin, D., Iwatsubo, E.Y., and Melbourne, T., 2001, Global positioning system (GPS) survey of Augustine Volcano, Alaska, August 3-8, 2000: data processing, geodetic coordinates, and comparison with prior geodetic surveys: US Geological Survey Open-File Report 01-99, US Department of the Interior, US Geological Survey, 20 pp.

Plackett, R.L., 1950, Some theorems in least squares: Biometrika, v. 37, p. 149-157, doi: 10.2307/2332158.

Power, J.A., and Lalla, D.J., 2010, Seismic observations of Augustine Volcano, 1970-2007, *in* Power, J., Coombs, M.L., and Freymueller, J., eds., The 2006 Eruption of Augustine Volcano, Alaska: USGS Professional Paper 1769, p. 3-40.

Power, J.A., Nye, C.J., Coombs, M.L., Wessels, R.L., Cervelli, P.F., Dehn, J., Wallace, K.L., Freymueller, J.T., and Doukas, M.P., 2006, The reawakening of Alaska's Augustine Volcano: Eos Transactions, AGU, v. 87, p. 373-377, doi: 10.1029/2006EO370002.

Riehle, J.R., 1985, A reconnaissance of the major Holocene tephra deposits in the upper Cook Inlet region, Alaska: Journal of Volcanology and Geothermal Research, v. 26, p. 37-74, doi: 10.1016/0377-0273(85)90046-0.

Riehle, J.R., Miller, T.F., and Bailey, R.A., 1995, Cooling, degassing and compaction of rhyolitic ash flow tuffs: a computational model: Bulletin of Volcanology, v. 57, p. 319-336, doi: 10.1007/BF00301291.

Rignot, E.J.M., and van Zyl, J.J., 1993, Change detection techniques for ERS-1 SAR data: IEEE Transactions on Geoscience and Remote Sensing, v. 31, p. 896-906, doi: 10.1109/36.239913.

Rodriguez, E., Morris, C.S., Belz, J., Chapin, E., Martin, J., Daffer, W., and Hensley, S., 2005, An assessment of the SRTM topographic products: Technical Report JPL D-31639, Jet Propulsion Laboratory, Pasadena, California, USA, 143 pp., http://www2.jpl.nasa.gov/srtm/SRTM_D31639.pdf.

Rosen, P., Hensley, S., Zebker, H., Webb, F., and Fielding, E., 1996, Surface deformation and coherence measurements of Kilauea Volcano, Hawaii, from SIR-C radar interferometry: Journal of Geophysical Research: Planets (1991–2012), v. 101, p. 23109-23125, doi: 10.1029/96JE01459.

Rosen, P.A., Hensley, S., Joughin, I.R., Li, F.K., Madsen, S.N., Rodriguez, E., and Goldstein, R.M., 2000, Synthetic aperture radar interferometry: Proceedings of the IEEE, v. 88, p. 333-382, doi: 10.1109/5.838084.

Rosenqvist, A., Shimada, M., Ito, N., and Watanabe, M., 2007, ALOS PALSAR: A pathfinder mission for global-scale monitoring of the environment: IEEE Transactions on Geoscience and Remote Sensing, v. 45, p. 3307-3316, doi: 10.1109/TGRS.2007.901027.

Rowley, P.D., Kuntz, M.A., and Macleod, N.S., 1981, Pyroclastic-flow deposits, *in* Lipman, P.W., and Mullineaux, D.R., eds., The 1980 eruptions of Mount St. Helens: U.S. Geological Survey Professional Paper 1250, p. 489-512.

Schmincke, H.-U., 2004, Volcanism: New York, NY, USA, Springer-Verlag, 324 pp.

Sheridan, M.F., and Ragan, D.M., 1975, Compaction of ash-flow tuffs: Developments in Sedimentology, v. 18, p. 677-717, doi: 10.1016/S0070-4571(08)71103-8.

Siebert, L., Glicken, H., and Kienle, J., 1989, Debris avalanches and lateral blasts at Mount St. Augustine Volcano, Alaska: National Geographic Research, v. 5, p. 232-249.

Stevens, N.F., Wadge, G., Williams, C.A., Morley, J.G., Muller, J.P., Murray, J.B., and Upton, M., 2001, Surface movements of emplaced lava flows measured by synthetic aperture radar interferometry: Journal of Geophysical Research: Solid Earth, v. 106, p. 11293-11313, doi: 10.1029/2000jb900425.

Swanson, S.E., and Kienle, J., 1988, The 1986 eruption of Mount St. Augustine: field test of a hazard evaluation: J. Geophys. Res., v. 93, p. 4500-4520, doi: 10.1029/JB093iB05p04500.

Vallance, J.W., Bull, K., and Coombs, M.L., 2010, Pyroclastic flows, lahars, and mixed avalanches generated during the 2006 eruption of Augustine Volcano, *in* Power, J., Coombs, M.L., and Freymueller, J., eds., The 2006 Eruption of Augustine Volcano, Alaska: U.S.Geological Survey Professional Paper 1769, p. 219-267.

van Zyl, J.J., 2001, The Shuttle Radar Topography Mission (SRTM): a breakthrough in remote sensing of topography: Acta Astronautica, v. 48, p. 559-565, doi: 10.1016/S0094-5765(01)00020-0.

Waitt, R.B., and Begét, J., 2009, Volcanic processes and geology of Augustine Volcano, Alaska: U.S. Geological Survey Professional Paper 1762, 78 pp., 2 plates, scale 1:25,000.

Waitt, R.B., McIntire, J., and Janda, C.G., 2009, Geologic map of Augustine Island, Alaska - Plate 1: US Geological Survey Professional Paper 1762, scale 1:25000.

Williams, H., and McBirney, A.R., 1979, Volcanology: San Francisco, CA, USA, Freeman, Cooper & Co., 397 pp.

Yount, M.E., Miller, T.P., and Gamble, B.M., 1987, The 1986 eruptions of Augustine Volcano, Alaska: hazards and effects, *in* Hamilton, T.D., and Galloway, J.P., eds., Geologic Studies in Alaska in 1986: U.S. Geological Survey Circular 998, p. 4-13.

Zebker, H.A., Amelung, F., and Jonsson, S., 2000, Remote sensing of volcano surface and internal processes using radar interferometry, *in* Mouginis-Mark, P.J., Crisp, J.A., and Fink, J.A., eds., Remote Sensing of Active Volcanism: Geophysical Monograph Series 116, p. 179-205, doi: 10.1029/GM116p0179.

Zielinki, S., 2006, Explosion at dormant Alaskan volcano: Eos, Transactions American Geophysical Union, v. 87, p. 435-435, doi: 10.1029/2006eo410008.

Chapter 3

Multi-sensor remote sensing data applied to estimation of 2012–2013 effusion rates at Tolbachik Volcano, Kamchatka Peninsula, Russian Far East[3]

3.1 Abstract

Measuring the emplacement volume and deposition rates at effusive volcanoes is a key element of understanding their behavior and, where possible, assessing their hazard potential. This study was conducted to evaluate how thermal satellite data from the constellation of National Oceanic and Atmospheric Administration satellites carrying Advanced Very High Resolution Radiometers can be combined with synthetic aperture radar data from the German Aerospace Center's TanDEM-X synthetic aperture radar mission to derive detailed deposition data from the 2012–2013 effusive Tolbachik Fissure Eruption on the Kamchatka Peninsula, Russian Far East. The fusion of Advanced Very High Resolution Radiometer thermal data and TanDEM-X synthetic aperture radar data was accomplished through coregistration, resampling, comparison, and interpolating the high temporal resolution Advanced Very High Resolution Radiometer data with the much more infrequent digital elevation models developed from TanDEM-X data of high spatial resolution. This new approach for combining the temporally, spatially, and spectrally different datasets is presented here along with a discussion on the benefits and limitations of the technique. This process has developed an eruption profile with more reliable estimates of the volume of deposition and rates of emplacement over the course of the eruption. This combined analysis is a significant improvement over the single point estimates

[3] McAlpin, D.B., Meyer, F.J., Kubanek, J., Webley, P.W., and Dehn, J., Multi-sensor remote sensing data applied to estimation of 2012–2013 effusion rates at Tolbachik Volcano, Kamchatka Peninsula, Russian Far East, prepared for submission to the Journal of Volcanology and Geothermal Research.

using the low temporal resolution of the TanDEM-X data alone where non-varying rates are assumed between observations. As part of this study, the progression of the Tolbachik Fissure Eruption at a high temporal resolution was possible, and we clarified the onset and end of the eruptive period, as well as periods of higher and lower effusive activity. This combined thermal-SAR approach has the potential to develop more comprehensive analyses of effusive volcanic depositional episodes, improve hazard mitigation efforts, and increase our understanding of subsurface conditions that control effusive eruptions.

3.2 Introduction:

Tolbachik Volcano (55° 49.5'N, 160° 23.5' E) is located on the ~1200 km long Kamchatka Peninsula in the far-eastern end of the Russian Federation (Figure 3.1). The peninsula is flanked on the west by the Sea of Okhotsk, in the southeast by the Pacific Ocean, and in the northeast by the Bering Sea. Tolbachik Volcano, or more precisely the Tolbachik Volcanic Complex, consists of two stratovolcanoes: the Ostry (sharp) Tolbachik, and Plosky (flat) Tolbachik (Zelenski et al., 2014). Although Ostry Tolbachik is inactive (Fedotov et al., 2011), Plosky Tolbachik is one of the largest and most active volcanic areas on the Kamchatka Peninsula (Churikova et al., 2015), and marks the southern end of the Klyuchevskoy Volcano Group (KVG), that includes 14 active and inactive volcanoes (Senyukov et al., 2015).

Within the last fifty years, Plosky Tolbachik (hereafter, "Tolbachik" refers to Plosky Tolbachik unless otherwise specified), has had two large effusive eruptions; the first in 1975–1976, and a second in 2012–2013. The 1975–1976 eruption, the "Great Tolbachik Fissure Eruption," lasted more than 1½ years, and emplaced ~2.2 km^3 of volcanic product over an area exceeding 1000 km^2 (Churikova et al., 2015) and was the largest basaltic eruption in the Kurile-Kamchatka volcanic belt in historic time (Fedotov et al., 1980).

The 2012–2013 eruption, also known as the "Tolbachik Fissure Eruption" (TFE), occurred over nine months, from 27 November 2012 through 24 August 2013 and deposited volcanic products over a reported area between 35.9 km^2 and 45.8 km^2, with a non-DRE (dense rock equivalent) volume variously estimated between 0.53 km^3 and 0.65 km^3 (0.50 km^3 DRE and 0.55 km^3 DRE). (Dvigalo et al., 2014; Belousov et al., 2015; Dai and Howat, 2017; Kubanek et al., 2017). The eruption was largely an effusive eruption, which is broadly defined by Jackson (1997) as the emission of relatively fluid lava onto the Earth's surface, and by Harris et al. (2007), as volume flux pertinent to basaltic lava flows.

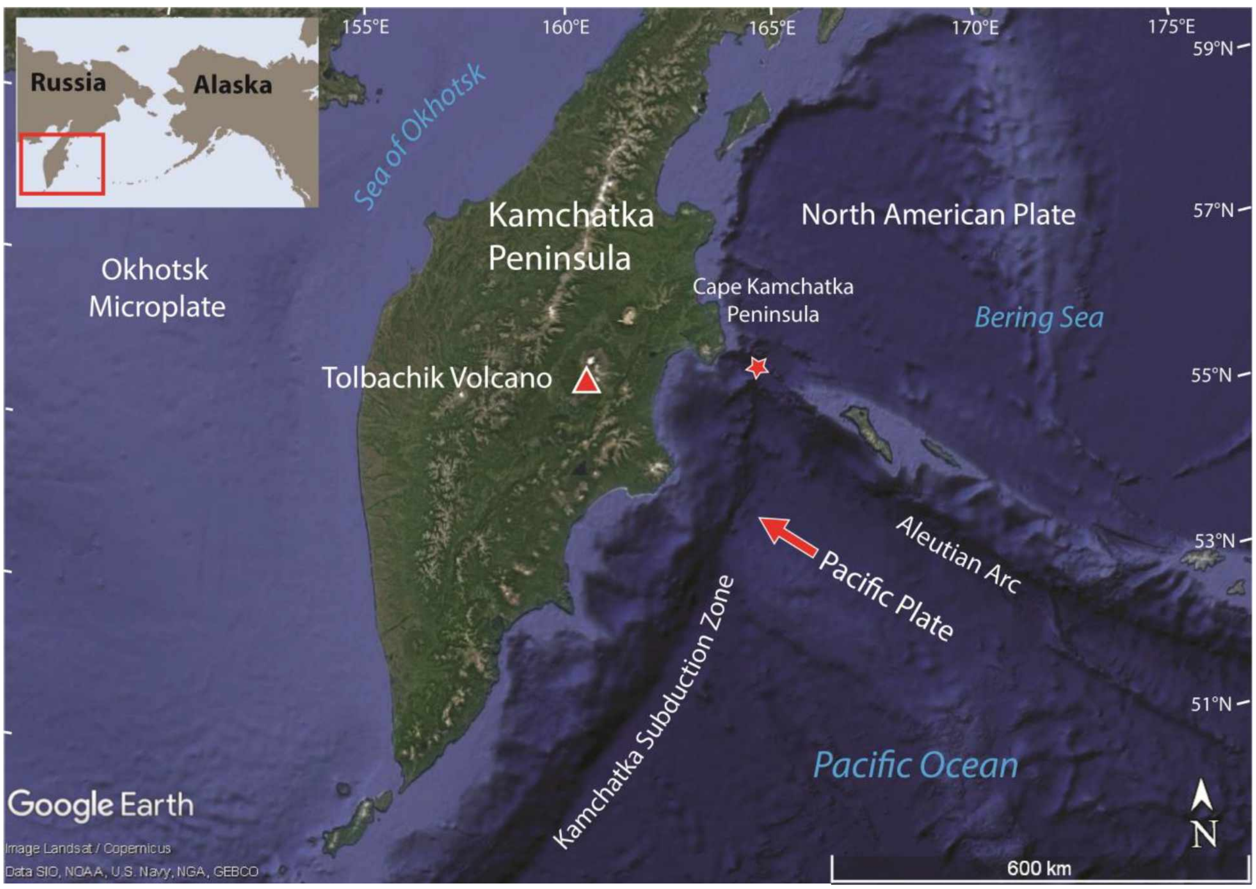

Figure 3.1: The Kamchatka Peninsula in the Russian Far East. Tolbachik Volcano is shown in the Central Kamchatka Depression, formed between the Kamchatka Mountain Range to its west, and the Vostochny Range to its Southeast. The large red arrow indicates the approximate direction of Pacific Plate subduction under the peninsula (Jiang, 2009); a star marks the vicinity of the Aleutian-Kamchatka Junction where the subducting Pacific Plate terminates (Levin, 2002).

Volcanism of the KVG is driven by the Pacific Plate lithosphere subducting under the Kamchatka Peninsula and the Okhotsk microplate at ~7.7 cm·yr^{-1} at latitude 55°N, and ~8.3 cm·yr^{-1} further south, at 47°N (Jiang et al., 2009). The northern end of the Pacific Plate terminates in an unusual confluence with the western end of a second arc-trench system, the Aleutian Subduction Zone (Levin et al., 2002) . This Aleutian-Kamchatka Junction is found in a complex shear zone just off the Cape Kamchatka Peninsula.

The subduction has produced robust volcanism over the entire Kamchatka region, but especially so at Tolbachik, with eruptions in 1941, the Great Tolbachik Fissure Eruption of 1975–1976, and most recently, the Tolbachik Fissure Eruption of 2012–2013. The latter – the subject of this study – began on 27 November 2012, after minor precursory seismicity. The initial eruption began with a south-southwest trending fissure opening on the southern slope of Tolbachik, that became a 6 km long opening, accompanied by intense lava effusion (Melnikov and Volynets, 2015). Although the eruption was primarily effusive, explosive activity was also apparent at numerous vents along the length of the fissure. Most active was the middle part of the fissure, at the Menyailov group of vents, and the lower part of the fissure, the Naboko vents (Belousov et al., 2015) (Figure 3.2).

By the next day (28 November 2012), lava was effusing from these two eruptive centers, forming lava fields exceeding 14 km², and producing lava fountains visible from more than 40 km distant (Gordeev et al., 2013). Large a'a' flows were observable in two streams, the first designated the Vodopadnoye Flow, largely fed by the Menyailov group of vents, and the second, the Leningradskoye flow, fed mostly by the Naboko group (Belousov et al., 2015). Over these first two days, moderate explosive activity and extensive effusion marked the most violent period of the entire eruption, producing a time averaged lava effusion rate estimated by aerial photogrammetry at 440 m³ s^{-1} (Dvigalo et al., 2014).

From 29 November 2012 explosive activity and effusion continued at both the Menyailov and Naboko vents through 30 November 2012, but in early December 2012, activity along the middle to upper parts of the fissure, including the Menyailov vents, waned and ceased. The front of the Vodopadnoye Flow Field, which was fed by the middle to upper vents, stopped its westward advance at a length of 8.5 km, and a thickness of 10 m. The lower level Naboko vents persisted, however, and continued to feed the Leningradskoye Flow Field, whose westerly extent

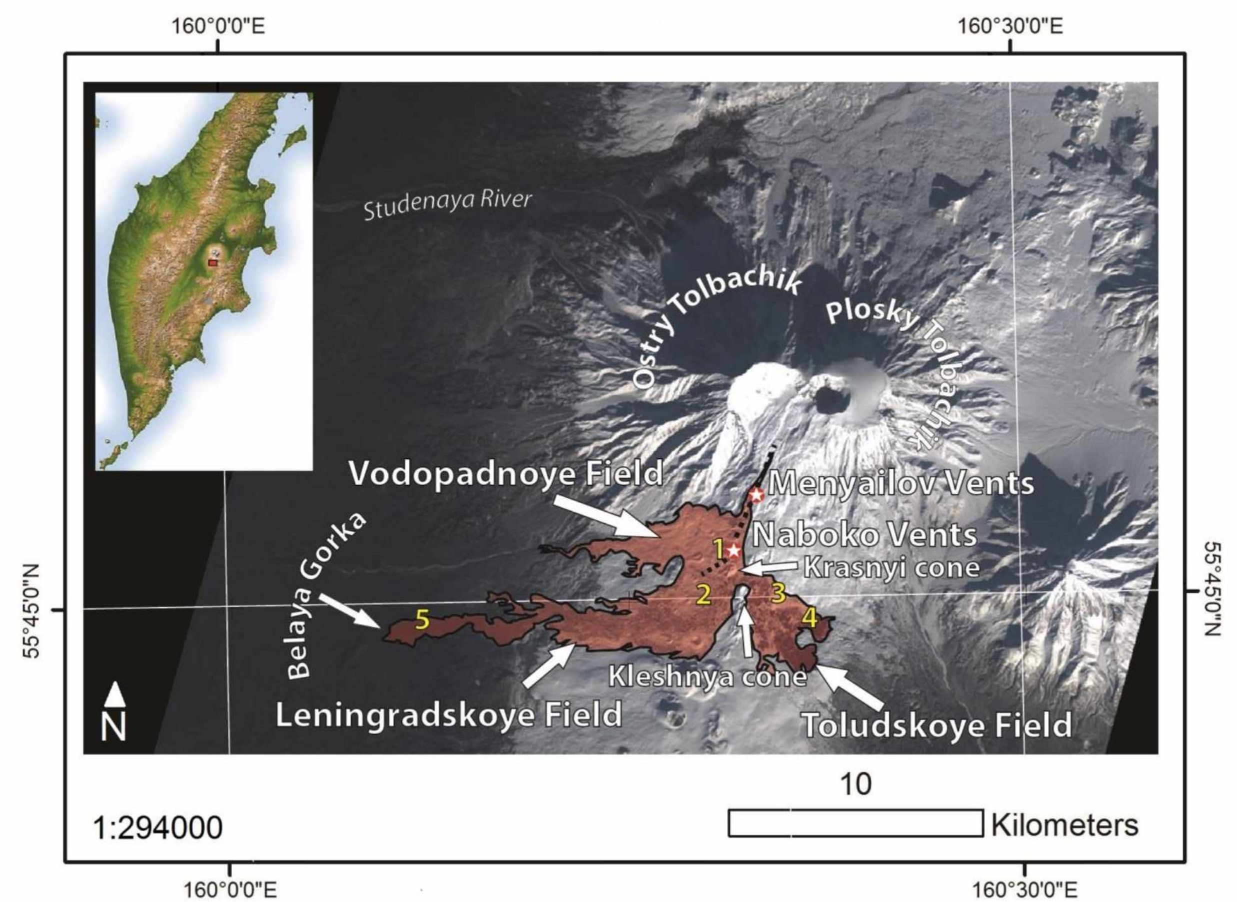

Figure 3.2: Tolbachik Volcano, including flow fields and major vents from the TFE. The eruptive fissure, center, is displayed as a dashed line, with major vents marked by red/white stars along the fissure. Yellow numbers correspond to sample points described in Section 3.4.1.2. The flow field outline is modified from Belousov (2015). Inset map from Shuttle Radar Topography Mission (SRTM), courtesy NASA/JPL. Background image from EO-1/ALI image, courtesy USGS.

was reported to have reached its maximum length of 17.8 km on or before 13 December 2012 (Dvigalo et al., 2014; Belousov et al., 2015).

The roughly two week period that ended 8 December marked the end of the TFE's initial eruptive stage and the beginning of the main stage of the eruption, as designated by Belousov et al. (2015). In January, 2013, lava lobes began migrating towards the south, southeast, and east, forming a third lava field, known as the Toludskoye Flow Field. By early June 2013, the Vodopadnoye Field was up to ~10 m thick, while the Leningradskoye Lava Field, formed by a number of overlying flows, reached a thickness of up to ~69 m between Krasnyi and Kleshnya Cones, but 5–15 m near Belaya Gorka. The Toludskoye Flow would continue to grow until the end of the main stage in late August 2013, reaching ~53 m thickness to the east of the Kleshnya Cone (Dvigalo et al., 2014), and up to ~70 m thick in its northern areas (Belousov et al., 2015).

The final stage of the eruption began on 23 August 2013, when lava discharge decreased to zero, and lava, flowing through a system of lava tubes, ceased. At the same time, seismic tremors decreased below detection levels, and lava drained from the lava ponds in the main crater and satellite vents of the Naboko cone. Minor Strombolian activity and subsidence episodes continued for approximately two weeks, before a complete cessation of surface activity during the first week of September, 2013 (Belousov et al., 2015). No substantial increase in area was reported in the Toludskoye Flow since early June 2013, although some thickening continued between June 2013, and the cessation of effusion at the end of August, 2013.

This highly active volcanic zone is of geologic interest due to its frequency and intensity, but also of economic interest given the potential for eastward drifting ash to disrupt air traffic in the busy transportation corridor between North America and the Far East. Consequently, the Alaska Volcano Observatory (AVO) has closely monitored the region for volcanic activity. From 1993 to 2018, AVO maintained extensive observations of the Kamchatka Peninsula using the Advanced Very High Resolution Radiometers (AVHRR) aboard a constellation of sun-synchronous, Polar Orbiting Environmental Satellites (POES), and its predecessor platform, the Advanced TIROS-N (ATN), both operated by NOAA.

This study examines more than nine-months of AVHRR thermal data collected by three POES satellites during the TFE, focusing on observed activity, with comparison and enhancement of complementary data from the TanDEM-X radar mission consisting of two synthetic aperture radar sensors operated by the German Aerospace Center, Deutches Zentrum für Luft und Raumfahrt (DLR), and its partner, Astrium GmbH.

3.2.1 The AVHRR thermal sensor

The first AVHRR sensor was a four-channel radiometer, launched in 1978, followed by an improved, five-channel version, AVHRR/2, in 1981 (Kidwell, 1991). All currently operating AVHRR sensors (AVHRR/3) operate in six-channels, observing in both visual and infrared wavelengths (NOAA, 2017) (Table 3.1).

Table 3.1: Six visible and infrared (IR) wavelengths of AVHRR/3 along with spatial resolution at nadir (Robel and Graumann, 2014).

Band	Spectrum	Wavelength (μm)	Spatial resolution at nadir (km)
1	Visible	0.580 – 0.680	1.1
2	Near IR	0.725 – 1.000	1.1
3A	Near IR (daylight)	1.580 – 1.640	1.1
3B	Mid-IR (night)	3.550 – 3.930	1.1
4	Thermal IR	10.300 – 11.300	1.1
5	Thermal IR	11.500 – 12.500	1.1

AVHRR/3 channels l, 2, and 3A measure reflected energy in the visible and near-IR portions of the electromagnetic spectrum, providing observations of land surface, vegetation, clouds, lakes, shorelines, snow, aerosols, and ice. Channels 3B, 4, and 5 are used to determine the radiative energy in the mid- and thermal IR from the temperature of the land, water, and sea surface as well as the clouds above them (Robel and Graumann, 2014). With their global coverage and 12-hour revisit cycles, two operational AVHRR sensors can provide up to four daily surface observations of almost any target on earth. The trade-off for frequency of observations, however, is a coarse spatial resolution; where the AVHRR ground resolution is only 1.1 km at nadir, and increases to 7.2 km at the edge of its swath (Harris, 2013).

Melnikov and Volynets (2015) summarized their opinion by stating, "This kind of resolution is not suitable for analyses of TFE lava flows." Nonetheless, the frequency of AVHRR observations creates an extensive archive of surface observations in three infrared channels. Especially when applied to effusive eruptions of long duration like the 2012–2013 TFE, the archive has a high potential to contribute to our understanding of the mechanics and behavior of large effusive eruptions.

3.2.2 Hot and cold components within AVHRR resolution cells

Although AVHRR is onboard a weather-focused satellite that was never designed to detect or monitor high temperature surface features (e.g., fires, lava flows, lava lakes, and fumarole fields), its ability to fulfill this function has been well established since the 1970's (Williams Jr. and Friedman, 1970; Dozier, 1981; Rothery, 1992; Harris et al., 1997b; Oppenheimer, 1998; Dehn et al., 2000; Harris, 2013; Dehn and Harris, 2015; Ramsey, 2016). More difficult, however, is the ability of AVHRR to provide observations that identify the nature of a high temperature feature; to distinguish, for instance, between a lava flow and fumarole field, or another thermally radiant feature (Rothery et al., 1988; Oppenheimer et al., 1993). Moreover, a high temperature feature may represent only a small fraction (0.1% or less) of the spatial footprint of the resolution cell with the reminder filled by a much larger area of cooler crust, or non-radiant background (Oppenheimer, 1991). In such cases, the radiant brightness temperature measurement from

AVHRR reflects a mixed or integrated temperature from multiple components, each occupying an unknown area within the sensor's resolution cell.

Dozier (1980, 1981), addressed the mixed temperature problem with a method of using two infrared bands to estimate the proportionate radiance contribution made by a hot, sub-pixel target and the cooler background portion of the pixel it occupies. This dual-band method was quickly applied to estimate the size and temperatures from steel mills and oil gas flares (Matson and Dozier, 1981), and, though AVHRR was used to observe sub-pixel volcanic targets shortly thereafter (Wiesnet and D'Aguanno, 1982), the dual band method was first applied to volcanic targets by Rothery et al. (1988), using thermal data from the Landsat Thematic Mapper (TM) and Multispectral Scanner (MSS).

Although the dual-band method is a simple means to solve ideal two-component temperature models of lava bodies, it suffers under the assumption that a high-temperature pixel contains only two components (the high temperature component and its cooler, surrounding crust. Oppenheimer (1991), went further, and proposed a three-component model to represent an incandescent exposed core, a cooler crust, and a third, lava-free component of cold surrounding ground. Oppenheimer's approach used Matson and Dozier's dual band equations with an assumed value for the high temperature component, and solved for the fractional component in an iterative process. This proved insightful, because larger ground resolution (1.1 km for AVHRR versus 30 m for Landsat TM) naturally results in a greater number of thermal components.

Oppenheimer's two-band, three-component model was refined with AVHRR data (Harris et al., 1997a) as well as Landsat TM (Harris et al., 1998), and a three-band, three-component model, also with Landsat TM (Harris et al., 1999). Wright and Flynn (2003) suggested that the three component temperature resolution was insufficient to develop a temperature range, even as it was generally effective for the mode. Using a forward-looking infrared (FLIR) thermal camera to examine active lava flows at Kilauea Volcano, Hawai'i, they tested dual- and triple-component models, as well as additional multiple component solutions. Their results concluded that a five- to seven-component solution provided the most complete and accurate description of the actual subpixel temperature distribution.

3.2.3 Obstacles of thermal remote sensing

Regardless of how the mixed temperature problem is approached, issues still remain with un-mixing the sub-pixel temperature distribution, especially with the coarse spatial resolution of AVHRR. Chief among these issues are the effects of sensor saturation, shallow scan angles, and cloud cover.

All thermal sensors have a saturation point; a maximum sensitivity level beyond which an increase in radiance no longer registers. At this level, only the maximum radiance is reported, but nothing greater (Prata et al., 1995). For most meteorological satellites, including AVHRR, saturation levels in the mid-IR and thermal-IR are typically quite low – generally around 50 °C to 65 °C. Actual saturation levels, however, are not strictly a function of hardware. Occasional changes in calibration, sensor degradation, solar contamination, and other causes, create variations in saturation levels (Trischenko et al., 2002). In the past, AVHRR's near-IR channel (band 3), the band most sensitive to high-temperature detection (Kennedy et al., 1994), was reported to saturate at 50 °C (e.g., Dean et al., 1998), 49.5 °C (e.g., Dehn et al., 2000), 56.85 °C (e.g., van Manen et al., 2010a), and 62 °C (e.g., Harris, 2013). The upper bound of band 3 radiant temperatures observed during this study of the nine month TFE was 66.2 °C, but a working value of 62 °C was treated as band 3 saturation.

Saturation occurs at such a low radiant temperature because only a small fraction of a pixel need be occupied by hot material; a lava flow covered by a cool, 100 °C crust occupying a ground area of 0.5 km × 0.5 km, if centered in a pixel at nadir, is sufficient to result in mid-IR, channel 3 saturation (Harris et al., 1995). When AVHRR data is collected over a large, active, lava flow, a significant number of saturated, band-3 pixels may be observed. For those pixels that do saturate, the source temperature of the combined thermal components within the pixel is greater than, or equal to, the saturation temperature of the sensor (Harris, 2013).

AVHRR can be similarly affected by cloud cover, including smoke and ash clouds, which block ground radiance from reaching the sensor. Although thick clouds can be masked out with relative ease (e.g., Tapakis and Charalambides, 2013), they may also leave targets obscured for days or weeks at a time, and in so doing, leave large gaps in AVHRR's otherwise extensive data record. Even when clouds only partially obscure a target, the measured radiant temperature can be significantly biased (e.g., Stewart, 1985; Prata et al., 1995). A more difficult detection problem involving clouds comes from those areas of very thin clouds and haze, or clouds smaller than the sensor's resolution cell. These clouds, usually high cirrus clouds and some low stratus clouds are much colder than the surface. Cirrus clouds, in particular, are much colder, and even a small number can contribute significant errors. Both can be thin enough to be invisible in visible and infrared images, and therefore may remain undetected (Stewart, 1985).

Finally, the satellite's orientation requires attention to determine the geometry of the resolution cell and its effect on spatial resolution. The scan angle is the angle between the satellite nadir and the satellite's view vector of the ground feature. Although the nominal diameter of AVHRR's ground resolution cell is stated as 1.1 km, this assumes measurement at nadir. As the sensor's view vector moves outward from nadir, the size of its ground resolution cell increases in the cross-track direction as shown in Figure 3.3. This becomes particularly important for thermal observations, where accurate temperatures are required, and where resolution cells with multiple thermal components account for the cells' change in size as they approach the scan edge. The nominal AVHRR ground resolution cell covers an area of 1.1 km × 1.1 km at nadir, but increases to approximately 7.2 km × 2.5 km at the edge of the swath (Harris (2013).

3.2.4 Thermal data for effusive deposition volume measurements

Despite these obstacles, thermal data has been successfully used to detect and monitor volcanic activity, and to estimate instantaneous effusion rates at effusive volcanic eruptions. To accomplish the latter, most researchers follow the concept of Pieri and Baloga (1986), who used Hawai'ian lava temperatures collected from field data to establish quantitative relationships between conditions at a volcanic vent, and the morphology of its related lava flow. Harris et al. (1997a) used AVHRR data and a three-component model to estimate the unmixed pixel temperatures and the corresponding hot/warm/cold areas, then applied heat transfer equations to obtain a detailed effusion rate, E_r. In that equation:

$$E_r = Q_{tot} \ / \rho(C_p \Delta T + c_L \Delta\phi) \tag{3.1}$$

where Q_{tot} is the total thermal flux from the flow, ρ and C_p are lava density and specific heat capacity, ΔT is eruption temperature minus solidus, c_L is latent heat of crystallization, and $\Delta\phi$ is crystallization in cooling through ΔT. This is essentially a force balance of the thermal output of the flow, Q_{tot}, divided by the thermal properties of the flow. The same heat transfer method was used by Harris et al. (1998) on active lava flows at Kilauea Volcano from Landsat Thematic Mapper (TM), and AHVRR data; and Harris et al. (2000) used data from three thermal radiometers, AVHRR, TM, and the Along Track Scanning Radiometer (ATSR) to estimate effusion rates at Etna (1980-1995), and Krafla (1975–1984).

Thermal data from AHVRR has also been used to estimate time-averaged effusion rates as a function of lava flow areas. Wright et al. (2001) derived a method using the single-band model of Harris et al. (1997), for occasions when widespread saturation was present in AVHRR band 3. Under those conditions, a range of lava temperatures were assumed, and the fraction of a pixel occupied by hot lava was calculated. Eq. 3-1 for E_r, was modified to reflect heat loss per unit area (F_T), and to account for the area of lava at temperature T (A_T), which became:

$$E_\mathrm{r} = F_T \; / \rho(C_\mathrm{p}\,\Delta T + c_\mathrm{L}\Delta\phi)\,A_T \qquad (3.2)$$

Since the terms that relate E_r and A_T are all constants, Wright et al. (2001) concluded that any variation in E_r must be proportional to changes in the lava flow areas that were calculated or observed, i.e., the equation can be represented as $E_r = xA_T$, where x is the thermally derived coefficient (Lautze et al., 2004).

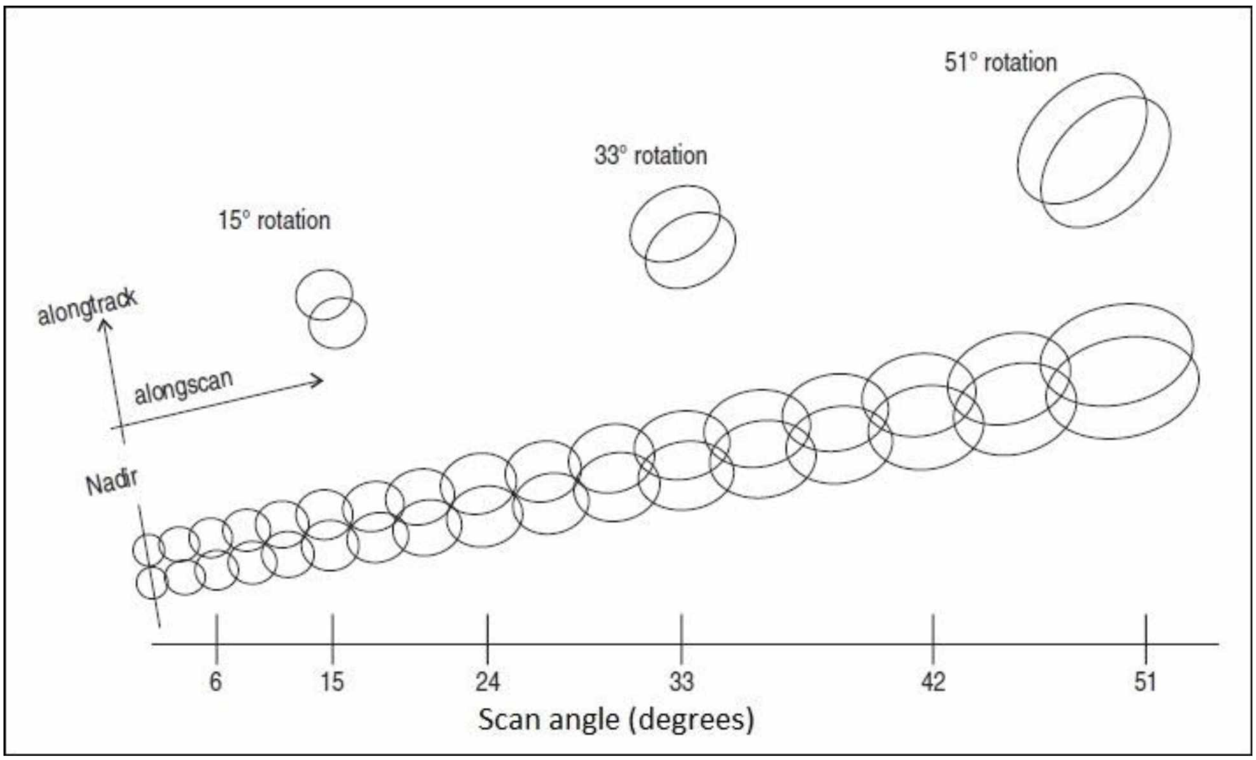

Figure 3.3: Sketch of pixel geometry for two adjacent AVHRR scan lines. The size of a ground resolution cell increases toward the scan edge, as the distance from the sensor to the target increases. This causes a scale distortion that requires adjustment (modified from Harris, 2013).

These studies of volcanic activity proved the utility of satellite observation of volcanoes, particularly those using the high temporal resolution of AVHRR. These studies also helped underscore the feasibility of an automated monitoring approach that could quickly detect the elevated surface temperatures associated with volcanic activity or pre-activity. Among a number of solutions developed for automated volcano monitoring was the Okmok algorithm, established at AVO, and implemented during the 1997 eruption of its namesake, Okmok Volcano, in the Aleutian Islands (Dean et al., 1998; Dehn et al., 2000; Schneider et al., 2000; Dean et al., 2002).

Several times daily, AVHRR data are downloaded to one of two satellite receiving stations at the University of Alaska Fairbanks (UAF), where they are scanned, orthocorrected, and georegistered (Dean et al., 1998). The data are processed by the Okmok algorithm and its successor, Okmok II, to identify potentially elevated surface temperatures, or thermal anomalies. An anomalous pixel can be reliably detected if its AVHRR band 3 temperature is at least 5 °C above its surrounding eight pixels (Dehn et al., 2002; van Manen et al., 2010b).

Once a potential thermal anomaly is identified, the algorithm employs a Bayesian approach to examine the anomalous pixel with a series of tests, including many that are specific to individual North Pacific volcanoes. These tests then assign credits and demerits designed to maximize the likelihood of a volcanic source, and minimize the likelihood of a false positive (Dehn and Harris, 2015). Thermal anomalies in the North Pacific were manually checked at least daily until early 2013, when scheduled satellite monitoring of volcanoes on the Kamchatka Peninsula and the Northern Kurile Islands was discontinued by AVO (scheduled monitoring was continued until 2018 by the research organization V-ADAPT, Inc., and, at this writing is now performed by the Kamchatka Volcanic Eruption Response Team) (KVERT, 2019).

3.2.5 Alternatives to thermal remote sensing: SAR

Remote sensing of volcanic activity is a key element of Earth observation, but there is a need to resist solutions to understand the volcanic process from a single set of observations, or from one type of observations. Although the coverage available from thermal data, often gathered by weather-focused satellites, has become almost ubiquitous given the number of satellites and frequency of observations, its ultimate benefit for the volcano community is often diminished by low spatial resolution, sensor saturation, weather conditions, and/or environmental distortions such as atmospheric emissivity, surface emissivity, and surface reflectivity (Harris et al., 1997a; Harris et al., 2007).

Where thermal observations fall short, radar data often succeeds. Most significantly, radar systems operate in much longer wavelengths than thermal systems; generally within a range from 2.5 cm to 30 cm (Table 3.2). A microwave, or radar wavelength at 5.6 cm (C-band) is 10^5 times as long as visible wavelengths, and ~112 times as long as near-IR wavelengths. Because of these longer wavelengths, radar signals are not generally blocked by clouds, dust, or ash (Ferretti, 2014).

Table 3.2: Frequencies and wavelengths used by selected Earth observation satellites with microwave sensors; Currently operational sensors are marked (*). Modified from Ferretti (2014)

Band	Frequencies	Wavelengths	Sensors
L	1 – 2 Ghz	30 - 15 cm	SeaSat, JERS-1, ALOS-PALSAR 2*, SAOCOM*
S	2 - 4 Ghz	15 - 7.5 cm	Huanjing-1C*
C	4 – 8 Ghz	7.5 – 3.75 cm	ERS-1/2, RADARSAT-1/2, ENVISAT, Sentinel-1A/1B*
X	8 - 12 Ghz	3.75 – 2.5 cm	COSMO-SkyMed*, TerraSAR-X/Tandem-X*

The weather and daylight independence of radar remote sensing provides important advantages over visible and thermal systems for monitoring volcanic eruptions. For time-averaged effusion rate estimation in particular, digital elevation data created from multi-temporal interferometric SAR acquisitions have proven to be a useful data source, (Kubanek et al., 2013; Poland, 2014; Kubanek et al., 2015).

Calculating differences in topography at a volcano using DEM data acquired before, during, and after an eruption provides a direct measure of the volume of effusive material emplaced between DEM acquisition times (Stevens et al., 1999). DEM time series, therefore, provide a convenient means to derive time-averaged effusion rates during an ongoing eruption (Poland, 2014).

Various studies have shown the suitability of using DEM data to derive erupted volumes and time-averaged lava effusion rates. DEMs derived by stereo-optical instruments have been used to monitor effusion rates during ongoing eruptions (e.g., Schilling et al., 2008; Diefenbach et al., 2012; Diefenbach et al., 2013). Similar to AVHRR, the disadvantage of these methods lies in their dependence on sufficient daylight and suitable weather conditions, limiting the ability of optical sensors to provide regular DEM data during an ongoing event (Poland, 2014).

Interferometric synthetic aperture radar (InSAR) data can help overcome these limitations by providing cloud-penetrating and daylight-independent observations of an active volcano (Kubanek et al., 2017). Repeat-pass InSAR data was used to generate lava flow thickness and volume information for eruptions at Mt Etna, Italy (Stevens et al., 2001); Santiaguito Volcano, Guatemala (Ebmeier et al., 2012); El Reventador Volcano, Ecuador (Naranjo et al., 2016); and Augustine Volcano, Alaska (McAlpin et al., 2017). While these studies resulted in beneficial deposition-volume measurements, the sensitivity of repeat-pass data to surface deformation, plus the often rapid loss of interferometric coherence at active volcanoes was found to be a cause of significant error in DEM estimates derived from repeat-pass InSAR (Wadge, 2003; Kubanek et al., 2017).

The DLR's TanDEM-X satellite mission provides a solution to the disadvantages of repeat-pass InSAR. TanDEM-X is composed of two nearly identical, C-band radar satellites flying in close formation (the first satellite is designated TanDEM-X, and the second, TerraSAR-X (it can be a source of some confusion that both the mission, and one of its two satellites are designated TanDEM-X). The primary objective of the TanDEM-X mission is the generation of DEMs at high spatial resolution and vertical accuracy (Krieger et al., 2007). Its bistatic acquisition mode, in which one transmitting station and one receiving station are separated in space (Kostylev, 2007), permits regular, near-simultaneous InSAR acquisitions over volcanic targets, forming the basis for the generation of DEM time series at 11-day intervals or multiples thereof (Kubanek et al., 2015). Hence, TanDEM-X DEM data are increasingly used to estimate volcanic effusion rates. Recent examples include the estimation of lava dome volumes at Merapi Volcano, Indonesia, and Volcan de Colima, Mexico (Kubanek et al., 2013); analysis of the time-averaged discharge rate of subaerial lava at Kilauea Volcano, Hawai'i (Poland, 2014); and the estimation of total effusion for the Tolbachik Volcano eruption (Kubanek et al., 2015). .

3.3 Methods

3.3.1 Thermal datasets

To examine the activity of Tolbachik Volcano, 2569 AVHRR observations during the TFE were acquired between 27 November 2012 and 27 August 2013. Each observation consists of Tolbachik geographically situated within a 40 × 40 pixel grid corresponding to an area of 44 km × 44 km. The grid is produced from AVHRR full-scene acquisitions of 2400 × 6400 km (USGS, 2018), which were received at UAF, and divided at the time of acquisition into seven subsections of two sizes: five are 563 km × 563 km, and two are 1126 km × 1126 km. Active volcanoes within each subsection, including Tolbachik, were identified and assigned to an area of interest within a 40 × 40 pixel square (Dean et al., 1998).

3.3.1.1 AVHRR data for the TFE

Archived AVHRR data at UAF was available in individual datasets for each of the 2569 observations acquired during the nine month TFE. Each 40×40-pixel observation consists of 69 fields containing dates, each band's maximum and mean radiant temperatures, local zenith angles for the 40×40 grid, as well as other data for each of 1600 pixels in each grid. Raw AVHRR data was downloaded at UAF and converted to radiant temperatures (°C) and albedo (%) using an inverse Planck function before being archived (Lauritson et al., 1979; Dehn et al., 2000). For ease of analysis, all 2569 observations were condensed to 13 pertinent data fields each, and reshaped into a 1600 × 13 × 2569 data matrix.

Processing by the well-tested Okmok II algorithm identified thermal anomalies, but within a monitoring structure designed primarily to detect new thermal anomalies. Consequently, the algorithm flags a maximum of 25 anomalous pixels per observation, under the assumption that pixel counts greater than 25 no longer contribute to the objective of detection (J. Dehn, pers. comm.). To insure all thermal anomalies were accounted for, the AVHRR band 3 radiant temperatures from each 40×40 pixel grid were fit to a normal distribution, and the mean (μ) and standard deviation (σ) of background temperatures computed. Thermal anomalies were redefined as all pixels with an AVHRR band 3 radiance temperature exceeding $\mu + 5\sigma$. This was a judgmentally determined threshold, which we believed was large enough to exclude warm crust and relatively minor atmospheric reflections, but small enough to include substantially all significant episodes of effusion. Results were evaluated based on inspection, with outliers removed as described in Section 3.4.1.1. This is a relatively simple method compared to the Okmok II algorithm, but one that is also intuitive and easy to use, while at the same time sufficient to resolve the 25-pixel limit with practical effect.

3.3.1.2 Saturation of thermal sensors and other issues

Of the initial 2569 observations, at least 1188, or 46%, contained saturated pixels in the mid-IR (AVHRR band 3). Saturation issues (described in Section 3.2.3), proved to be particularly prevalent during the early phases of the eruption, where large volumes of newly emplaced lava overwhelmed the AVHRR temperature range for up to 90% of the available observations (Figure 3.4). For large effusive events like the TFE, it was clear that saturation poses a significant challenge for effusion rate (E_r) estimation from AVHRR alone.

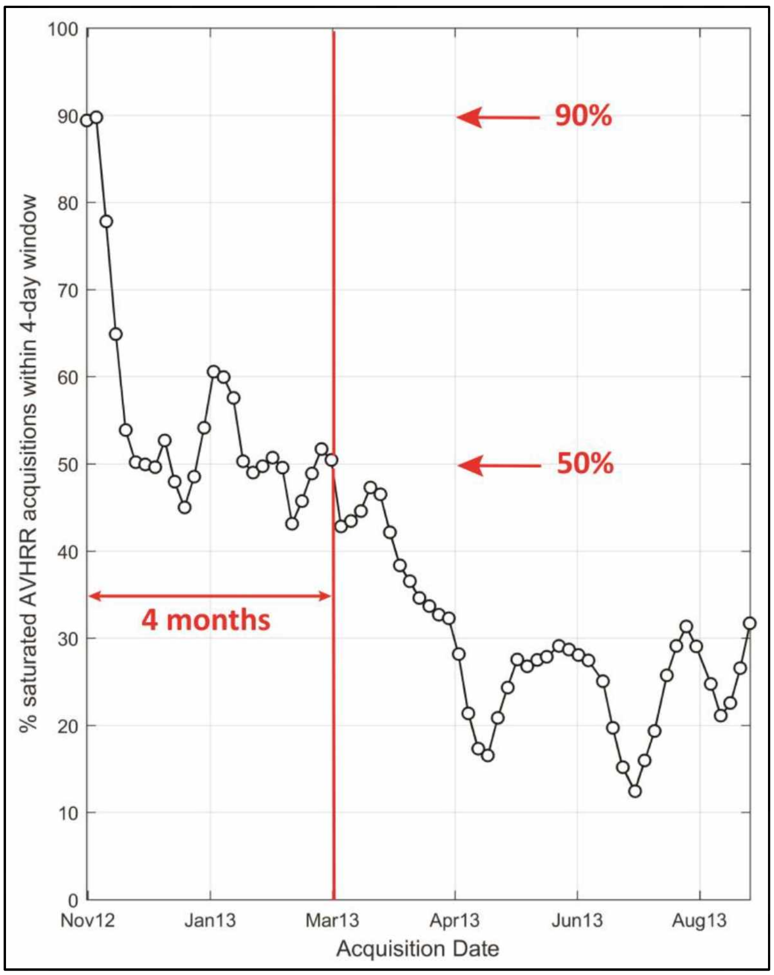

Figure 3.4: Percentage of AVHRR band 3 acquisitions with saturated pixels during the nine-month TFE.

For temperature and area estimates, examination using the three component model of Harris (2013), described in Section 3.2.2, was considered necessary due to the large size and complex geometry of the eruption (Gordeev et al., 2013; Dvigalo et al., 2014; Belousov et al., 2015; Melnikov and Volynets, 2015; Senyukov et al., 2015), which would create at least three components: incandescent lava, cooler crust, and cold, ambient surfaces. It therefore seemed prudent to consider the observation from Harris (2013), that in lava flows with three thermal components, a two-component model will have limited accuracy.

Issues with frequent thermal saturation of AVHRR band 3 data, especially during the most active parts of the TFE, complicated the inversion of thermal components using the three-component method, leading to bias and stability issues of the solution. Endeavors to estimate large scale lava flow temperatures and areas with a three-component model were re-focused in favor of the development of an alternative method that relies only on the more robust detection of thermal anomalies.

Even without relying on the three component method, the original archive of 2569 thermal observations from AVHRR during the TFE was still available. Such a data volume contains valuable information if it can be extracted and practically analyzed. It was apparent, for instance, that a saturated AVHRR band-3 pixel can be interpreted as thermally anomalous, since its integrated radiance temperature met our working saturation level of at least 62 °C. Given prior knowledge that the TFE was a largely effusive eruption, we inferred that saturated pixels present during the eruption period contained effused lava.

This assumption does not require an estimate of radiant temperature from the sensor; all that is necessary is to identify pixels with thermal anomalies from the AVHRR data stack. The $\mu + 5\sigma$ threshold test (see Section 3.3.1.1) was applied to accomplish this task, resulting in the time series of thermal anomalies, *HS(t)*. The resulting time series provides a day-by-day profile of activity during the TFE (see Figure 3.12), tracing variations of effusion as the event progresses.

Despite its importance for identifying variations in effusion, *HS(t)* cannot directly measure the desired parameters of effused volume, *V(t,)* and effusion rates, $E_r(t)$, because additional information and assumptions are needed to scale thermal anomaly data into these variables.

3.3.2 Synthetic aperture radar (SAR) data

If such additional information could not be found within the AVHRR data, then it could potentially be found or inferred with SAR observations. Using interferometric processing of the phase information, high resolution, three-dimensional maps can be created from data of the TanDEM-X mission as discussed in Section 3.2.5. When compared for differences, the resulting digital elevation models (DEMs) provide accurate, high spatial-resolution maps of changes in topography during the course of the eruption; i.e., highly reliable estimates of effusive volume and activity.

The high spatial resolution of SAR data offers a solution that AVHRR's coarse resolution cannot match, but at a cost of temporal sampling. While TanDEM-X has the theoretical capability to provide DEM data every 11 days, the effective sampling suitable for DEM generation is typically lower. This is due, in part, to the reality that DEM generation requires certain optimized observation conditions that are not always met. Available DEM-capable TanDEM-X datasets for the TFE are discussed below.

3.3.2.1 TanDEM-X data for the TFE

The TanDEM-X datasets were acquired in bistatic InSAR stripmap mode with an azimuth resolution of 2 m and a ground range resolution of 1.5 m to 3.5 m (Roth, 2003). This mode uses either TerraSAR-X or TanDEM-X satellites as a transmitter to illuminate a common radar footprint on the Earth's surface. The full list of TanDEM-X data used in this study is provided in Table 3.3, together with parameters relevant for InSAR-based DEM generation. A total of 12 bistatic TanDEM-X InSAR pairs were analyzed, including a pre-eruption data pair from 15 November 2012, used as the base dataset to estimate the eruption. Ten syneruptive InSAR pairs are available between 7 December 2012 and 17 August 2013, providing DEM data on time intervals between 11 and 55 days. The largest sampling gap (55 days) occurred between 16 March 2013 and 10 May 2013. One post-eruption pair, acquired on 11 October 2013, is used to assess the total deposition volume accumulated throughout the eruption.

Table 3.3: Dates of TanDEM-X data acquisitions with selected parameters applicable to DEM generation.

Timing	**Acquisition Date**	**Effective perpendicular baseline $B_{\perp}$ [m]**	**Height of ambiguity [m]**	**Average interferometric coherence [γ]**	**Temporal baseline [days]**
Preeruptive	11-15-2012	31.6	-210.6	0.83	0
Syneruptive	12-07-2012	40.6	-162.0	0.84	11
	12-18-2012	41.3	-159.4	0.84	11
	01-09-2013	42.1	-155.9	0.84	22
	02-22-2013	53.8	-120.3	0.83	44
	03-16-2013	53.5	-120.8	0.83	22
	05-10-2013	25.2	-261.1	0.84	55
	06-01-2013	31.8	-206.1	0.83	22
	06-23-2013	28.1	-233.8	0.85	22
	07-15-2013	37.9	-171.2	0.85	22
	08-17-2013	110.2	-58.9	0.81	33
Posteruptive	10-11-2013	92.9	69.5	0.81	55

3.3.2.2 InSAR processing workflow for DEM generation

The derivation of DEMs from TanDEM-X InSAR data takes advantage of the sensitivity of the interferometric phase ϕ to surface topography. The interferometric phase of a generic SAR interferogram is the sum of the phase contributions from all elemental scatterers in the resolution element, and can be expressed as

$$\phi_{i,j} = \phi_{i,j,defo} + \phi_{i,j,topo} + \phi_{i,j,atm} + \phi_{i,j,orbit} + \phi_{i,j,noise} \tag{3.3}$$

where $\phi_{i,j}$ is the InSAR phase calculated from SAR acquisitions i and j. The phase values $\phi_{i,j}$ contain information about the surface topography h encoded in phase component ($\phi_{i,j,topo}$) as well as the surface deformation $\Delta d_{i,j} = \left(d_j - d_i\right)$ that occurred between the image acquisition times t_i and t_j ($\phi_{i,j,defo}$). The InSAR phase, $\phi_{i,j}$ is furthermore affected by differences in the atmospheric propagation properties at times t_i and t_j ($\phi_{i,j,atm}$), errors in satellite orbits ($\phi_{i,j,orbit}$), and noise ($\phi_{i,j,noise}$).

For bistatic TanDEM-X acquisitions, we can assume that $t_i \approx t_j$ such that $\phi_{i,j,defo}$ and $\phi_{i,j,atm}$ can be considered negligible; hence Eq. 3.3 simplifies to

$$\phi_{i,j}^{TDX} \approx \phi_{i,j,topo}^{TDX} + \phi_{i,j,orbit}^{TDX} + \phi_{i,j,noise}^{TDX} \tag{3.4}$$

To extract topography information from Eq. 3.4, suppression of orbit errors ($\phi_{i,j,orbit}^{TDX}$) and appropriate statistical modeling of measurement errors ($\phi_{i,j,noise}^{TDX}$) needs to be accounted for in the analysis. Then, the sensitivity of the phase values in Eq. 3.4 to the target parameter h (surface topography), is given by

$$\phi_{i,j,topo} = \frac{4\pi}{\lambda} \frac{B_{i,j,\perp}^{eff}}{r \cdot sin(\theta)} h \tag{3.5}$$

where $B_{i,j,\perp}^{eff}$ is the effective perpendicular baseline corresponding to half of the perpendicular baseline of the bistatic TanDEM-X acquisition geometry (Table 3.1). In Eq. 3.5, r is the sensor-to-target range, θ is the look angle of the system, λ is the wavelength of the transmitted signal, and h is the surface elevation.

InSAR processing can generally be divided into three parts: (1) the pre-eruption DEM processing, (2) the syneruption and posteruption DEM processing, and (3) the differential DEM analysis. A short synopsis of the processing approach, condensed from Kubanek et al. (2017) is provided below.

1. Pre-eruption DEM processing: To derive information about the pre-eruptive topography of Tolbachik Volcano, a DEM acquired by the Shuttle Radar Topography Mission

(SRTM), flown on the Space Shuttle Endeavour in February, 2000 (Farr et al., 2007) was updated. An interferogram ϕ_{pre} was formed from the pre-eruption TanDEM-X data pair. To assist in phase unwrapping, a reference phase derived from the existing 90m-resolution SRTM DEM, ϕ_{ref_topo}, was subtracted from ϕ_{pre} resulting in the residual phase measurement φ. This residual phase φ is filtered and unwrapped using the Statistical-cost, Network-flow PHase-Unwrapping algorithm (SNAPHU) of Chen and Zebker (2002). The resulting φ_{unw} contains the difference Δh between the SRTM DEM and the true pre-eruption topography as well as a potential signal related to satellite orbit errors. A first-order polynomial plane is subtracted to compensate for these orbit errors arriving at $\phi_{\Delta h}$. The reference phase ϕ_{ref_topo} is added to $\phi_{\Delta h}$ and phase-to-height conversion is performed to arrive at the TanDEM-X-based pre-eruption DEM h_{pre}. The height map h_{pre} to a pixel spacing of 11.2 m × 13.2 m..

2. Syneruption and posteruption DEM processing: Each syn- and post-eruption data pair listed in Table 3.3 was processed in the same way as the pre-eruption data pair, but using the newly generated reference DEM h_{pre} to create the reference phase ϕ_{ref_topo}.

3. Differential DEM analysis: This step extracts deposition volumes from the DEM data. The pre-eruption DEM h_{pre} is subtracted from each processed syn- and post-eruption DEM in the geocoded domain. The DEM differencing enables mapping of the lava flows extruded between 15 November 2012 and the corresponding acquisition time of the syn- and post-eruption data pairs (Table 3.3). In addition, estimates of the lava flow volume and time-averaged discharge rates for different time intervals of the eruption can be calculated.

The time evolution of lava flow emplacement, calculated as described above, is shown in Figure 3.5, where progressive thickening of the flow can be seen in sequence in Figure 3.4(a) – 3.4(k).

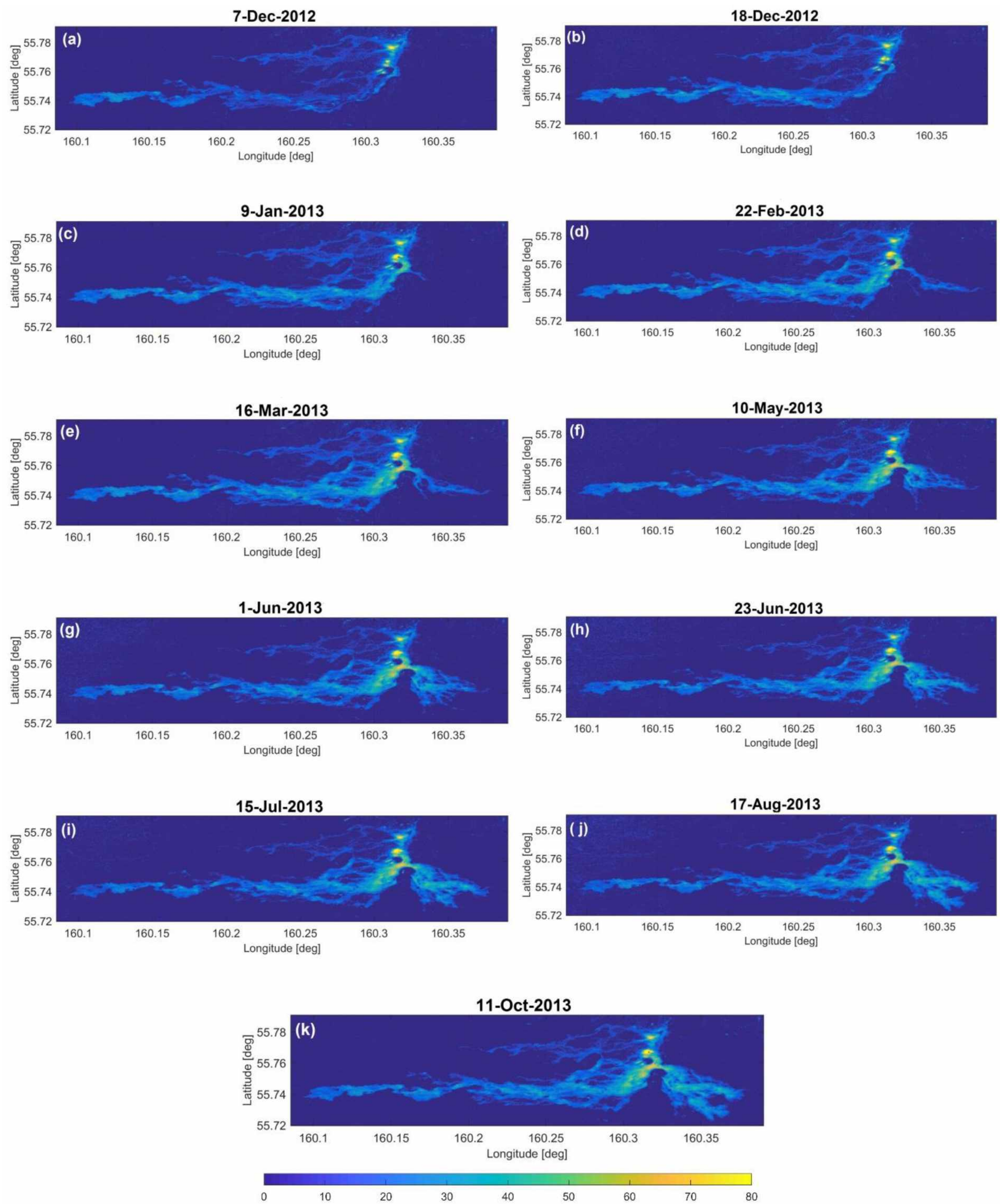

Figure 3.5: DEM time series during the TFE, calculated from TanDEM-X InSAR data (Kubanek et al., 2017). While TanDEM-X data is not always available on the same dates major events occur, the DEM time series is consistent with selected milestones as follows. (a)-(d) Menyailov Vents ceased effusion, and Vodopadnoye Lava Field stopped its westward growth in early December 2012; (c) Leningradskoye Lava Field reached its maximum length of 17.8 km in mid- December 2012: (c) Toludskoye Flow Field began to form in early January, 2013: (h) Flow field thicknesses reach 10 m at Vodopadnoye, 69 m at Leningradskoye, and 53 m at Toludskoye, early June, 2013: (j)-(k) Effusion reduces to zero, late August, 2013 (Belousov, 2015).

3.3.2.3 Accuracy assessment

An assessment of the derived DEM difference observations was conducted by Kubanek et al. (2017) that was based on four reference areas outside the footprint of the TFE lava flow. The areas were chosen to cover different topographic terrain and different levels of vegetation cover. An analysis of height differences within the selected reference areas resulted in a mean elevation difference (μ), centered on zero while the standard deviation of the mean elevations (σ_{μ}) in allreference areas was 1.63 m. These results indicate the TanDEM-X measurements of elevation differences were of high vertical accuracy. Additionally, the measurements indicate that flow thickness observations from TanDEM-X were not significantly biased.

3.3.3 Combining the AVHRR thermal time series and SAR DEM differencing

The goal of combining AVHRR hotspot and TanDEM-X DEM time series data was to improve upon the effusion rate observations extracted from the individual datasets alone. Of particular interest from this analysis was the extraction of time-averaged discharge rates for very large effusive eruptions such as the TFE.

As discussed above, the complementary properties of the two datasets suggest that a joint analysis of AVHRR thermal and TanDEM-X derived DEM time series data may provide new evidence on changing volcanic processes that cannot be gleaned from processing the datasets individually. The independent nature of their respective measurement variables is an additional benefit, as it ensures that the error sources affecting each measurement type are statistically uncorrelated.

The workflow of our data combination approach is shown in Figure 3.6, and uses the combined observations from TerraSAR-X DEMs and AVHRR hotspot time series to arrive at temporally detailed and physically unbiased information on the effused volume and the effusion rate history of the TFE. This approach is composed of three main processing steps, as follows. Step 1: an initial co-registration of AVHRR hotspot and TanDEM-X DEM data followed by a resampling of TanDEM-X data to the AVHRR observation geometry to prepare the data for joint processing. Step 2: a residual co-registration between the two datasets to identify and correct for occasional geolocation errors in AVHRR data; and Step 3: a fusion of the AVHRR and TanDEM-X data to develop at a joint time series of lava effusion.

3.3.3.1 TanDEM-X to AVHRR resampling

To process both datasets together, the AVHRR and TanDEM-X data must be available in the same geographic coordinate system. While both datasets are available in a WGS84 reference frame and latitude-longitude coordinate grid, their initial spatial resolution is different and needs to be harmonized.

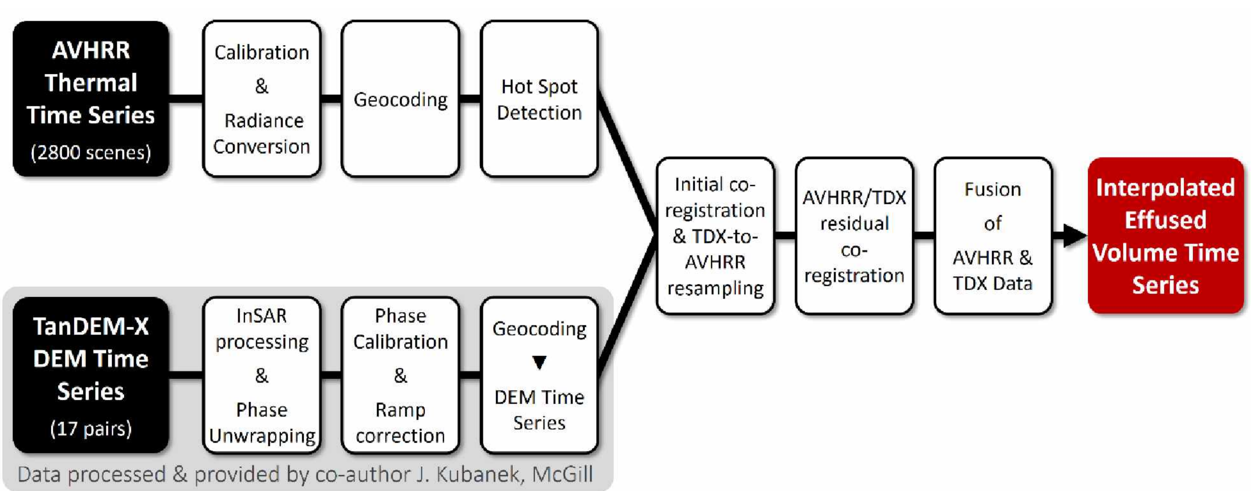

Figure 3.6: Workflow for combining TanDEM-X-derived DEM time series information with AVHRR thermal data for improved effusion rate information.

As the final time series will be sampled at the AVHRR acquisition times, the coarser resolution of the yet more frequently acquired AVHRR data was selected as the reference geometry for the joint data stack. It was therefore necessary to resample the TanDEM-X-derived flow thickness time series, $F(t)$, onto the AVHRR geometry, resulting in resampled flow thickness data, $F_{res}(t)$. This resampled dataset has a spatial sampling of 0.016°, corresponding to an approximate pixel size of 1.1 km × 1.1 km. An example of a resampled flow thickness map from 11 October 2013 is shown in Figure 3.7. Note that the maximum flow thickness appears reduced, as the original flow thickness map, shown in Figure 3.5k, is resampled to the lower AVHRR resolution.

3.3.3.2 Residual AVHRR/TanDEM-X co-registration

To facilitate the combination of AVHRR and TanDEM-X DEM time series, an accurate co-registration between the two datasets is essential. To this end, occasional mis-registrations of AVHRR observations must be identified and corrected. These mis-registrations originate from

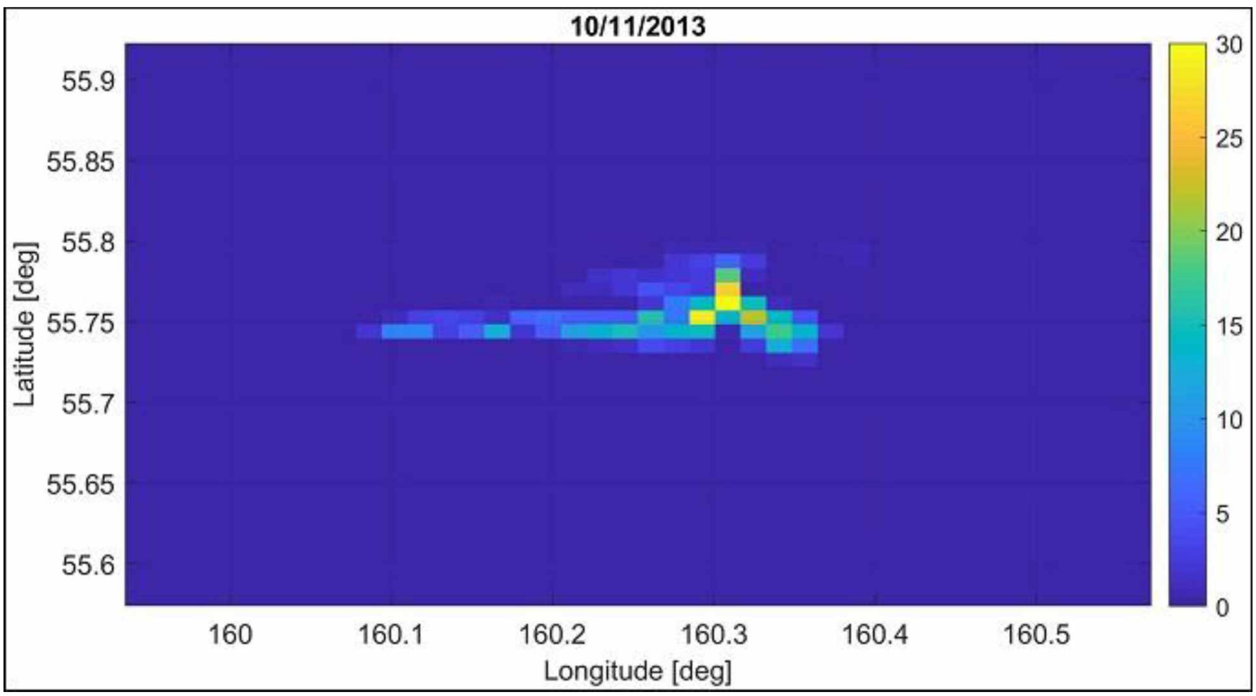

Figure 3.7: Flow thickness map $\boldsymbol{F_{res}}$ from 11 October 2013, originally shown in Figure 3.5(k), resampled to the lower AVHRR resolution.

spurious geolocation errors that occur when AVHRR observations are acquired at a shallow scan angle; i.e., when Tolbachik Volcano is near the western edge of the swath width (better acquisitions are possible when the target has moved closer to the satellite's nadir, but by this time, the UAF receiving station would be out of position).

To facilitate the identification and correction of occasional AVHRR registration errors, a three-step pattern matching approach was developed:

1) The flow thickness difference, $\boldsymbol{\Delta F_{res}}$, between two consecutive TanDEM-X acquisition time steps $\boldsymbol{t_{TDX}(n-1)}$, and $\boldsymbol{t_{TDX}(n)}$ is calculated.

2) Height error $\boldsymbol{\sigma_{F_{res}}} = \boldsymbol{\sigma_F/\sqrt{m}}$ is used with the AVHRR/TanDEM-X resolution ratio m to identify pixels showing significant flow thickness increases between time steps $\boldsymbol{t_{TDX}(n-1)}$, and $\boldsymbol{t_{TDX}(n)}$ according to

$$\Delta F_{res} > 2\sigma_{F_{res}} \tag{3.6}$$

Here, a significant flow thickness increase is defined as that in excess of two standard deviations as a means to limit the risk of incorrect acceptance to 5% or less.

3) The final step, the identified pixel pattern is co-registered to the hot spot maps of all AVHRR acquisition times, $\boldsymbol{t_{AVHRR}}$, between $\boldsymbol{t_{TDX}(n-1)}$, and $\boldsymbol{t_{TDX}(n)}$, by calculating the geometric center of the respective pixel masks, measuring their offsets in latitude and longitude direction, and correcting these identified offsets.

Figure 3.8 shows an example of the achieved co-registration quality. Here, AVHRR hot spot pixels (in white) on 9 December 2012, are overlain on pixels with significant flow thickness increases between TanDEM-X DEM observations from 7 December 2012 and 18 December 2012 (in gray). It can be seen that all thermal anomalies are contained within areas that experienced flow thickening.

Although Figure 3.8 was intended to demonstrate co-registration quality, it also results in a comparison of hot spot locations relative to areas of significant flow thickness. This is suggestive of levee formation quite early in the eruption, particularly when viewed with the lava flow emplacement maps in Figure 3.5, which similarly indicate thickening near the flow centerlines.

3.3.3.3 Fusion of AVHRR and TanDEM-X DEM time series information

After resampling and residual co-registration, the data are now ready for combination. Our approach for AVHRR/TanDEM-X fusion rests on the following considerations:

- Each DEM in the TanDEM-X-based time series is assumed to provide unbiased estimates of the flow thickness *F(t)* and the total effused volume *V(t)* at the observation times $\boldsymbol{t_{TDX}}$.
- Differences in flow thickness (*ΔF(t)*) between time steps $\boldsymbol{t_{TDX}(n-1)}$ and $\boldsymbol{t_{TDX}(n)}$ are assumed to be the sum of all effusive events that occurred between these two time steps.

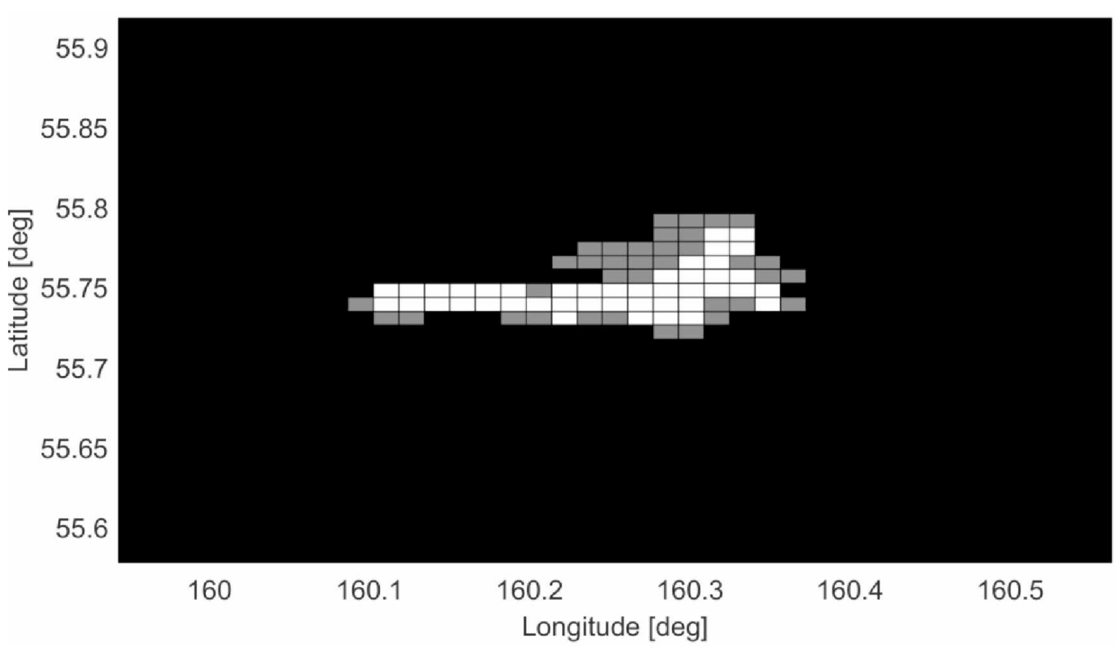

Figure 3.8: A comparison of AVHRR hotspot pixels (in white) to pixels with significant flow thickness increase (in gray) for 9 December 2012 demonstrates the quality of co-registration method. All thermal anomalies identified for 9 December 2012, are contained within the area for which TanDEM-X detected a flow thickening increase between 7 December 2012 and 18 December 2012.

- Thermal anomalies extracted from AVHRR data are assumed to capture effusive events at observation times $\boldsymbol{t_{AVHRR}}$ and represent the number and the timing of effusive events between TanDEM-X observation times $\boldsymbol{t_{TDX}(n-1)}$ and $\boldsymbol{t_{TDX}(n)}$.

Based on these considerations, we can establish that the joint time series, $F_{AVHRR+TDX}(t)$, represents the thickness of emplaced material at each of the N TanDEM-X acquisition points, t_{TDX}. High temporal resolution AVHRR hotspot information is used to interpolate between those TanDEM-X acquisition points by assuming each AVHRR hotspot between time steps $t_{TDX}(n-1)$, and $t_{TDX}(n)$, adds the following amount of flow thickness

$$\Delta F_{HS}(n) = \frac{[F(t_{TDX}(n)) - F(t_{TDX}(n-1))]}{k_{HS}} \quad \forall \quad n \in N \tag{3.7}$$

with k_{HS} being the number of AVHRR thermal anomalies detected between time steps $t_{TDX}(n-1)$ and $t_{TDX}(n)$. This allows the flow thickness time series of the joint AVHRR/TanDEM-X acquisition times to be expressed as:

$$F_{AVHRR+TDX}(t) = \begin{cases} F(t) & if \quad t \in t_{TDX} \\ F_{AVHRR+TDX}(t-1) & if \quad HS(t) = 0 \\ F_{AVHRR+TDX}(t-1) + \Delta F_{HS}(n) & if \quad HS(t) = 1 \end{cases} \tag{3.8}$$

Figure 3.9 conceptually demonstrates the approach for generating flow thickness time series information from the joint processing of AVHRR/TanDEM-X acquisitions. It displays the thickness evolution of the flow deposit, $F_{AVHRR+TDX}(t)$, at a single pixel in the AVHRR domain. The integrated TanDEM-X-based flow thicknesses are used to interpolate between less frequent TanDEM-X acquisition times, revealing evidence of the ebb and flow of volcanic activity at high temporal resolution with minimal bias.

3.3.4 Eruption characterization from AVHRR/TanDEM-X time series data

The combination of TanDEM-X DEM data with AVHRR hotspot data adds new, critical details to the previously known eruption profile of the TFE. Using the AVHRR hotspot information, with its higher temporal resolution, to interpolate deposition between TanDEM-X DEM acquisition points improves the timing of the onset of the eruption, and reveals several periods of higher effusion that were not detectable in the TanDEM-X DEM data alone.

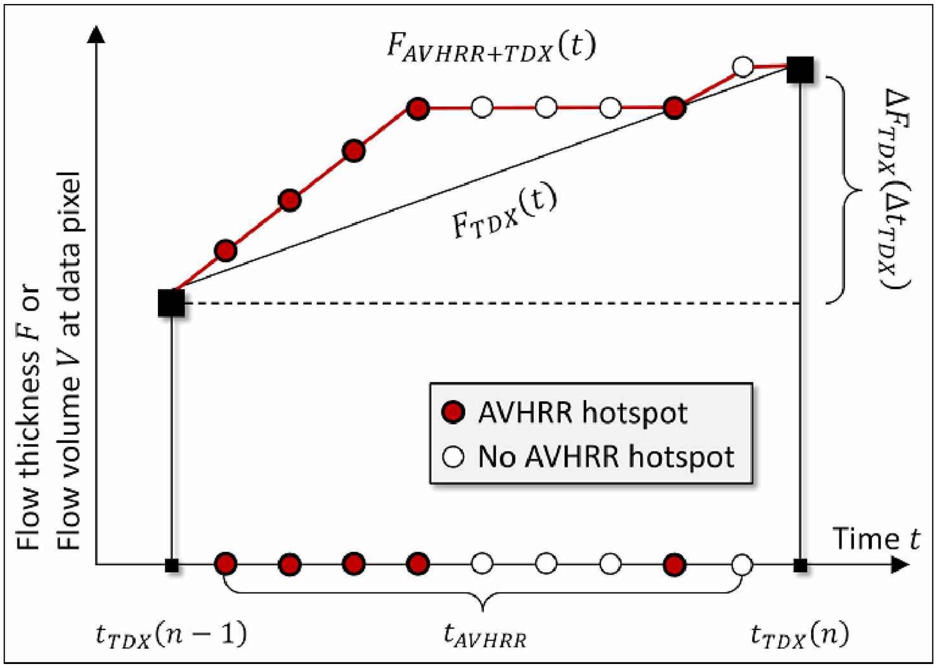

Figure 3.9: Principle of AVHRR/TDX combination for improved estimation of effusive history. effusion between two data points $t_{TDX}(n\text{-}1)$ and $t_{TDX}(n)$ by TanDEM-X alone presents as a linear function. By interpolating AVHRR pixel counts as described in the text, a more responsive polynomial trend emerges.

3.3.4.1 Total effused volume

Figure 3.10 shows the evolution of the total effused volume of the TFE as derived via the developed joint-series method (blue line) in comparison to the previously available information (TanDEM-X DEM time series; green line/triangles). The first 5.5 months of the eruptive phase are shown, and demonstrate that the joint time series traces the TanDEM-X-only derived effused volume time series published by Kubanek et al., (2017) without significant bias, while increasing the amount of available detail about the temporal evolution of the TFE. Both time series record a total of 0.45 km^3 of effused material over the first 5.5 months of the eruption with 66% of the material (0.4 km^3) emplaced within its first 20 days. In addition to the TanDEM-X observations alone, the joint AVHRR/TanDEM-X effusion volume time series clarifies the timing of the onset of the eruption and reveals several periods of higher effusion that were previously undetectable. More information from the generated data is presented in Section 3.4.1.

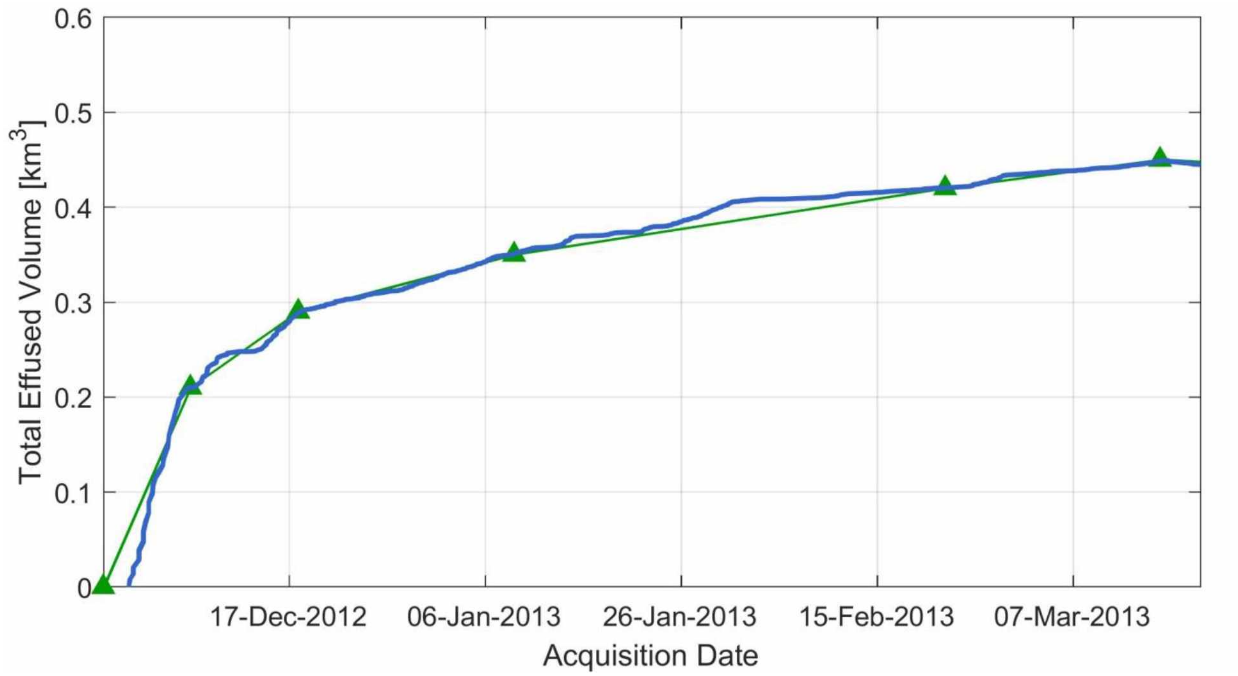

Figure 3.10: Time evolution of total effusion volume (km^3). Cumulative deposition determined by combined AVHRR and TanDEM-X DEM data are shown in blue; TanDEM-X data alone is shown in green/triangles. The first 5.5 months of the eruptive period are shown. The combination of TanDEM-X DEM information with AVHRR hotspot data reveals new details about variations in effusive volcanic activity over time.

3.3.4.2 Time-averaged discharge rates for the TFE

Time-averaged discharge rates (Figure 3.11) are calculated from the total effused volume information by dividing volume increases between two consecutive time steps by their respective time difference. As volcanic activity can vary widely at the temporal sampling of AVHRR, effusion rates calculated at the full temporal resolution of AVHRR would lead to information that is difficult to analyze due to its high level of detail. To avoid this, we chose to derive time-averaged discharge rates on a 5-day basis instead. This 5-day basis was found to be a good compromise between preserving temporal detail without obscuring the long-term behavior of effusion with a high level of short-term variability.

Five-day time-averaged discharge rates derived from the joint AVHRR/TanDEM-X time series are displayed as a bold blue line in Figure 3.10. The information in this figure indicates that most lava was effused during the first few days of the eruption, maintaining a time-averaged discharge rate of ~ 300 m³ s^{-1} throughout the initial 10 days of the event. Effusion dropped significantly thereafter, maintaining ~100 m³ s^{-1} for another 10 days before leveling out at 0–30 m³ s^{-1} for most of the remainder of the event. A measurable increase in effusion is observed near the end of the eruptive period, adding a final 0.05 km³ of lava in August 2013 before activity ceased later in that month. This uptick was also observed in the original TanDEM-X-based DEM time series and is mostly related to the final buildup of the Toludskoye Lava Field (see Section 3.4.1.2).

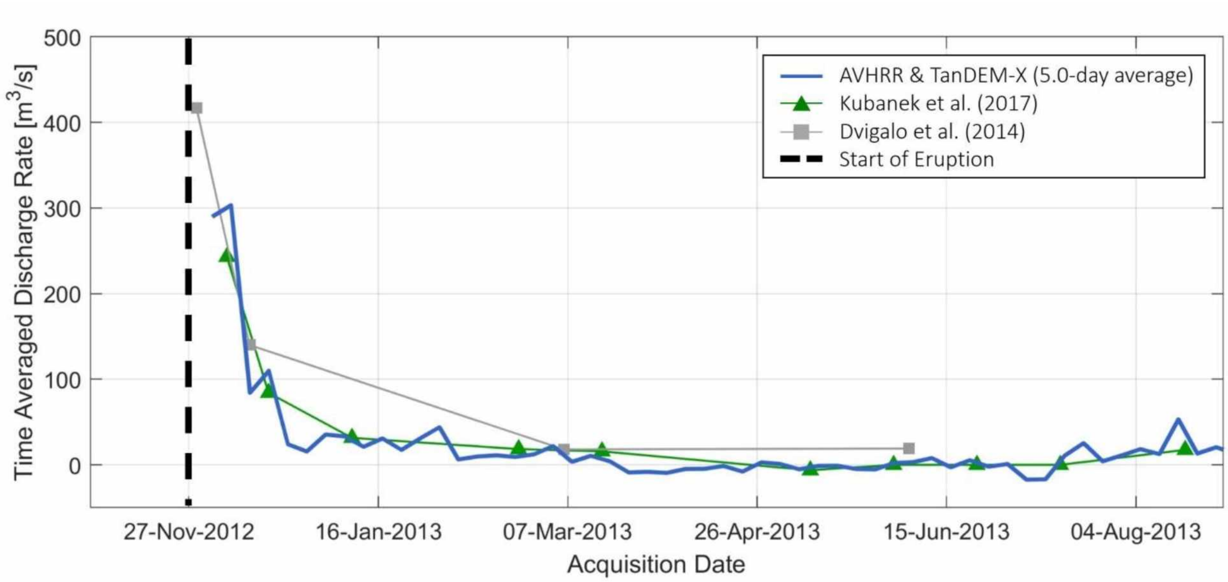

Figure 3.11: Comparison of time-averaged effusion rates from TanDEM-X DEM differencing (Kubanek et al., 2017), stereo photogrammetric measurements (Dvigalo et al., 2014), and five-day moving average integrated AVHRR/TanDEM-X time series.

To validate the derived effusion rate information, the data in Figure 3.11 is augmented with previously published effusion-rate information. Dvigalo et al. (2014) processed multi-temporal photogrammetric data from an airborne platform to derive multiple DEMs over the areas covered by lava flow deposits. A total of four DEMs were available throughout the duration of the event with acquisition dates on 29 November 2012, 13 December 2012, 06 March 2013, and 05 June 2013. Lava flow volumes were calculated from the DEMs and time-averaged discharge rates were derived (gray line and squares in Figure 3.11). Kubanek et al., (2017) generated DEMs at sparse temporal sampling from TanDEM-X data to assess the effusive behavior of the TFE. These DEMs (described in more detail in Section 3.3.2.1) allowed for the generation of effusion-rate information at about a monthly sampling rate (green line and triangles in Figure 3.11).

Figure 3.11 shows a good relationship between the joint AVHRR/TanDEM-X derived effusion-rates with Dvigalo et al. (2014), while providing more temporal detail than previously available. During the first two days of the eruption, Dvigalo et al. (2014) reported a time averaged effusion rate of 417 $m^3 s^{-1}$ (restated from 440 $m^3 s^{-1}$ from the provided data) while Kubanek et al. (2017), reports a ten-day time average discharge rate of 248 $m^3 s^{-1}$. Both of these independent observations are within a reasonable range of the five-day moving average of ~300 $m^3 s^{-1}$ derived from the joint AVHRR/TanDEM-X data in this research study. Figure 3.11 highlights the similarity between the discharge and decay rates of the joint AVHRR/TanDEM-X time series, and the rates derived by Dvigalo et al. (2014) and Kubanek et al. (2017).

Compared to the two reference time series, the results from joint AVHRR/TanDEM-X processing show a rapid drop in time averaged discharge rate in early December 2012. This drop in activity corresponds to other published information. The joint AVHRR/TanDEM-X data also show a comparably quiescent period between 23 December 2012 and 28 December 2012 where time-averaged discharge rates dropped to approximately 20 $m^3 s^{-1}$. Short term variations in eruption rate are further analyzed for individual test sites in Section 3.4.1.2.

3.4 Discussion

3.4.1 New findings about the TFE

3.4.1.1 Characteristics of the time series of thermal anomalies *HS(t)*

The time series of thermal anomalies as detected from the available AVHRR data is shown in Figure 3.12. Similarly to the time-averaged discharge rate in Figure 3.11, this time series of hot pixel counts follows the same pattern expected from an effusive eruption as postulated in Wadge (1981); i.e., an effusion rate increasing rapidly to a maximum, then falling slowly with time. In

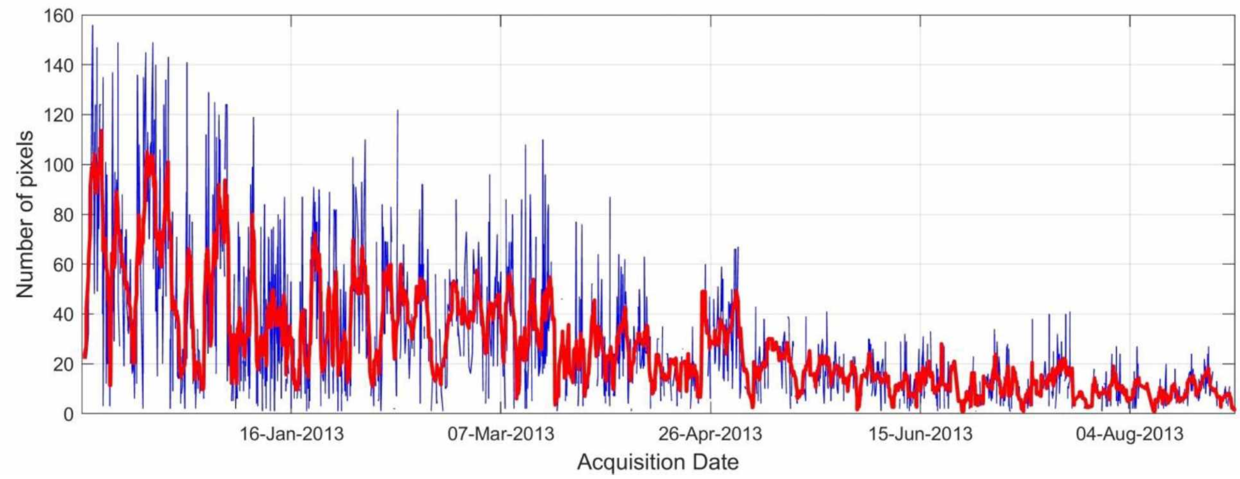

Figure 3.12: The number of thermal anomalies identified in AVHRR band 3 during the TFE, from 27 November 2012 through 27 August 2013. Blue lines represent actual pixel counts; red line represents a ten-observation smoothing.

Figure 3.11, the number of thermal anomalies is highest at the beginning of the eruption, when effusion is typically greatest, but decreases as the eruption progresses, until ceasing entirely after 27 August 2013. Observations with anomalously high pixel counts have been excluded from Figure 3.11. Such values, identified as those in excess of 1.5% of the interquartile range (Tukey, 1977), were considered outliers. To account for the heteroscedastic nature of the data, i.e., the significantly higher level of activity at the onset of the eruption, outliers were recomputed in two week windows.

During the course of the eruption, several episodic pulses of activity can be identified in Figure 3.11, providing a general timeline of the ebb and flow of the TFE. Strong variations in pixel counts are particularly evident in early phases of the eruption where periods of more vigorous effusion are interrupted by brief periods of relative quiescence. Hot pixel counts during these first two weeks of the eruption are shown in Figure 3.13 to demonstrate their association with previously reported field observations. Four activity phases (labeled (A) through (E) in

Figure 3.13) can be distinguished and compared to field-observed activity reports in Table 3.4. A comparison of the activity phases in Figure 3.13 with field reports in Table 3.4 shows generally good correspondence between the different data types.

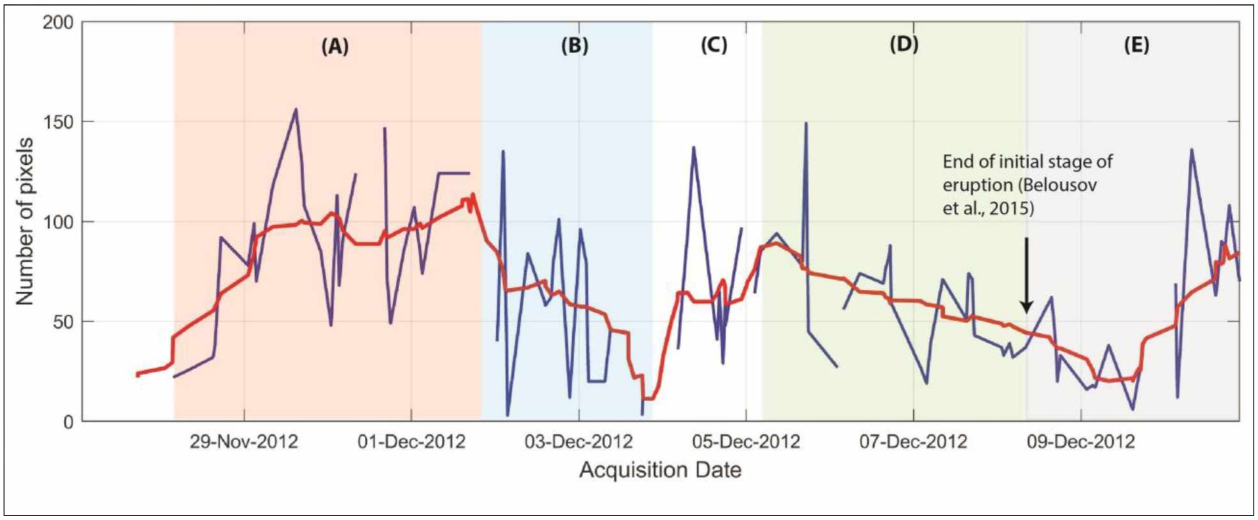

Figure 3.13: AVHRR hot pixel counts plotted during initial two weeks of the eruption demonstrate correspondence with observed activity. Blue line represents actual pixel counts; red line smoothed over ten observations. Descriptions of observed activity for phases (A) through (E) are listed in Table 3.4. Outliers, as described by Tukey (1977), were removed to clarify scaling.

3.4.1.2 Samples of lava deposition time series for selected geographic locations

Based on the joint AVHRR/TanDEM-X time series, we can explore the history of deposition for sample points across the lava flows emplaced by the TFE. In Figures 3.14 through 3.18, five selected sample points showcase the information in the joint AVHRR/TanDEM-X dataset, and analyze the timing of lava emplacement as a function of geographic location. These five sample locations (identified in Figure 3.2), are spread across the full reach of the 2012–2013 lava flow fields, and include locations near Naboko Vent (location #1), the Leningradskoye Lava Field (locations #2 and #5), and the Toludskoye Lava Field (locations #3 and #4). In Figures 3.12 through 3.16, both the joint time series (black lines) and the TanDEM-X-only time series (gray lines) indicate the evidence gained through the developed data combination. Descriptions of activity presented for each figure pertain to the limited area defined by a single resolution cell.

Table 3.4: Descriptions of reported activity during the first two weeks of eruption; phases (A) through (E) correspond to the periods identified in Figure 3.13.

Phase	Date/time (UTC)	Reported activity
(A)	28-Nov-2019, 03:41 through 30-Nov-2019, 21:47.	Eruption detection: red shading, reflects rapid increase in activity, characterized by visible lava fountains from both Menyailov and Naboko vents, explosive activity, eruptive fissures, and lava gushing from vents (Gordeev et al. 2013, Belousov et al., 2015, and Melnikov and Volynets, 2015); maximum time averaged discharge rate (440 m^3 s^{-1}) attained during this period (Dvigalo, 2014).
(B)	1-Dec-2012, 00:47 through 3-Dec-2012, 18:08.	Blue shading, corresponding to reported reduction of activity in multiple vents, and cessation of activity in the middle-upper parts of the eruption fissure and the Menyailov Vent (Belousov et al. , 2015, and Melnikov and Volynets, 2015).
(C)	3-Dec-2012, 18:27 through 5-Dec-2012, 02:22.	Unshaded: a brief pulse not directly reported by observers.
(D)	5-Dec-2012, 04:05 through 7-Dec-2012, 17:24.	Green shading; decrease in hot pixel counts corresponding to cessation of activity on the lowermost part of the eruption fissure (on the summit of Krasnyi Cone and its south-western foot); Vodopadnoye Flow Field stops; Naboko Vent feeds Leningradskoye Flow Field, which continues to grow (Belousov et al., 2015).
(E)	8-Dec-2012, 01:14 forward:	Gray shading; fountaining and outpouring of lava continues; growth of scoria/agglutinate cone at Naboko Vent. The next eight months' activity is described by Belousov et al. (2015), as relatively monotonous, with gradual transformations.

Accordingly, certain events, particularly dates and times related to the beginning and cessation of effusive activity, may differ in some degree from more general observations reported by observers.

Location #1 – near Naboko Vent (55.7612°N, 160.3087°E), Figure 3.14: The joint dataset clarifies the date and time of first deposition detected at this location as 30 November 2012, 02:42 UTC. Flow thickness increased rapidly during the early phases of the eruption until 7 December 2012 at 03:42 UTC when flowing lava slowed and nearly ceased. A significant increase in activity was observed again on 28 December 2012. Noticeable activity pulses followed between 25 January 2013 and 31 January 2013 as well as between 24 February 2013 and 1 March 2013. During both of these episodes, lava flow thickness increased rapidly over a short time. Lava flow thickening at these locations ceased on 8 May 2013.

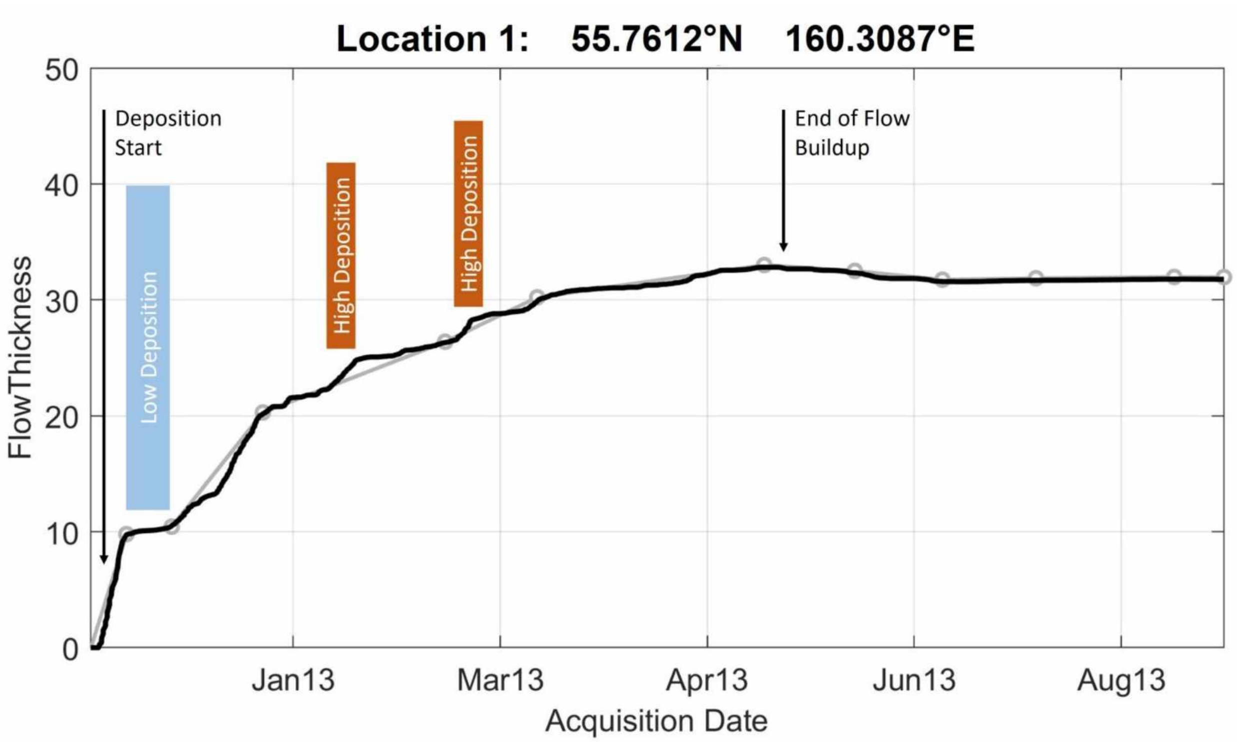

Figure 3.14: Time series of lava flow thickness for sample location #1, situated near Naboko Vent (55.7525°N, 160.2928°E). The joint AVHRR/TanDEM-X dataset is shown as black line; gray line shows information available from TanDEM-X DEM data only.

<u>Location #2 – Leningradskoye Lava Field (55.7525°N, 160.2928°E), Figure 3.15:</u> This location is ~1.9 km southwest of the Naboko Vent. Deposition began on 30 November 2012, 17:01 UTC, and proceeded rapidly until 9 January 2013, building a lava flow of significant thickness. This initial flow buildup was only briefly interrupted by two periods of comparably low deposition between 9 December 2012 and 14 December 2012, as well as between 23 December 2012 and 28 December 2012. Two more periods of significant thickening followed (21 January 2013 through 1 February 2013, and 27 February 2013 through 3 March 2013) before lava buildup ceased around 18 March 2013

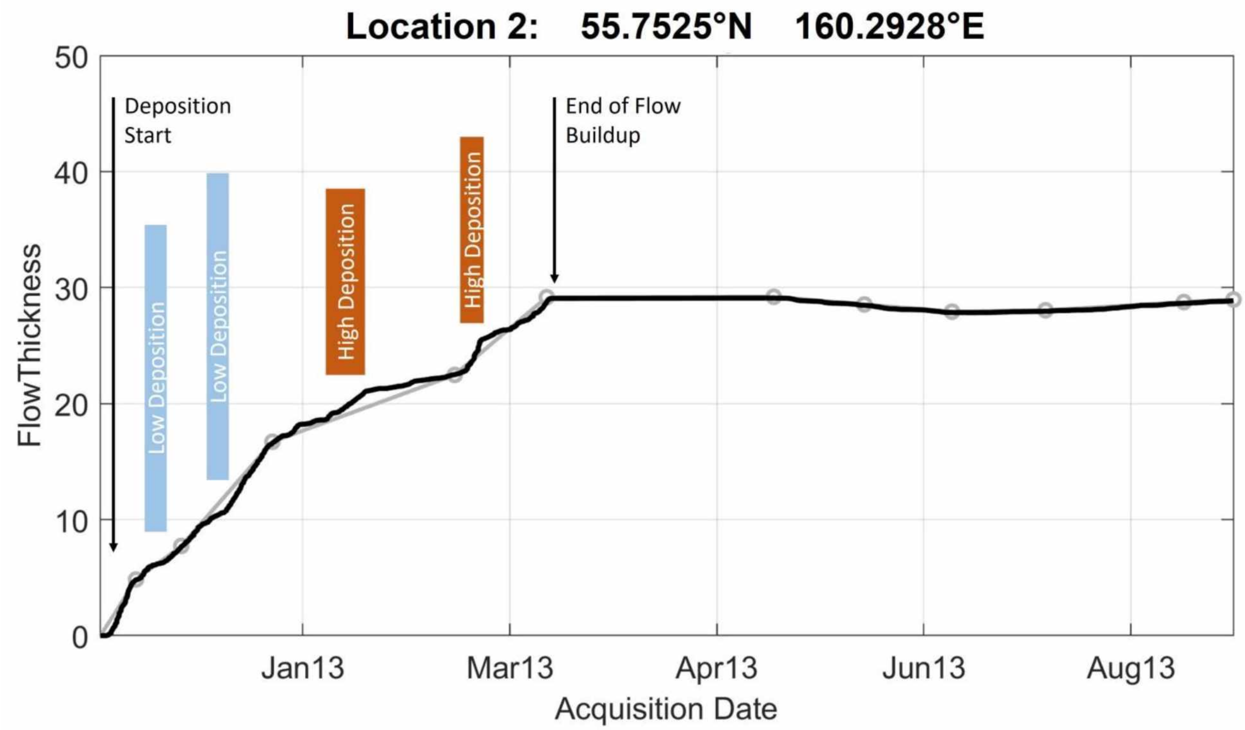

Figure 3.15: Time series of lava flow thickness for sample location #2, situated on Leningradskoye Lava Field (55.7525°N, 160.2928°E). The joint AVHRR/TanDEM-X dataset is shown as black line; gray line shows information available from TanDEM-X DEM data only.

Location #3 - Toludskoye Lava Field (55.7525°N, 160.3405°E), Figure 3.16: Even though the Toludskoye Lava Field began forming around 28 December 2012 (site location 55.7525°N, 160.3246°E, not shown) significant lava buildup at location #3 commenced only on 7 January 2013, 16:19 UTC. A first rapid pulse of initial lava flow thickening lasted until 1 February 2013, interrupted only by two short periods of slowdown between 11 January 2013 and 13 January2013, and from 15 January 2013 until 25 January 2013. After 1 February 2013, lava buildup at this location ceased for more than two months before restarting with varying activity levels on 8 April 2013. Last deposition at this location is recorded on 14 August 2013. Both the identified beginning and end of depositional activity at this site are consistent with field reports (Dvigalo et al., 2014; Belousov et al., 2015).

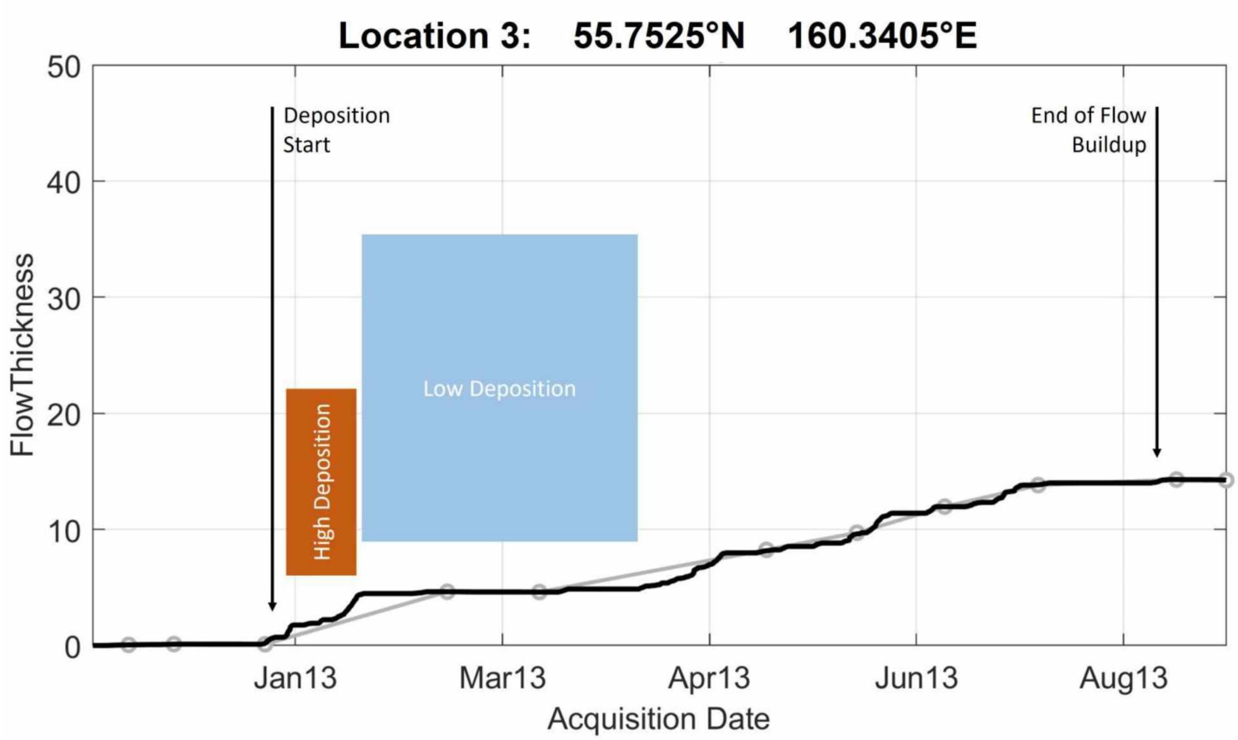

Figure 3.16: Time series of lava flow thickness for sample location #3, situated near the proximal end of Toludskoye Lava Field (55.7525°N, 160.3405°E). The joint AVHRR/TanDEM-X dataset is shown as black line; gray line shows information available from TanDEM-X DEM data only

Location #4 - Toludskoye Lava Field (55.7438°N, 160.3564°E), Figure 3.17: This location is ~1.5 km southeast of the previously discussed location #3, also situated on Toludskoye Lava Field. Initial buildup of flow thickness at this location started on 13 January 2013, and ended on 1 February 2013. The end of this initial buildup period was found to be identical for locations #3 and #4, providing evidence of the quality of the derived observations. After an extended period of little or no deposition, lava flow thickening restarted on 1 June 2013. Consistent with field reports (Dvigalo et al., 2014), the last detection of deposition at this site occurred on 26 August 2013.

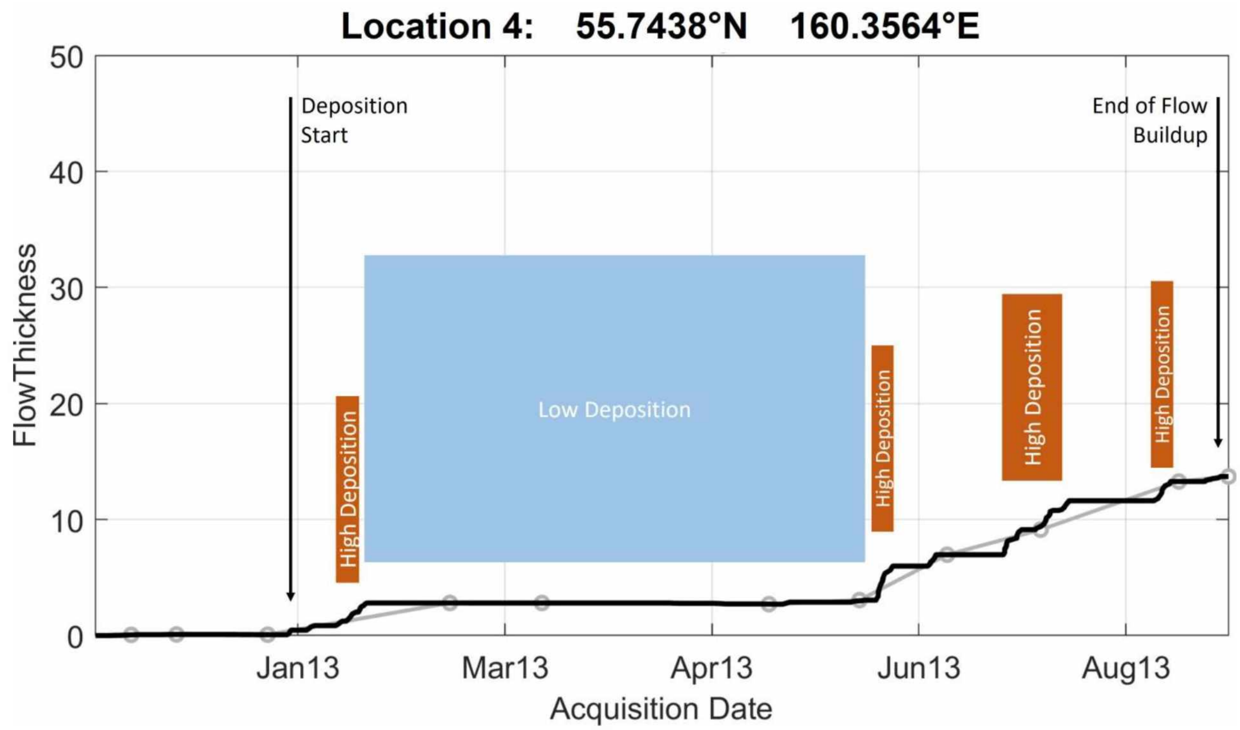

Figure 3.17: Time series of lava flow thickness for sample location #4, situated on Toludskoye Lava Field 55.7438°N, 160.3564°E). The joint AVHRR/TanDEM-X dataset is shown as black line; gray line shows information available from TanDEM-X DEM data only.

Location #5 - Leningradskoye Lava Field (55.7438°N, 160.1179°E), Figure 3.18:

This last site is located near the western edge of the Leningradskoye Lava Field and provides observations to determine when the Leningradskoye Lava Field reached its maximum length. The joint AVHRR/TanDEM-X data shows first signs of lava flow emplacement on 1 December 2012 at 03:06 UTC, only five days after the first reported lava flows on 27 November 2012, 05:15 UTC (Gordeev et al., 2013). This is consistent with other observations that indicate the Leningradskoye Lava Field was emplaced rapidly. While Dvigalo et al., (2014) reports Leningradskoye's maximum westerly extent only for 13 December 2013, the 12-day time offset is likely due to the spare data that was available. Dvigalo et al., (2014) observations were based on airborne imagery acquired on only four dates (29 November 2012, 13 December 2012, 06 March 2013, and 05 June 2013). The joint AVHRR/TanDEM-X time series, therefore, significantly improves upon previously existing information about the timing of maximum reach.

Figure 3.18 also shows that the last significant lava flow thickening was recorded on 8 December 2013 indicating that the westernmost reaches of this lava field were emplaced within the first 21 days of the eruption. While AVHRR recorded some additional thermal anomalies later on during the eruption, these did not contribute significantly to the overall thickness of the flow.

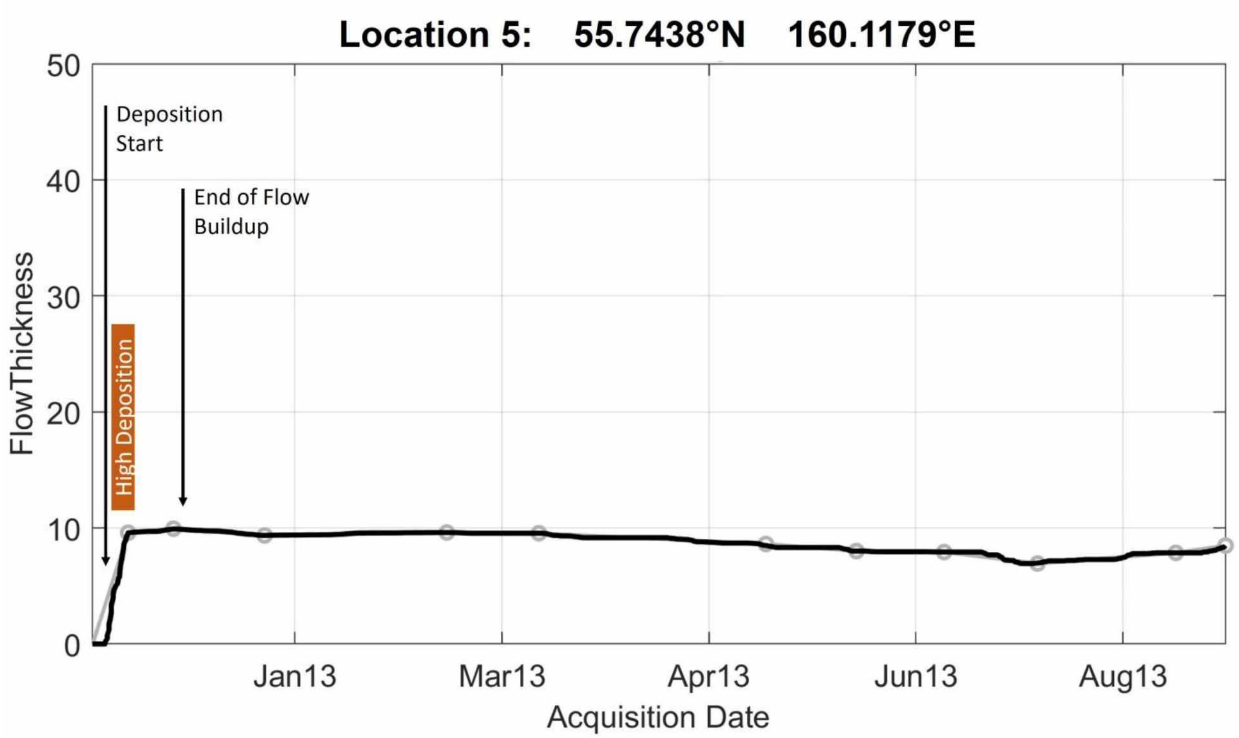

Figure 3.18: Time series of lava flow thickness for sample location #5, situated on Leningradskoye Lava Field (55.7438°N, 160.1179°E). The joint AVHRR/TanDEM-X dataset is shown as black line; gray line shows information available from TanDEM-X DEM data only

When compared to the total effused volume plot (Figure 3.10), the individual point locations indicate that most of the deposition during the eruption occurred near the main vents and along the Leningradskoye Lava Field. While the buildup of the Toludskoye Lava Field led to a noticeable uptick in the total effused volume and the time-averaged discharge rate (Figure 3.11) starting around mid-January and lasting until mid-February 2013, the contribution of this lava field to the total effused volume is ~13%. Our data shows cessation of the last significant lava deposition around 26 August 2013, which is in good agreement with the 23 August 2013 end of activity reported by Belousov et al., (2015), and the 27 August 2013 ending by Kubanek et al. (2017).

3.4.2 Main capabilities and limitations of developed technology

In this study, a combination of AVHRR hotspot and TanDEM-X DEM time series data were used to evaluate lava deposition for large effusive eruptions; specifically, the 2012-2013 volcanic eruption at Tolbachik Volcano, Kamchatka. Our approach was motivated by the complementary capabilities of the two data sources:

- TanDEM-X time series are able to provide unbiased information on effusion volumes and lava flow thickness for large effusive events, yet, their sparse temporal sampling leads to an incomplete characterization of the volcanic activity.
- AVHRR thermal remote sensing data provides regular observations of a volcanic system at a high temporal sampling rate of several measurements per day. Hotspot observations extracted from these data can provide a detailed history of the volcanic activity, yet, AVHRR's frequent saturation issues reduce the capability of the sensor to provide unbiased effusion information for eruptions creating large lava deposits over periods of weeks or months.

Our approach preserved the flow thickness and effusion volume observations at the sparse TanDEM-X DEM acquisition points and used AVHRR hotspot data to add observations on the effusion history between the TanDEM-X-based anchor points.

In the following, we discuss the main advantages and limitations of the developed technique. We also highlight potential modifications to our approach that may help alleviate some of the identified limitations.

3.4.2.1 Benefits of the proposed data fusion approach

The proposed combination of AVHRR hotspot and TanDEM-X DEM time series data permits the creation of a temporally dense effusion time series for large effusive eruptions while avoiding saturation-related biases. The combined dataset can reveal detailed observations on the temporal evolution of volcanic activity, and significantly for Tolbachik, the joint dataset provides detailed results on:

- The history of lava emplacement for all geographic locations sampled by our dataset including the identification of high-effusion periods and periods of quiescence.
- Details on the onset and duration of deposition at each image pixel.
- A detailed history of total effused volume including the timing of the beginning and end of effusive activity.
- Time-averaged discharge rates calculated over hours rather than weeks provide new observations on active and passive episodes at Tolbachik that could not be gleaned from previously available data.

The approach developed here can be transferred to other volcanoes known to have large effusive eruptions, if sufficient TanDEM-X coverage is available. The joint dataset may also be used to test if the observed effusive behavior of an eruption deviates from established effusion rate models. For instance, Wadge (1981) analyzed the variation of effusion rates for different basaltic eruptions and concluded that basaltic eruptions very often begin with initial high effusion rates and continue with much lower rates comparable to an exponential flow model,

$$E_r(t) = E_{r\_max} \cdot e^{-\xi t} \tag{3.9}$$

which relates the effusion rate at any time during the eruption ($E_r(t)$), to the maximum lava discharge rate (E_{r_max}), and a decay constant (ξ). Densely sampled effusion observations, such as those provided here for the TFE, can offer important inputs to test effusion models, which may lead to an enhanced characterization of eruption dynamics and magma movement. Decay constants, derived from a model fit to observations, can reveal evidence of reservoir depth, such as deep reservoirs, that tend to have eruptions with slowly waning flows (Wadge, 1981).

3.4.2.2 Limitations of the technique

Our approach is based on a number of assumptions that give rise to its main limitations:

Assumption 1: The available AVHRR hotspot observations provide a true representation of the effusive activity between two TanDEM-X sampling points. This necessarily involves two additional, implicit assumptions:

- The false alarm rate of the hotspot detection method is low, i.e., the effusive activity is correctly represented in the data.
- The temporal sampling provided by valid AVHRR scenes is regular. This assumes that temporal gaps between observations, due to cloud cover or unfavorable imaging geometry, are spread randomly throughout the time series. Extended temporal gaps could lead to a biased representation of effusive activity between TanDEM-X time steps.

We consider the first of these considerations as less critical, as the hotspot detection approach uses a low false alarm rate (Dehn and Harris, 2015), and as residual false alarms should be random in time, which both minimize effects on the shape of the effusion time series.

The assumption of evenly distributed temporal gaps between usable AVHRR observations is of higher importance as neither the appearance of clouds nor the distribution of cloudy data is strictly random in time. Hence, the temporal distribution of AVHRR datasets across our time series (Figure 3.19) was analyzed and shows that, for the TFE, the temporal gaps between observations with potentially erroneous data is log-normally distributed, as would be expected for random variables with small mean and large standard deviations (Limpert et al., 2001). On average, every third AVHRR dataset was found to contain questionable observations due to a combination of shallow observation (scan) angles and local cloud cover. The temporal distribution of missed samples was found to be near random such that the impact of image gaps on effusion rate estimation was minimal for this particular time series.

Assumption 2: All hotspots detected between the consecutive TanDEM-X acquisition times $t_{TDX}(n-1)$ and $t_{TDX}(n)$ contribute equally to the total flow volume that effused between times $t_{TDX}(n-1)$ and $t_{TDX}(n)$.

Violations to this assumption may lead to errors in the reconstructed effusion time series. Even so, the joint effusion time series is required to preserve TanDEM-X measurement points, and errors are thereby contained between TanDEM-X sampling points.

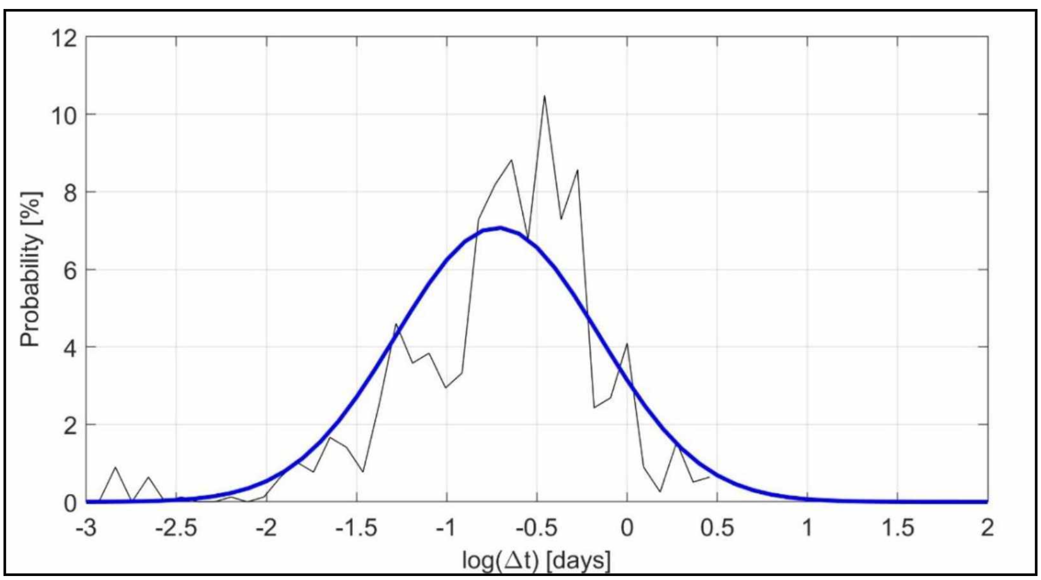

Figure 3.19: Statistical distribution of temporal gaps between missed data samples. The spacing of missed samples closely follows a normal distribution in this linear-log plot. On average, every third AVHRR acquisition contains questionable observations due to low incidence angles or cloud cover.

3.4.2.3 Potential future improvements to the approach

Additional sensors for DEM generation: While TanDEM-X proved to be a first-rate source for DEM generation over active volcanoes, it may be useful to expand to other spaceborne sensors capable of DEM generation. Examples include the strip-processed version of the ArcticDEM (Morin et al., 2016) constructed from in-track and cross-track high-resolution (~0.5 m) imagery acquired by the DigitalGlobe constellation of optical imaging satellites. The strip-processed version is available as multi-temporal layers and could be a suitable candidate for future integration. However, a regular occurrence of temporal gaps in these DEMs would require an approach for data cleanup.

The TanDEM-L constellation, currently in early development at the German Aerospace Center, could be another promising future candidate for DEM data (Eineder et al., 2016). Like TanDEM-X, the TanDEM-L mission is a constellation of two identical sensors where the generation of repeated DEMs is a mission requirement (Tridon et al., 2018). The cloud-independence of this sensor may lead to an availability of regular DEM acquisitions over most volcanic sites of interest.

Additional thermal sensors and channels for hotspot observations: Currently, high-resolution observations of effusion activity are acquired from the AVHRR sensor. With the fleet of available thermal sensors expanding, observations could be expanded to include data from instruments such as Himawari 8 (Bessho et al., 2016); the Geostationary Operational Environmental Satellite –R Series (GOES-R) (Schmit et al., 2005); or the Spinning Enhanced Visible and Infrared Imager (SEVIRI) on board the Meteosat Second Generation (MSG) satellites (Trigo et al., 2008), Using a broader set of sensors for thermal monitoring will lead to improved temporal sampling of effusive events._Currently, thermal information from AVHRR is focused on hotspot detection. This is a practical limitation given the low saturation temperature of AVHRR band 3, particularly for large effusive events such as the TFE.

Use of thermal data could be improved by integrating AVHRR band 4 (λ=10.6μm) into the thermal series analysis, in a manner similar to its use in the Okmok II algorithm. At its longer wavelength, band 4 is less sensitive to variations of surface temperature and is therefore a less frequently used, albeit a less accurate tool for surface temperature estimation. However, its reduced temperature sensitivity also reduces the likelihood of saturation.

In an expansion of our current approach, AVHRR band 4 data could be integrated as a weighting function in Eq. 3.10 to ensure that thermal anomalies associated with higher band 4 temperatures, $T_{10.6\mu}$, contribute more to the overall flow volume increase. This could be achieved by integrating $T_{10.6\mu}$ directly to estimate the contribution ΔF_{HS} of every hotspot to the flow thickness increase between two TanDEM-X acquisition times, e.g.,

$$\left[F\left(t_{TDX}(n)\right) - F\left(t_{TDX}(n-1)\right)\right] = {\sum \Delta F_{HS} \cdot T_{10.6\mu}} \Big/ {\sum T_{10.6\mu}} \tag{3.10}$$

3.5 Conclusion

The TFE on the Kamchatka Peninsula was a significant effusive eruption that lasted nine months, and emplaced volcanic products with a volume reported between 0.53 km³ and 0.65 km³ (0.50 km³ DRE and 0.55 km³ DRE) over an area between 35.9 km² and 45.8 km² (Belousov et al., 2015; Dvigalo et al., 2014; Kubanek et al., 2017; Dai and Howat, 2017). Radiant brightness temperature data were examined from 2569 observations obtained from orbital AVHRR sensors. Although reliable results on the lava flow area from this large scale eruption using the AVHRR data exclusively were not possible, a new approach was developed to combine AVHRR thermal data with a series of DEMs derived from the TanDEM-X radar observations. This approach can lead to a substantial increase in the understanding of the small temporal changes in the volcanic activity and emplaced material across the lava flow extent during the nine-months of the eruption.

Each DEM in the TanDEM-X based time series provided precise elevation differences to derive the flow thickness and effused volume at each TanDEM-X observation time. The DEMs provided highly accurate fine spatial resolution observations, but their temporal resolution was coarse, resulting in only 12 DEMs over the course of the entire nine month eruption. To fill those gaps, thermal anomalies observed by AVHRR sensors, which provide up to four observations per day, were interleaved between the TanDEM-X acquisition times, and interpolated to provide precise estimates on the number and timing of significant effusive periods.

The developed joint time series approach substantially increased the number of observations and hence small temporal variations in the eruptive activity during the nine month TFE and possibly other effusive eruptions. The onset and end of the TFE was clarified and re-defined from the combined series and several periods of relative quiescence and high activity were identified that were not originally recognized from the individual time series analysis. Lava flow development as a function of time and space was analyzed that supported an improved estimate of the effusion history across the approximate nine months of the TFE. In addition to a geophysical analysis of the derived data, several benefits and limitations of the developed approach were identified as well as future directions to improve upon the process to derive even more details on the eruptive cycle and our understanding of these large effusive events.

3.6 Appendix

List of variables used in Section 3, Equations 3.1 -- 3.10

Variable	Description
E_r	Instantaneous lava effusion rate
Q_{tot}	Total thermal flux
ρ	Lava density
C_p	Specific heat capacity
ΔT	Eruption temperature minus solidus
c_L	Latent heat of crystallization
$\Delta\phi$	Crystallization in cooling through ΔT
F_T	Heat loss per unit area
A_T	Area of lava
μ	Mean of a population
σ	Standard deviation of a population
$HS(t)$	Time series of thermal anomalies
$V(t)$	Effused volume at time t_{TDX}
$E_r(t)$	Time series of effusion rates
$B_\perp$	Effective perpendicular baseline
γ	Average interferometric coherence
$\phi_{i,j}$	The InSAR phase calculated from SAR acquisitions *i* and *j;*
$\phi_{i,j,defo}$	The InSAR phase component contributed from surface deformation;
$\phi_{i,j,topo}$	The InSAR phase component contributed from surface topography;
$\phi_{i,j,atm}$	The InSAR phase component contributed from atmospheric propagation properties;
$\phi_{i,j,orbit}$	The InSAR phase component contributed from errors in satellite orbits;

$\phi_{i,j,noise}$	The InSAR phase component contributed from noise;
t_i and t_j	Time at point *i* and *j*, respectively.
$\phi_{i,j}^{TDX}$	The InSAR phase from TanDEM-X SAR acquisitions *i* and *j*;
$\phi_{i,j,topo}^{TDX}$	The InSAR phase component of TanDEM-X SR acquisitions *i* and *j* that are contributed from surface topography;
$\phi_{i,j,orbit}^{TDX}$	The InSAR phase component of TanDEM-X SR acquisitions *i* and *j* that are contributed from errors in satellite orbits;
$\phi_{i,j,noise}^{TDX}$	The InSAR phase component of TanDEM-X SR acquisitions *i* and *j* that are contributed from noise;
$B_{i,j\perp,}^{eff}$	The effective perpendicular baseline corresponding to half of the perpendicular baseline of the bistatic TanDEM-X acquisition geometry.
r	The sensor-to-target range
θ	The look-angle of the satellite-sensor system
λ	Wavelength
h	Surface elevation
ϕ_{pre}	Interferometric phase from the pre-eruption TanDEM-X data pair.
ϕ_{ref_topo}	A interferometric reference phase derived here from SRTM data
φ	Residual phase measurement
φ_{unw}	Residual phase measurement between the SRTM-DEM, and the true pre-eruption topography.
h_{pre}	The TanDEM-X pre-eruption DEM
Δ_h	The difference between two elevations
$\phi_{\Delta h}$	The phase change attributable to Δ_h after correction for orbit errors
h_{pre}	Surface elevation based on the pre-eruption DEM from TanDEM-X
$HS(t)$	A hotspot at time *t*.
$F(t)$	Flow thickness at observation time t_{TDX}

$F_{res}(t)$	Flow thickness time series resampled into AVHRR geometry
ΔF_{res}	The difference in flow thickness between two acquisition times
$t_{TDX}(n)$	A TanDEM-X acquisition time at time step *n*.
σ_{Fres}	Height error of the resampled flow thickness
σ_F	Height error of flow thickness before resampling
m	AVHRR/TanDEM-X resolution ratio
t_{AVHRR}	All AVHRR acquisition times
$F_{AVHRR+TDX}(t)$	Flow thickness of the joint time series at time *t*
N	The total number of TanDEM-X acquisition points *tTDX*
$\Delta F_{HS}(n)$	Additional flow thickness added at each hotspot *n*
k_{HS}	The number of thermal anomalies between two consecutive time steps
$E_{r\ max}$	The maximum instantaneous lava discharge rate
ξ	A decay constant over the course of an effusive eruption

3.7 References

Belousov, A., Belousova, M., Edwards, B., Volynets, A., and Melnikov, D., 2015, Overview of the precursors and dynamics of the 2012–13 basaltic fissure eruption of Tolbachik Volcano, Kamchatka, Russia: Journal of Volcanology and Geothermal Research, v. 307, p. 22-37, doi: 10.1016/j.jvolgeores.2015.06.013.

Bessho, K., Date, K., Hayashi, M., Ikeda, A., Imai, T., Inoue, H., Kumagai, Y., Miyakawa, T., Murata, H., and Ohno, T., 2016, Journal of the Meteorological Society of Japan, v. 94, p. 151-183, doi: 10.2151/jmsj.2016-00.

Chen, C.W., and Zebker, H.A., 2002, Phase unwrapping for large SAR interferograms: Statistical segmentation and generalized network models: IEEE Transactions on Geoscience and Remote Sensing, v. 40, p. 1709-1719, doi: 10.1109/TGRS.2002.802453

Churikova, T., Gordeychik, B., Edwards, B.R., Ponomareva, V.V., and Zelenin, E.A., 2015, The Tolbachik volcanic massif: A review of the petrology, volcanology and eruption history prior to the 2012-2013 eruption: Journal of Volcanology and Geothermal Research, v. 307, p. 3-21, doi: 10.1016/j.jvolgeores.2015.10.016

Dai, C., and Howat, I.M., 2017, Measuring Lava Flows With ArcticDEM: Application to the 2012–2013 Eruption of Tolbachik, Kamchatka: Geophysical Research Letters, v. 44, p. 12,133-12,140, doi: 10.1002/2017gl075920.

Dean, K., Servilla, M., Roach, A., Foster, B., and Engle, K., 1998, Satellite monitoring of remote volcanoes improves study efforts in Alaska: Eos, Transactions American Geophysical Union, v. 79, p. 413-423, doi: 10.1029/98EO00316.

Dean, K.G., Dehn, J., Engle, K., Izbekov, P., Papp, K.R., and Patrick, M.R., 2002, Operational satellite monitoring of volcanoes at the Alaska Volcano Observatory: Advances in Environmental Monitoring and Modeling, v. 1, p. 70-97.

Dehn, J., Dean, K., and Engle, K., 2000, Thermal monitoring of North Pacific volcanoes from space: Geology, v. 28, p. 755-758, doi: 10.1130/0091-7613(2000)28<755:tmonpv>2.0.co;2.

Dehn, J., Dean, K.G., Engle, K., and Izbekov, P., 2002, Thermal precursors in satellite images of the 1999 eruption of Shishaldin Volcano: Bulletin of Volcanology, v. 64, p. 525-534, doi: 10.1007/s00445-002-0227-0.

Dehn, J., and Harris, A.J.L., 2015, Thermal anomalies at volcanoes, *in* Dean, K.G., and Dehn, J., eds., Monitoring volcanoes in the North Pacific: observations from space: Berlin, Springer-Verlag, pp. 49-78, doi: 10.1007/978-3-540-68750-4_3.

Diefenbach, A., Bull, K.F., Wessels, R.L., and McGimsey, R., 2013, Photogrammetric monitoring of lava dome growth during the 2009 eruption of Redoubt Volcano: Journal of Volcanology and Geothermal Research, v. 259, p. 308-316, doi: 10.1016/j.jvolgeores.2011.12.009.

Diefenbach, A.K., Crider, J.G., Schilling, S.P., and Dzurisin, D., 2012, Rapid, low-cost photogrammetry to monitor volcanic eruptions: an example from Mount St. Helens, Washington, USA: Bulletin of Volcanology, v. 74, p. 579-587, doi: 10.1007/s00445-011-0548-y.

Dozier, J., 1980, Satellite identification of surface radiant temperature fields of subpixel resolution: NOAA Technical memorandum NESS 113, NOAA, Washington, DC, 11 pp.

—, 1981, A method for satellite identification of surface temperature fields of subpixel resolution: Remote Sensing of Environment, v. 11, p. 221-229.

Dvigalo, V.N., Svirid, I.Y., and Shevchenko, A.V., 2014, The first quantitative estimates of parameters for the Tolbachik Fissure Eruption of 2012–2013 from aerophotogrammetric observations: Journal of Volcanology and Seismology, v. 8, p. 261-268, doi: 10.1134/s0742046314050029.

Ebmeier, S.K., Biggs, J., Mather, T.l., Elliott, J.R., Wadge, G., and Amelung, F., 2012, Measuring large topographic change with InSAR; lava thicknesses, extrusion rate, and subsidence rate at Santiaguito Volcano, Guatemala: Earth and Planetary Science Letters, p. 216-225, doi: 10.1016/j.epsl.2012.04.027.

Eineder, M., Hajnsek, I., Krieger, G., Moreira, A., and Papathanassiou, K., 2016, Tandem-L: satellite mission proposal for monitoring dynamic processes on the Earth's surface, German Aerospace Center (Deutsches Zentrum für Luft- und Raumfahrt e.V.), Cologne, 28 pp.

Farr, T.G., Rosen, P.A., Caro, E., Crippen, R., Duren, R., Hensley, S., Kobrick, M., Paller, M., Rodriguez, E., Roth, L., Seal, D., Shaffer, S., Shimada, J., Umland, J., Werner, M., Oskin, M., Burbank, D., and Alsdorf, D., 2007, The shuttle radar topography mission: Review of Geophysics, v. 45, p. 1-33, doi: 10.1029/2005RG000183.

Fedotov, S., Utkin, I., and Utkina, L., 2011, The peripheral magma chamber of Ploskii Tolbachik, a Kamchatka basaltic volcano: Activity, location and depth, dimensions, and their changes based on magma discharge observations: Journal of Volcanology and Seismology, v. 5, p. 369-385, doi: 10.1134/S0742046311060042

Fedotov, S.A., Chirkov, A.M., Gusev, N.A., Kovalev, G.N., and Slezin, Y.B., 1980, The large fissure eruption in the region of Plosky Tolbachik Volcano in Kamchatka, 1975–1976: Bulletin of Volcanology, v. 43, p. 47-60, doi: 10.1007/bf02597610.

Ferretti, A., 2014, Satellite InSAR data: Reservoir monitoring from space: The Netherlands, EAGE Publications bv, 159 pp.

Gordeev, E., Muravyov, Y.D., Samoylenko, S., Volynets, A., Melnikov, D., Dvigalo, V., and Melekestsev, I., 2013, First results from the 2012-2013 Tolbachik fissure eruption: Bulletin of the Volcanological Society of Japan, v. 58, p. 1-8.

Harris, A.J., Flynn, L.P., Rothery, D.A., Oppenheimer, C., and Sherman, S.B., 1999, Mass flux measurements at active lava lakes: implications for magma recycling: Journal of Geophysical Research: Solid Earth, v. 104, p. 7117-7136, doi: 10.1029/98JB02731.

Harris, A.J.L., 2013, Thermal remote sensing of active volcanoes: a users manual, 1st ed.: Cambridge, UK, Cambridge University Press, 728 pp.

Harris, A.J.L., Blake, S., Rothery, D.A., and Stevens, N.F., 1997a, A chronology of the 1991 to 1993 Mount Etna eruption using advanced very high resolution radiometer data: Implications for real-time thermal volcano monitoring: Journal of Geophysical Research: Solid Earth, v. 102, p. 7985-8003, doi: 10.1029/96jb03388.

Harris, A.J.L., Dehn, J., and Calvari, S., 2007, Lava effusion rate definition and measurement: a review: Bulletin of Volcanology, v. 70, p. 1-22, doi: 10.1007/s00445-007-0120-y.

Harris, A.J.L., Flynn, L.P., Keszthelyi, L., Mouginis-Mark, J.P., Rowland, K.S., and Resing, A.J., 1998, Calculation of lava effusion rates from Landsat TM data: Bulletin of Volcanology, v. 60, p. 52-71, doi: 10.1007/s004450050216.

Harris, A.J.L., Murray, J.B., Aries, S.E., Davies, M.A., Flynn, L.P., Wooster, M.J., Wright, R., and Rothery, D.A., 2000, Effusion rate trends at Etna and Krafla and their implications for eruptive mechanisms: Journal of Volcanology and Geothermal Research, v. 102, p. 237-269, doi: 10.1016/S0377-0273(00)00190-6.

Harris, A.J.L., Rothery, D.A., Carlton, R.W., Langaas, S., and Mannstein, H., 1995, Non-zero saturation of AVHRR thermal channels over high temperature targets: evidence from volcano data and a possible explanation: International Journal of Remote Sensing, v. 16, p. 189-196, doi: 10.1080/01431169508954388.

Harris, L.A.J., Butterworth, L.A., Carlton, W.R., Downey, I., Miller, P., Navarro, P., and Rothery, A.D., 1997b, Low-cost volcano surveillance from space: case studies from Etna, Krafla, Cerro Negro, Fogo, Lascar and Erebus: Bulletin of Volcanology, v. 59, p. 49-64, doi: 10.1007/s004450050174.

Jackson, J.A., *ed.*, 1997, Glossary of Geology, 4th edition: Alexandria, Virginia, American Geological Institute, 769 p.

Jiang, G., Zhao, D., and Zhang, G., 2009, Seismic tomography of the Pacific slab edge under Kamchatka: Tectonophysics, v. 465, p. 190-203, doi: 10.1016/j.tecto.2008.11.019.

Kennedy, P.J., Belward, A.S., and Gregoire, J.M., 1994, An improved approach to fire monitoring in West Africa using AVHRR data: International Journal of Remote Sensing, v. 15, p. 2235-2255, doi: 10.1080/01431169408954240.

Kidwell, K.B., 1991, NOAA polar orbiter data users guide (TIROS-N, NOAA-6, NOAA-7, NOAA-8, NOAA-9, NOAA-10, NOAA-11, NOAA-12, NOAA-13, and NOAA-14). NOAA POD Guide, National Oceanic and Atmospheric Administration, Washington, DC, 307 pp.

Kostylev, V.I., 2007, Different types of radar systems, chapter 9, *in* Cherniakov, M., ed., Bistatic Radar: Principles and Practice: West Sussex, John Wiley & Sons, Ltd., pp. 189-192, doi: 10.1002/9780470035085.

Krieger, G., Moreira, A., Fiedler, H., Hajnsek, I., Werner, M., Younis, M., and Zink, M., 2007, TanDEM-X: A satellite formation for high-resolution SAR interferometry: IEEE Transactions on Geoscience and Remote Sensing, v. 45, p. 3317-3341, doi: 10.1109/TGRS.2007.900693.

Kubanek, J., Richardson, J.A., Charbonnier, S.J., and Connor, L.J., 2015, Lava flow mapping and volume calculations for the 2012–2013 Tolbachik, Kamchatka, fissure eruption using bistatic TanDEM-X InSAR: Bulletin of Volcanology, v. 77, p. 1-13 (on-line version), doi: 10.1007/s00445-015-0989-9.

Kubanek, J., Westerhaus, M., and Heck, B., 2013, On the use of bistatic TanDEM-X images to quantify volumetric changes of active lava domes: International Association of Geodesy, Scientific Assembly 150th Anniversary of the IAG, Book of Abstracts, Book of Abstracts, p. 202, doi: 10.1007/1345_2015_172.

Kubanek, J., Westerhaus, M., and Heck, B., 2017, TanDEM-X time series analysis reveals lava flow volume and effusion rates of the 2012–2013 Tolbachik, Kamchatka fissure eruption: Journal of Geophysical Research: Solid Earth, v. 122, p. 1-21, doi: 10.1002/2017JB014309.

KVERT, 2019, "About KVERT", Kamchatka Volcanic Eruption Response Team (ed.). Institute of Volcanology and Seismology, Petropavlovsk-Kamchatsky, http://www.kscnet.ru/ivs/kvert/about_eng, accessed 20 February 2019.

Lauritson, L., Nelson, G., and Porto, F., 1979, Techniques for data extraction and calibration of TIROS-N/NOAA series satellite radiometers, NOAA-Technical Memorandum NESS 107, NOAA, Washington, DC, 77 pp.

Lautze, N.C., Harris, A.J.L., Bailey, J.E., Ripepe, M., Calvari, S., Dehn, J., Rowland, S.K., and Evans-Jones, K., 2004, Pulsed lava effusion at Mount Etna during 2001: Journal of Volcanology and Geothermal Research, v. 137, p. 231-246, doi: 10.1016/j.jvolgeores.2004.05.018

Levin, V., Shapiro, N., Park, J., and Ritzwoller, M., 2002, Seismic evidence for catastrophic slab loss beneath Kamchatka: Nature, v. 418, p. 763, doi: 10.1038/nature00973.

Limpert, E., Stahel, W., A., and Abbt, M., 2001, Log-normal distributions across the sciences: keys and clues: BioScience, v. 51, p. 341-352, doi: 10.1641/0006-3568(2001)051[0341:LNDATS]2.0.CO;2.

Matson, M., and Dozier, J., 1981, Identification of subresolution high temperature sources using a thermal IR sensor: Photogrammetric engineering and remote sensing, v. 47, p. 1311-1318.

McAlpin, D., Meyer, F., Gong, W., Beget, J., and Webley, P., 2017, Pyroclastic flow deposits and InSAR: analysis of long-term subsidence at Augustine Volcano, Alaska: Remote Sensing, v. 9, p. 4, doi: 10.3390/rs9010004.

Melnikov, D., and Volynets, A.O., 2015, Remote sensing and petrological observations on the 2012–2013 fissure eruption at Tolbachik Volcano, Kamchatka: Implications for reconstruction of the eruption chronology: Journal of Volcanology and Geothermal Research, v. 307, p. 89-97, doi: 10.1016/j.jvolgeores.2015.09.025.

Morin, P., Porter, C., Cloutier, M., Howat, I., Noh, M.-J., Willis, M., Bates, B., Williamson, C., and Peterman, K., 2016, ArcticDEM; a publically available, high resolution elevation model of the Arctic, EPSC2016-8396, presented at the EGU General Assembly 2016, vol. 18, Vienna, Austria, 17-22 April 2016, pp.

Naranjo, M.F., Ebmeier, S.K., Vallejo, S., Ramón, P., Mothes, P., Biggs, J., and Herrera, F., 2016, Mapping and measuring lava volumes from 2002 to 2009 at El Reventador Volcano, Ecuador, from field measurements and satellite remote sensing: Journal of Applied Volcanology, v. 5, p. 8, doi: 10.1186/s13617-016-0048-z.

NOAA, 2017, "POES operational status", Last modified 27 January 2017, NOAA Office of Satellite and Product Operations, National Environmental Satellite, Data, and Information Service, https://www.ospo.noaa.gov/Operations/POES/status.html, accessed 16 January 2019.

Oppenheimer, C., 1991, Lava flow cooling estimated from Landsat Thematic Mapper infrared data: the Lonquimay eruption (Chile, 1989): Journal of Geophysical Research: Solid Earth, v. 96, p. 21865-21878, doi: 10.1029/91JB01902

Oppenheimer, C., 1998, Review article: volcanological applications of meteorological satellites: International Journal of Remote Sensing, v. 19, p. 2829-2864, doi: 10.1080/014311698214307.

Oppenheimer, C., Brancis, P.W., Rotherery, D.A., Carlton, R.W.T., and Glaze, L.S., 1993, Infrared image analysis of volcanic thermal features: Láscar Volcano, Chile, 1984-1992: Journal of Geophysical Research: Solid Earth, v. 98, p. 4269-4286, doi: 10.1029/92JB02134.

Pieri, D.C., and Baloga, S.M., 1986, Eruption rate, area, and length relationships for some Hawaiian lava flows: Journal of Volcanology and Geothermal Research, v. 30, p. 29-45, doi: 10.1016/0377-0273(86)90066-1.

Poland, M.P., 2014, Time-averaged discharge rate of subaerial lava at Kilauea Volcano, Hawai ‘i, measured from TanDEM-X interferometry: Implications for magma supply and storage during 2011–2013: Journal of Geophysical Research: Solid Earth, v. 119, p. 5464-5481, doi: 10.1002/2014JB011132.

Prata, A., Caselles, V., Coll, C., Sobrino, J., and Ottle, C., 1995, Thermal remote sensing of land surface temperature from satellites: Current status and future prospects: Remote Sensing Reviews, v. 12, p. 175-224, doi: 10.1080/02757259509532285.

Ramsey, M.S., 2016, Synergistic use of satellite thermal detection and science: a decadal perspective using ASTER, *in* Harris, A.J.L., DeGroeve, T., Garel, F., and Carn, S.A., eds., Detecting, modelling and responding to effusive eruptions, Special Publication 426 Volume 426, Geological Society, London, pp. 115-136, doi: 10.1144/sp426.23.

Robel, J., and Graumann, A., *eds.*, 2014, NOAA KLM user's guide with NOAA-N, N Prime, and MetOp supplements: Asheville, NC, USA, National Oceanic and Atmospheric Administration, National Environmental Satellite, Data, and Information Service, National Climatic Data Center, 2530 p.

Roth, A., 2003, TerraSAR-X: a new perspective for scientific use of high resolution spaceborne SAR data, *in* Proceedings, 2nd GRSS/ISPRS Joint Workshop on Remote Sensing and Data Fusion over Urban Areas, Berlin, Germany, 22-23 May 2003, pp. 4-7, IEEE, doi: 10.1109/dfua.2003.1219947.

Rothery, D.A., 1992, Monitoring and warning of volcanic eruptions by remote sensing, chapter 4, *in* McCall, G.J.H., Laming, D.J.C., and Scott, S.C., eds., Geohazards: London, Chapman & Hall, pp. 25-32, doi: 10.1007/978-94-009-0381-4_4

Rothery, D.A., Francis, P.W., and Wood, C.A., 1988, Volcano monitoring using short wavelength infrared data from satellites: Journal of Geophysical Research, v. 93, p. 7993-8008, doi: 10.1029/JB093iB07p07993.

Schilling, S.P., Thompson, R.A., Messerich, J.A., and Iwatsubo, E., 2008, Use of digital aerophotogrammetry to determine rates of lava dome growth, Mount St. Helens, Washington, *in* Sherrod, D.R., Scott, W.E., and Stauffer, P.H., eds., A Volcano Rekindled: The Renewed Eruption From Mount St. Helens, 2004–2006: USGS Professional Paper 1750, p. 145-167.

Schmit, T.J., Gunshor, M.M., Menzel, W.P., Gurka, J.J., Li, J., and Bachmeier, A.S., 2005, Introducing the next-generation Advanced Baseline Imager on GOES-R: Bulletin of the American Meteorological Society, v. 86, p. 1079-1096, doi: 10.1175/BAMS-86-8-1079.

Schneider, D.J., Dean, K.G., Dehn, J., Miller, T.P., and Kirianov, V.Y., 2000, Monitoring and analyses of volcanic activity using remote sensing data at the Alaska Volcano Observatory: case study for Kamchatka, Russia, December 1997, *in* Mouginis-Mark, P.J., Crisp, J.A., and Fink, J.A., eds., Remote Sensing of Active Volcanism: Washington, DC, American Geophysical Union, pp. 65-85.

Senyukov, S.L., Nuzhdina, I.N., Droznina, S.Y., Garbuzova, V.T., Kozhevnikova, T.Y., Sobolevskaya, O.V., Nazarova, Z.A., and Bliznetsov, V.E., 2015, Reprint of "Seismic monitoring of the Plosky Tolbachik eruption in 2012–2013 (Kamchatka Peninsula Russia)": Journal of Volcanology and Geothermal Research, v. 307, p. 47-59, doi: 10.1016/j.jvolgeores.2015.07.026.

Stevens, N., Wadge, G., and Murray, J., 1999, Lava flow volume and morphology from digitised contour maps: a case study at Mount Etna, Sicily: Geomorphology, v. 28, p. 251-261, doi: 10.1016/S0169-555X(98)00115-9.

Stevens, N., Wadge, G., and Williams, C., 2001, Post-emplacement lava subsidence and the accuracy of ERS InSAR digital elevation models of volcanoes: International Journal of Remote Sensing, v. 22, p. 819-828, doi: 10.1080/01431160051060246.

Stewart, R.H., 1985, Methods of satellite oceanography: Berkeley, University of California Press, 360 pp.

Tapakis, R., and Charalambides, A.G., 2013, Equipment and methodologies for cloud detection and classification: A review: Solar Energy, v. 95, p. 392-430, doi: 10.1016/j.solener.2012.11.015.

Tridon, D.B., Sica, F., De Zan, F., Bachmann, M., and Krieger, G., 2018, Observation Strategy and Flight Configuration for Monitoring Earth Dynamics with the Tandem-L Mission, *in* Proceedings, IGARSS 2018-2018 IEEE International Geoscience and Remote Sensing Symposium, Valencia, pp. 5651-5654, doi: 10.1109/IGARSS.2018.8517757

Trigo, I.F., Peres, L.F., DaCamara, C.C., and Freitas, S.C., 2008, Thermal land surface emissivity retrieved from SEVIRI/Meteosat: IEEE Transactions on Geoscience and Remote Sensing, v. 46, p. 307-315, doi: 10.1109/TGRS.2007.905197.

Trischenko, A.P., Fedosejevs, G., Li, Z., and Cihlar, J., 2002, Trends and uncertainties in thermal calibration of AVHRR radiometers onboard NOAA-9 to NOAA-16: Journal of Geophysical Research, v. 107, p. 1-13, doi: 10.1029/2002JD002353.

Tukey, J.W., 1977, Exploratory data analysis: Reading Massachusetts, Addison-Wesley Publishing Company, 688 pp.

USGS, 2018, "USGS EROS Archive - Advanced Very High Resolution Radiometer", US Geological Survey, Earth Resources Observation and Science (EROS) Center, Reston, Virginia, https://www.usgs.gov/centers/eros/science/usgs-eros-archive-advanced-very-high-resolution-radiometer-avhrr?qt-science_center_objects=0#qt-science_center_objects, accessed 20 February 2019.

van Manen, S.M., Dehn, J., and Blake, S., 2010a, Satellite thermal observations of the Bezymianny lava dome 1993-2008: Precursory activity, large explosions, and dome growth: J. Geophys. Res., v. 115, p. B08205, doi: 10.1029/2009jb006966.

van Manen, S.M., Dehn, J., West, M.E., Blake, S., and Rothery, D.A., 2010b, the 2006 eruption of Augustine Volcano -- combined analyses of thermal satellite data and reduced displacement, *in* Power, J.A., Coombs, M.L., and Freymueller, J., eds., The 2006 eruption of Augustine Volcano, Alaska: USGS Professional Paper 1769, p. 553-567.

Wadge, G., 1981, The variation of magma discharge during basaltic eruptions: Journal of Volcanology and Geothermal Research, v. 11, p. 139-168, doi: 10.1016/0377-0273(81)90020-2.

Wadge, G., 2003, Measuring the rate of lava effusion by InSAR, *in* Proceedings, FRINGE 2003 Workshop ESA SP-550, vol. 34, Frascati, Italy, 1-5 December 2003, pp. 1-5.

Wiesnet, D., and D'Aguanno, J., 1982, Thermal imagery of Mount Erebus from the NOAA-6 satellite: Antarctic Journal of the United States, v. 17, p. 32-34.

Williams Jr., R.S., and Friedman, J.D., 1970, Satellite observation of effusive volcanism: British Interplanetary Society Journal, v. 23, p. 441-450.

Wright, R., Blake, S., Harris, A.J.L., and Rothery, D.A., 2001, A simple explanation for the space-based calculation of lava eruption rates: Earth and Planetary Science Letters, v. 192, p. 223-233, doi: 10.1016/S0012-821X(01)00443-5.

Wright, R., and Flynn, L.P., 2003, On the retrieval of lava-flow surface temperatures from infrared satellite data: Geology, v. 31, p. 893-896, doi: 10.1130/G19645.1.

Zelenski, M., Malik, N., and Taran, Y., 2014, Emissions of trace elements during the 2012–2013 effusive eruption of Tolbachik Volcano, Kamchatka: enrichment factors, partition coefficients and aerosol contribution: Journal of Volcanology and Geothermal Research, v. 285, p. 136-149, doi: 10.1016/j.jvolgeores.2014.08.007.

Conclusion

Volcanoes are one of the most destructive natural forces on Earth. Human populations have, for centuries, been attracted to the flanks of volcanoes for the mineral-rich volcanic ash that first supported crops for cultivation, then grasslands for husbandry, and later tourism, jobs, and the economies of the cities and human populations that grew up around them. It could be said that volcanoes are to humans, what the Sirens were to Odysseus: appealing on the surface, but ultimately destructive. In 2015, about 58 million people lived within a 10 km radius of roughly 1300 Holocene volcanoes, 200 million live within a 30 km radius, and more than 11% of the world's 6.5 billion people live within 100 km of a Holocene volcano (Siebert et al., 2015). With the benefits of living with volcanoes come real dangers, and in a variety of forms: explosions, toxic gases, pyroclastic flows, lava, ash, and lahars. So the ubiquitous presence of volcanoes, and the populations that live near them present a strong incentive to improve our understanding of the underlying processes of volcanic activity, and by extension, maximize forecast and mitigation effectiveness.

With that broad objective in mind, this three chapter dissertation research focused on improving volcanic observation and, more specifically, the detection, and monitoring of volcanic deposits using novel remote sensing techniques to combine information from visible, thermal, and microwave instruments.

Chapter 1

High-resolution optical images were combined with L-band synthetic aperture radar (SAR) data to produce geophysical measurements at Redoubt Volcano, Alaska during its 2009 eruption. This research study acquired simultaneous forward-, nadir-, and rear-looking optical images, or "triplets," of Redoubt Volcano and the Drift River Valley from the Panchromatic Remote

Sensing Instrument for Stereo Mapping (PRISM) instrument aboard Japan's Advanced Land Observing Satellite (ALOS). At the same time, repeat-pass, L-band SAR data from the Drift River Valley were acquired by the Phased Array type L-band Synthetic Aperture Radar (PALSAR), also orbiting aboard ALOS. Optical PRISM triplets were used to produce high-resolution photogrammetric digital elevation models (DEMs) of Redoubt Volcano and the Drift River Valley to examine topographic changes caused by lahar deposits and scour, and to estimate the volume of the Redoubt lava dome produced during its 2009 eruption. PRISM DEMs were also used with PALSAR data and differential InSAR (d-InSAR) processing to improve the correction of topographic phase components in PALSAR d-InSAR data and increase the accuracy with which eruption-related surface deformation could be measured at Redoubt. Finally, a new algorithm was developed to map boundaries of lahar deposits using coherence maps with PALSAR data. The unique algorithm takes full advantage of all available coherence information in several syneruptive InSAR pairs to reduce noise and false alarms in automatic lahar mask creation.

A number of geophysical findings were possible from the remote sensing techniques developed in this chapter. Elevation difference data at Redoubt Volcano's summit crater revealed an almost 200 m reduction in elevation from the evacuation of accumulated snow and ice during the explosive phase of the eruption (March and April 2009), while the 7 km-long Drift Glacier, on the volcano's north flank, suffered an elevation loss of ~100 m from ice melt and scour. Growth of the final dome began on 4 April 2009, and continued until the end of the eruption on 1 July 2009, reaching an elevation increase of ~200 m over ~850 horizontal meters, and an estimated volume of 7.2×10^6 m³. Even with uncertainties in calculating the geometric shape of the final dome, the total volume compares well with other values from (Bull, 2009; Dehn, J., pers. comm., 2012); Bull and Buurman, 2013; Diefenbach et al., 2013).

Given the amount of ice in the Drift Glacier and the volcano's summit crater, the explosive phase of the eruption caused a number of lahars, beginning where the Drift Glacier terminates in a piedmont lobe at the eastward flowing Drift River. A narrow gorge at the base of the Drift Glacier exhibited scouring of up to 20 m, attributed to lahars from 23 March 2012 (Waythomas et al., 2013), as well as localized zones of lahar deposition up to 20 m slightly downstream and east of the Drift Glacier's piedmont lobe. The data collected over the volcano and its deposits indicate lahar deposition of 0.5 – 2.5 m over a preponderance of the 37-km valley with a mean elevation increase of 1.5 m between the piedmont lobe and the Drift River Delta.

The developed approach, for combining ALOS PRISM and ALOS PALSAR sensors, was found to be highly beneficial to derive cm-scale surface deformation rates at Redoubt Volcano. A performance evaluation, using regions with known surface deformation, showed that the proposed combinatory method led to a significant reduction of bias (μ = 2 cm yr^{-1}), and a significant improvement in accuracy (σ = 1.8 cm yr^{-1}), when compared to standard techniques (μ = 10.5 cm yr^{-1} and σ = 4.2 cm yr^{-1}).

The surface deformation measurements, derived with the developed method, were of sufficient accuracy to confirm that compaction and evaporation of interstitial water in fresh lahar deposits gives rise to surface subsidence. In the lahar-covered areas of the Drift River valley, surface deformations between 0.5 cm yr^{-1} and 20 cm yr^{-1} were recorded. InSAR data additionally suggested that thicker lahar deposits result in higher surface deformation rates. Higher deformation rates were found where the lahar flow thickened as it filled depressions or encountered topographic relief. This suggests that InSAR-derived surface deformation measurements may be useful to derive lahar flow thickness and deposition volume information at active volcanoes, even if no repeated DEM data is available. This hypothesis was later tested in Chapter 2, using Augustine Volcano, Alaska as a test site.

The combination of multi-temporal syneruptive InSAR coherence maps resulted in accurate and reliable measurements of lahar flow extent at Redoubt Volcano, Alaska. As the coherence-based SAR approach is effective in all weather and illumination conditions, the developed technique has the potential to improve the reliability and timeliness of volcanic information, especially for volcanoes with sparse in situ data and regular cloud coverage. Our approach also lends itself to the analysis of flow progression for eruptions of longer duration.

Chapter 2

In this chapter, an analysis of long-term subsidence of pyroclastic flow deposits at Augustine Volcano in South Central Alaska was performed. The objective of this work was to record interferometric measurement of surface deformation from pyroclastic flow deposits (PFDs) at Augustine Island, which included deformation of PFDs laid down by Augustine's volcanic eruption in 2006, plus a second component of deformation contributed by underlying PFDs from a previous eruption in 1986.

As the two eruptions occurred twenty years apart, data collection for this research required multiple SAR platforms. No permanent spaceborne SAR system existed during the 1986 eruption, and no single platform was in use for the entirety of the twenty intervening years. To maximize available coverage, 48 SAR single look complex (SLC) images were acquired between 21 June 1992 and 9 October 2010. The images came from four platforms, using SAR sensors acquiring in C-band and L-band wavelengths (λ). C-band data were obtained from

Radarsat-1 (λ = 5.6 cm), ERS-1, and ERS-2 (both λ = 5.66 cm); while the L-band data (λ = 23.62 cm) for this research were acquired by ALOS-PALSAR.

At Augustine Volcano, SAR data suitable for interferometry were available from June 1992 to October 2005 (ERS-1 and ERS-2), from March 2006 to April 2007 (Radarsat-1), and from July 2007 to October 2010 (ALOS-PALSAR). Using these data in combination with geophysical models, deformation rates were projected back to the pre-SAR periods from 1986 to 1992 to estimate original thickness and long-term subsidence rates for PFDs related to Augustine Volcano's two most recent eruptions in 1986 and 2006.

To discriminate between contributions from these two eruptions, a simplified geophysical model was developed that first assumed the contraction behavior of 1986 and 2006 deposits was based on the same physical principles and same material parameters for each layer of deposits. The model considered four geophysical sources of deformation: (1) surface deflation due to loss of volatiles; (2) surface inflation or deflation caused by volume changes in the magma reservoir; (3) poroelastic deformation caused by loading; and (4) thermoelastic surface deformation due to cooling. Of these four mechanisms, only two, poroelastic deformation from loading, and thermoelastic cooling, were found significant.

A linear model of deformation in each data stack was found to have no significant improvement over an exponential decay model. Subsequent least-squares estimation showed that pyroclastic flows deformation increases linearly with flow thickness, confirming our suspicion from Chapter 1 that InSAR-derived deformation data can be used to estimate the thickness and volume of volcanic deposits. For the pyroclastic flows at Augustine Volcano, a thermal contraction rate of 0.091 cm y^{-1} m^{-1} ± 0.0002 cm y^{-1} m^{-1}, and a poroelastic contraction rate of 0.319 cm y^{-1} m^{-1} ± 0.0005 cm y^{-1} m^{-1} was found. Interestingly, these values are in good agreement with contraction parameters for basaltic and andesitic lava flows that were calculated by Ebmeier et al. (2012), from a limited set of global measurements. This similarity provides an independent validation of our method and gives credence to our results.

With these contraction parameters established, estimates of thickness and volume of deposits for 1986 and 2006 were possible. The model results and InSAR observations resulted in an estimated total volume of PFDs from Augustine Volcano's 2006 eruption of 3.3×10^7 m³ ± 0.11×10^7 m³. Maximum thicknesses were determined at ~31 m, with a mean thickness of ~5 m. Volume of 1986 PFDs were estimated at 4.6×10^7 m³ ± 0.62×10^7 m³, with a maximum thickness of ~31.5 m, and a mean thickness of ~7.4 m. As far as could be determined, these estimated values for 1986 represent the only published thickness distribution map prepared for Augustine Volcano's 1986 eruption.

Chapter 3

In the last of three chapters, a new method was developed to combine thermal and SAR remote sensing data to expand the possible number and precision of effusion observations that can be extracted from the individual datasets when processed alone. For this purpose, thermal data was obtained from a constellation of NOAA satellites with Advanced Very High Resolution Radiometer (AVHRR) sensors, and SAR data from the German Aerospace Center's TanDEM-X SAR mission. These two sources were complimentary because two AVHRR satellites, each with a twelve hour revisit period, resulted in several passes per day, but at a ground resolution of only 1.1 km, while the TanDEM-X, on the other hand, has a minimum revisit period of at least 11 days, but provides meter level spatial resolution. The complementarity of high-temporal but low-spatial resolution AVHRR and low-temporal but high-spatial resolution TanDEM-X data, suggested that a combination of the two sensors may result in an improved eruption profile that could not be achieved by either dataset on their own.

The target for this work was the 2012–2013 Tolbachik Fissure Eruption (TFE), which occurred at Tolbachik Volcano, on the Kamchatka Peninsula, from 27 November 2012 through ~27 August 2013. An initial analysis of contemporaneous AVHRR observations of Tolbachik Volcano made by the Alaska Volcano Observatory revealed significant saturation issues during the course of the eruption, but especially during the dynamic initial stage, when up to 90% of the available observations contained saturated pixels in the mid-infrared band (3.550 μm –3.93 μm), and at least 1188 of the 2569 total observations (46%) contained saturated pixels.

To minimize the impacts of saturation on effusion rate estimates derived from AVHRR alone, this work developed an alternative combinatory approach to effusion rate analysis. From the AVHRR sensor, the approach relied only on the number of pixels revealed to have an anomalous surface temperature in AVHRR data. This approach removed the necessity to derive actual surface temperatures, and also obviated the saturation issue. However, the existence and quantity of thermal anomalies (also called hotspots) became important. With the largely effusive nature of the TFE, thermally anomalous pixels could be assumed to represent lava, whose origin was effusion.

For thickness observations, DEM differencing from interferometric TanDEM-X InSAR data was used. Using interferometric phase information from TanDEM-X, a time series of twelve, high-resolution DEMs was created. When evaluated for temporal differences, the DEMs provided accurate, high spatial-resolution maps of changes in topography during the course of the eruption, i.e., highly reliable estimates of effusive volume.

A novel approach consisting of three primary processing steps was developed to combine AVHRR- and TanDEM-X-based observations. First, AVHRR and TanDEM-X data were resampled to the same reference frame and onto the same geospatial raster, with the AVHRR observation geometry chosen as the reference geometry. A second step identified and corrected occasional mis-registrations of AVHRR observations that typically originate from geolocation errors when AVHRR observations are acquired at a shallow scan angle; i.e., when Tolbachik Volcano is near the western edge of the swath width. In a final step, the two datasets were combined to produce unbiased and fine temporal resolution effusion observations at Tolbachik Volcano. To merit bias-free results, temporally sparse TanDEM-X-based effusion volume estimates are used as reference points to guide an interpolation approach that used AVHRR data to fill gaps between TanDEM-X acquisition times. Figure 3.13 shows a comparison of thermal anomaly time series to reported eruption chronology for the dynamic initial stage of the eruption, and provides evidence for this claim. The good correspondences give credence to the derived hotspot observations and support the developed approach, which uses hotspot data for interpolating flow thickness, volume, and effusion rate information.

The developed approach and available data resulted in a more detailed time series of effusive lava flow generation and emplaced material during the TFE. Lava flow volume was derived by multiplying lava flow extent with the reconstructed lava thickness values for every pixel and every time step of the joint AVHRR/TanDEM-X time series. The generated observations indicated that deposition began first toward the south and west, forming the Vodopadnoye and Leningradskoye Flow Fields, largely within the first two days after the start of the eruption. The Vodopadnoye Lava Field, fed mostly from the lower Menyailov Vents, reached its maximum extent of ~8.5 km on 10 December 2012 (Gordeev et al., 2013). The Leningradskoye Lava Field reached its maximum length shortly thereafter, on 13 December 2012, but continued to widen and thicken until reaching its maximum area and volume in April 2013 (Belousov et al., 2015).

The joint AVHRR/TanDEM-X data show that deposition to the east of the eruption fissure commenced on or about 28 December 2012 and began forming the Toludskoye Lava Field. Flow thickening was episodic with extended periods of inactivity until the lava field reached its final thickness in late August, 2013, near the end of the TFE. While the buildup of the Toludskoye Lava Field led to a noticeable uptick in the total effused volume (Figure 3.10) starting around mid-January 2013, the contribution of this lava field to the total effused volume was found to be ~13%. The joint AVHRR/TanDEM-X data indicated that significant lava effusion ceased on or about 26 August 2013, which is in good correspondence with other published values of 27 August 2013, from Kubanek et al. (2017); and 23 August 2013, from Belousov et al. (2015). Detailed analyses of flow emplacement histories for five sample locations among the three lava flow fields are shown in Figures 3.14 - 3.18.

A comparison of hotspot locations to the reconstructed flow thickness time series suggests that levee formation may have occurred early in the eruption, channeling most lava flow near the center of the emplaced flow fields and encouraging rapid thickening along the flow centerlines. Evidence of this behavior can be found in Figure 3.8, which shows a comparison of hot spot locations relative to areas with significant flow thickness, as well as in Figure 3.5, which shows the flow thickness time series as extracted from TanDEM-X and indicates rapid flow thickening near flow centerlines.

Time averaged discharge rates derived from the joint AVHRR/TanDEM-X time series show good correspondence with other published results (e.g., Dvigalo et al., 2014; Belousov et al., 2015; Kubanek et al., 2017) while providing finer scale temporal detail than previously available. A five-day average of the joint time series (Figure 3.11) indicates that a significant amount of the total deposition was effused during the first ten days of the eruption, resulting in a time averaged discharge rate of ~300 $m^3 s^{-1}$ over these ten days. Effusive volume deposition dropped significantly thereafter, maintaining ~ 100 $m^3 s^{-1}$ for another ten days before leveling out at 0 - 30 $m^3 s^{-1}$ for most of the remaining event. A measurable uptick of deposition was observed near the end of the eruptive period, adding a final 0.05 km^3 of lava volume in August 2013, before activity ceased late in the month. Figure 3.11 shows that both the peak discharge rates as well as the general temporal decay of effusion activity, as derived from the joint AVHRR/TanDEM-X time series, mimics discharge rate information derived from airborne stereo photogrammetry by Dvigalo et al. (2014), and from spaceborne single-pass InSAR by Kubanek et al. (2017).

Implications

The results of this research demonstrate a series of methods that combine observations and measurements from different remote sensing instruments to achieve more complete and accurate understanding and evidence of the volcanic activity, than is available from a single instrument on its own. Chapter 1 demonstrated how optical data from an orbital platform could provide high resolution DEMs for volume estimates and also substantially improve the accuracy of surface deformation estimates as derived from d-InSAR. This chapter described, for the first time, a unique method of employing several multi-temporal InSAR coherence maps to identify the decorrelated boundaries and extent of those deposits with high precision, while minimizing noise and false positives.

Chapter 2 described a new method of estimating surface deformation of pyroclastic flow deposits (PFDs), including, for the first time, the subsidence contribution to surface deformation made by previous, underlying PFDs. This study employed 16-years of InSAR data collected from four separate SAR platforms, and resulted in a reconstructed subsidence history from two generations of superimposed flows, the latest of which was created before the existence of spaceborne SAR observation. The generated data provided evidence that PFDs subsidence scales with PFD thickness and led to the generation of a geophysical model that establishes InSAR as a tool for measuring PFD thicknesses, volumes, and thermal properties. The multi-sensor InSAR observations supported a hypothesis that the initial settling period of Augustine PFDs was usually concluded within a year of emplacement, and documented a decrease of deformation rates over time as cooling rates of the flows subsided. Finally, the only known thickness map of PFDs emplaced by Augustine Volcano's 1986 eruption was created. These results reinforce a better understanding of the behavior and geometry of PFDs when using InSAR, and to the need to incorporate data from multiple archived datasets on other platforms. The developed techniques can be transferred to other volcanic sites as well as a broader analysis of PFD volumes and subsidence behavior.

In the third and final chapter, DEMs derived from InSAR data were combined, for the first time, with thermal data from AVHRR satellites to produce a more detailed thickness and effusion profile of large effusive eruptions such as the TFE. InSAR data for this study was acquired from the TanDEM-X satellite-radar mission operated by the German Aerospace Center (DLR). This mission generates observations to derive very high spatial resolution flow thickness and accurate flow volume observations, but at coarse temporal sampling, ranging between 11 and 55 days. The AVHRR data, on the other hand, provided high temporal but coarse spatial resolution observations of thermal activity. Data from the AVHRR sensor also showed limitations due to sensor saturation, especially during the early phases of the eruptive period.

This chapter provided an avenue to combine these complementary sensor types to reach an unbiased and fine temporal resolution effusion time series for the Tolbachik event. Effusion rate and effusion volume time series were validated against and compared to other published information for this event including field reports and measurements from airborne stereo photogrammetry. The technology and joint timer series processing developed here can be used as a template for the combination of other spaceborne datasets of relevance such as thermal data from Himawari 8 (Bessho et al., 2016); the Geostationary Operational Environmental Satellite – R Series (GOES-R), (Schmit et al., 2005); or the Spinning Enhanced Visible and Infrared Imager (SEVIRI) on board the Meteosat Second Generation (MSG) satellites (Trigo et al., 2008), or DEM data from other spaceborne stereo-optical (e.g., DigitalGlobe constellation) and InSAR (e.g., TanDEM-L) sensors. As data availability and processing technologies for DEM generation from spaceborne data matures, the developed techniques may have important implications for operational monitoring applications as they may allow near real-time measurements of effusion rates and effusion volumes as an ongoing eruption progresses.

Future work

In the last few years, the topic of multi-sensor data fusion has gained significant attention in the volcanic remote sensing community. Beyond the knowledge that observations from multiple sensing modalities are beneficial to advance our understanding of volcanic processes, this development is fueled by the increasing availability of high-resolution and regularly available observations from remote sensing platforms. Examples of this trend can be found in recent work by Reath et al. (2019), Pritchard et al. (2018), and Papageorgiou et al. (2019).

With the multi-sensor frameworks developed in this dissertation now in place, future efforts should focus on increasing the diversity of sensor types in a joint analysis. For the topic of volcanic deposition, a broader combination of optical, thermal, derived aerosol, and multi-frequency SAR data should be sought. Reath et al. (2019) provides a summary of relevant sensor systems for a joint monitoring of degassing, thermal, and deformation signatures at active volcanoes. Reath et al. (2019) use observations from these various sensors to perform qualitative analyses of volcanic eruptions but stop short of generating quantitate evaluations on the eruption behavior from the data. An integration of the multi-sensor data in Reath et al. (2019) with the processing technologies developed in this dissertation would provide a major step forward to current state-of-the-art, as they would add extensive capability to derive quantitative effusion information from the ever growing suite of multi-sensor information.

Throughout the three chapters, the work conducted in this dissertation highlighted the value and extensive benefits of multi-temporal DEM observations for the study of volcanic eruptions. Repeat-pass DEM data are used to improve the accuracy of surface deformation estimates from InSAR (Chapters 1 and 2), provide observations on the thickness and volumes of volcanic deposits (Chapters 1 and 3), enable measurements of volcanic domes (Chapter 1), and determine unbiased effusion rates (Chapter 3). With the value of DEM's now understood, a broader integration of this data type into volcanic monitoring systems is suggested.

Chapter 2 of this thesis revealed that InSAR can provide important observations on the poroelastic and thermoelastic contraction properties of volcanic deposits. Based on dense time series of data at Augustine Volcano, the contribution of thermoelastic and poroelastic contraction was separated and their relative importance as a function of time. It was surprising to find that the thermoelastic contraction properties of lahar flows at Augustine Volcano were similar to the thermoelastic contraction behavior of basaltic and andesitic lava as calculated by Ebmeier et al.,

(2012) from a limited set of global measurements. Based on these findings, a study on the impact of compositional properties on the contraction behavior of volcanic deposits is recommended.

While Chapter 3 provided the first application of jointly processing thermal and DEM time series data to analyze the eruptive behavior of large effusive eruptions, further research should study the following potential improvements to the technique: (1) the current technology does not take advantage of the quantitative data available in the different bands of a thermal sensor. Integration of sensor bands that are less prone to saturation into the technique would strengthen the accuracy of the derived time series. Such integration could be achieved by modifying two-band methods for effusion rate estimation to include bands with lower saturation likelihood or by including these datasets as weights in the time-series interpolation (as proposed in Eq. 3.10); (2) by resampling all data into the geospatial grid of the thermal sensor, the current approach does not take full advantage of the high-spatial resolution capabilities of the DEM-derived flow thickness observations. Methods could be devised that use high-resolution flow thickness measurements to interpolate the lower resolution thermal imagery, resulting in effusion observations that are have fine resolutions in both time and space.

Finally, an integration of the developed technology into operational monitoring systems should be considered. To make meaningful contributions in a response situation, the robustness and throughput capabilities of current remote sensing data processing technology needs to be improved. This is particularly true for SAR-based DEM and deformation measurement techniques. Both require more research to increase their level of automation and improve automatic error handling techniques to warrant operational use. With the continuous increase of available remote sensing sensors and considering the current explosion of remote sensing data volumes, the development of mechanisms to efficiently process large data volumes should also be considered. Cloud-based solutions have shown some success in facilitating near real-time remote sensing data processing in operational hazard monitoring systems (Meyer et al., 2018), , by providing high-throughput processing capabilities and by allowing elastic scaling of compute resources. However, more research is required to develop technology that is easy to use, fully scalable, and affordable.

It is my hope that the research presented here will provide the community with clues about how to take effective advantage of this growing pool of multi-sensor observations. I furthermore hope that the analysis concepts developed in this thesis will find broad applications in the study of volcanic activity in Alaska and beyond.

References to Conclusion

Belousov, A., Belousova, M., Edwards, B., Volynets, A., and Melnikov, D., 2015, Overview of the precursors and dynamics of the 2012–13 basaltic fissure eruption of Tolbachik Volcano, Kamchatka, Russia: Journal of Volcanology and Geothermal Research, v. 307, p. 22-37, doi: 10.1016/j.jvolgeores.2015.06.013.

Bessho, K., Date, K., Hayashi, M., Ikeda, A., Imai, T., Inoue, H., Kumagai, Y., Miyakawa, T., Murata, H., and Ohno, T., 2016, Journal of the Meteorological Society of Japan, v. 94, p. 151-183, doi: 10.2151/jmsj.2016-00.

Bull, K.F., 2009, Redoubt Volcano: 2009 Eruption Overview: AGU Fall Meeting, Abstract V51F-01, v. 1, p. 01.

Bull, K.F., and Buurman, H., 2013, An overview of the 2009 eruption of Redoubt Volcano, Alaska: Journal of Volcanology and Geothermal Research, v. 259, p. 2-15, doi: 10.1016/j.jvolgeores.2012.06.024.

Diefenbach, A., Bull, K.F., Wessels, R.L., and McGimsey, R., 2013, Photogrammetric monitoring of lava dome growth during the 2009 eruption of Redoubt Volcano: Journal of Volcanology and Geothermal Research, v. 259, p. 308-316, doi: 10.1016/j.jvolgeores.2011.12.009.

Dvigalo, V.N., Svirid, I.Y., and Shevchenko, A.V., 2014, The first quantitative estimates of parameters for the Tolbachik Fissure Eruption of 2012–2013 from aerophotogrammetric observations: Journal of Volcanology and Seismology, v. 8, p. 261-268, doi: 10.1134/s0742046314050029.

Ebmeier, S.K., Biggs, J., Mather, T.l., Elliott, J.R., Wadge, G., and Amelung, F., 2012, Measuring large topographic change with InSAR; lava thicknesses, extrusion rate, and subsidence rate at Santiaguito Volcano, Guatemala: Earth and Planetary Science Letters, p. 216-225, doi: 10.1016/j.epsl.2012.04.027.

Gordeev, E., Muravyov, Y.D., Samoylenko, S., Volynets, A., Melnikov, D., Dvigalo, V., and Melekestsev, I., 2013, First results from the 2012-2013 Tolbachik fissure eruption: Bulletin of the Volcanological Society of Japan, v. 58, p. 1-8.

Kubanek, J., Westerhaus, M., and Heck, B., 2017, TanDEM-X time series analysis reveals lava flow volume and effusion rates of the 2012–2013 Tolbachik, Kamchatka fissure eruption: Journal of Geophysical Research: Solid Earth, v. 122, p. 1-21, doi: 10.1002/2017JB014309.

Meyer, F.J., Ajadi, O.A., Schultz, L., Bell, J., Arnoult, K.M., Gens, R., and Nicoll, J.B., 2018, An Automatic Flood Monitoring Service from Sentinel-1 SAR: Products, Delivery Pipelines, and Performance Assessment, *in* Proceedings, IGARSS 2018 - 2018 IEEE International Geoscience and Remote Sensing Symposium, 22-27 July 2018, pp. 6576-6579, doi: 10.1109/igarss.2018.8517531.

Papageorgiou, E., Foumelis, M., Trasatti, E., Ventura, G., Raucoules, D., and Mouratidis, A., 2019, Multi-Sensor SAR Geodetic Imaging and Modelling of Santorini Volcano Post-Unrest Response: Remote Sensing, v. 11, p. 259, doi: 10.3390/rs11030259.

Pritchard, M., Biggs, J., Wauthier, C., Sansosti, E., Arnold, D., Delgado, F., Ebmeier, S., Henderson, S., Stephens, K., and Cooper, C., 2018, Towards coordinated regional multi-satellite InSAR volcano observations: results from the Latin America pilot project: Journal of Applied Volcanology, v. 7, p. 5, doi: 10.1186/s13617-018-0074-0.

Reath, K., Pritchard, M., Poland, M., Delgado, F., Carn, S., Coppola, D., Andrews, B., Ebmeier, S., Rumpf, E., and Henderson, S., 2019, Thermal, Deformation, and Degassing Remote Sensing Time Series (CE 2000–2017) at the 47 most Active Volcanoes in Latin America: Implications for Volcanic Systems: Journal of Geophysical Research: Solid Earth, doi: 10.1029/2018JB016199.

Schmit, T.J., Gunshor, M.M., Menzel, W.P., Gurka, J.J., Li, J., and Bachmeier, A.S., 2005, Introducing the next-generation Advanced Baseline Imager on GOES-R: Bulletin of the American Meteorological Society, v. 86, p. 1079-1096, doi: 10.1175/BAMS-86-8-1079.

Siebert, L., Cottrell, E., Venzke, E., and Andrews, B., 2015, Chapter 12 - Earth's Volcanoes and Their Eruptions: An Overview, *in* Sigurdsson, H., ed., The Encyclopedia of Volcanoes (Second Edition): Amsterdam, Academic Press, pp. 239-255, doi: 10.1016/B978-0-12-385938-9.00012-2.

Trigo, I.F., Peres, L.F., DaCamara, C.C., and Freitas, S.C., 2008, Thermal land surface emissivity retrieved from SEVIRI/Meteosat: IEEE Transactions on Geoscience and Remote Sensing, v. 46, p. 307-315, doi: 10.1109/TGRS.2007.905197.

Waythomas, C.F., Pierson, T.C., Major, J.J., and Scott, W.E., 2013, Voluminous ice-rich and water-rich lahars generated during the 2009 eruption of Redoubt Volcano, Alaska: Journal of Volcanology and Geothermal Research, v. 259, p. 389-413, doi: 10.1016/j.jvolgeores.2012.05.012.